Heavy-Ion Induced Void and Loop Formation in High Purity Vanadium

William John Weber

December 1977

UWFDM-182

Ph.D. thesis.

FUSION TECHNOLOGY INSTITUTE

UNIVERSITY OF WISCONSIN

MADISON WISCONSIN

Heavy-Ion Induced Void and Loop Formation in High Purity Vanadium

William John Weber

Fusion Technology Institute
University of Wisconsin
1500 Engineering Drive
Madison, WI 53706

http://fti.neep.wisc.edu

December 1977

UWFDM-182

Ph.D. thesis.

HEAVY-ION INDUCED VOID AND LOOP FORMATION IN HIGH PURITY VANADIUM

BY

WILLIAM JOHN WEBER

A thesis submitted in partial fulfillment of the
requirements for the degree of

DOCTOR OF PHILOSOPHY
(Nuclear Engineering)
at the
UNIVERSITY OF WISCONSIN-MADISON

1977

ABSTRACT

HEAVY-ION INDUCED VOID AND LOOP FORMATION IN HIGH PURITY VANADIUM

William John Weber

Under the supervision of Professor Gerald L. Kulcinski

Vanadium and its alloys are among the refractory metals considered for use as first wall material in a Controlled Thermonuclear Reactor (CTR). At CTR operating temperatures radiation induced microstructural changes in the form of voids, dislocation loops, and enhanced precipitation can produce dimensional and mechanical property changes which may greatly affect the lifetime of the first wall and the success of the CTR as a potential energy source. Therefore, a vigorous effort to understand the relationship between microstructural changes and the irradiation and material parameters is required.

In this investigation annealed samples of high purity vanadium are irradiated with 18 MeV, and in some cases 14 MeV, copper ions in order to study the characteristics of void and loop formation in high purity vanadium. The samples were irradiated at temperatures from 150 to 850°C. The irradiation-induced damage was analyzed at a depth of 1 micron by transmission electron microscopy. The damage level at this depth was on the order of 1 dpa and the damage rate was approximately 10^{-4} dpa/s.

The damage structure consisted of voids, dislocation loops, dislocation networks, and some irradiation-enhanced precipitation. Voids were observed to form from 200 to 700°C in the high purity vanadium. Black spot damage was found at 150°C and no voids were found in samples irradiated at 750, 800, and 850°C. The void swelling curve exhibited a double peak with the maximum occurring at 650°C and a broad low temperature peak occurring between 200 and 500°C. Radiation-induced precipitation within a narrow temperature range (500-600°C) resulted in a sharp decrease in void density and the presence of large vacancy loops in the absence of the voids. These precipitates were rod-shaped with their axis along one of the $\langle 100 \rangle$ directions and the loops were found to lie on $\{110\}$ planes and have Burgers vectors of $a/2\langle 111 \rangle$. Hydrogen, introduced into several vanadium samples by electropolishing, was found to enhance void nucleation and remain in the samples unless temperatures exceeded 750°C. In several samples which became contaminated with nickel, a metastable, partially coherent phase in the V-Ni system formed during irradiation. These nickel-bearing precipitates enhanced void swelling.

Approved ______________________________

ACKNOWLEDGEMENTS

The author would like to express his gratitude and sincere appreciation for the continual guidance, encouragement, and support given by his advisor, Professor G.L. Kulcinski, during the course of this study. The author would also like to thank Professor P. Wilkes for his advice and constructive criticism and Professor J.M. Donhowe for his guidance and encouragement during the early years of this study.

Special thanks are due Dr. H.V. Smith, Jr., Dr. R. I. Saunderson, R.G. Lott, J.B. Whitley, and S.K. McLaurin for assistance in the experimental work and for many helpful discussions and stimulating conversations.

The author is grateful to the University of Wisconsin Nuclear Physics Group for use of the tandem accelerator and its facilities.

The financial support of the United States Energy Research and Development Administration - Division of Physical Research, the University of Wisconsin Graduate School, and the National Science Foundation is greatly appreciated.

Finally, the author wishes to thank his wife, Jan, for her patience and moral support during the course of this research.

TABLE OF CONTENTS

Page

ABSTRACT. i

ACKNOWLEDGEMENTS. iii

Chapter

I. INTRODUCTION 1

Historical Review. 2
Vanadium 6

II. THEORETICAL ASPECTS OF RADIATION DAMAGE CALCULATIONS 9

The Unit of Radiation Damage 9
Neutron Irradiations 10
Charged-Particle Irradiations. 15
Electron Irradiations. 24

III. THEORY OF VOID SWELLING. 27

General Conditions For Void Swelling 27
Loop Formation 31
Void Nucleation. 34
Void Growth. 41

IV. PREVIOUS STUDIES OF IRRADIATION DAMAGE IN VANADIUM . 45

Neutron Irradiated Vanadium. 45
Heavy-Ion Irradiated Vanadium. 51
Electron Irradiated Vanadium 59

V. EXPERIMENTAL EQUIPMENT AND PROCEDURE 62

Heavy-Ion Irradiation Facility 62
High Vacuum Annealing System 76
Material Characterization. 80
Sample Preparation 83
Transmission Electron Microscopy (TEM) 89

TABLE OF CONTENTS-Continued

Page

VI. EXPERIMENTAL RESULTS 101

Introduction 101
Group I. 104
  Qualitative Results 104
  Nature of the Group I Precipitates. 110
  Quantitative Results. 122
Group II 133
  Qualitative Results 133
  Geometrical Analysis. 153
  Quantitative Results. 161

VII. DISCUSSION 173

Introduction 173
Precipitate Structures 173
  Group I 173
  Group II. 176
Void Microstructures 179
  Group I 180
  Group II. 181
Dislocation Substructures. 187
  Group I 187
  Group II. 187

VIII. CONCLUSIONS. 190

. . . .

APPENDIX A. 193

REFERENCES. 197

LIST OF FIGURES

Page

1. The Total Displacement Cross Section In Neutron Irradiated Vanadium. 14

2. The LSS Function $f(t^{\frac{1}{2}})$ Numerically Calculated From A Thomas-Fermi Potential. 18

3. Nuclear And Electronic Stopping Powers In Reduced Units From The LSS Model 20

4. Depth Distribution Of Damage And Copper Atoms In Vanadium Irradiated With 14 MeV Cu Ions. 23

5. The Total Displacement Cross Section In Electron Irradiated Vanadium. 26

6. The University of Wisconsin Heavy-Ion Irradiation Facility 63

7. Schematic Of The Target Chamber - U.W. Heavy-Ion Irradiation Facility 65

8. Partial Pressure Analysis of the Residual Gas In The Target Chamber At 1050°C and at 700°C. 67

9. Schematic Of The Sample Chamber Detailing The Relative Positions Of The Ion Beam Diagnostic Devices, Heater, Heat Shield, And Sample Holder. . 69

10. Ion Beam Composition 70

11. Schematic Of The Radiation Heater Assembly In The Sample Chamber 72

12. Schematic Of The Sample Holder For Irradiating Foil Strips. 73

13. Sample Holder For Irradiating 3 mm Discs 74

14. Schematic Of The Sample Holder For Irradiating 3 mm Discs 75

15. Sample Holder For The High Vacuum Annealing Furnace. 78

LIST OF FIGURES-Continued

Page

16. High Vacuum Annealing Furnace. 79

17. Residual Gas Scan During An Anneal In The High Vacuum Annealing Furnace 81

18. A Comparison Of The Residual Gases During Annealing In The Target Chamber And During Annealing In The High Vacuum Furnace. 82

19. The Grain Structure In Vanadium After A One Hour Anneal at 1050°C 86

20. Depth Distribution Of Damage And Copper Atoms In Vanadium Irradiated With 18 MeV Cu Ions. 88

21. Step Height Measurement Of The Amount Of Surface Removed From An Irradiated Sample. 90

22. Illustration Of The FS/RH Convention For Defining b For A Vacancy Loop And An Interstitial Loop. . . 97

23. Stereographic Projection Showing Those Crystal Orientations Where All The Possible n's Are In "Safe Orientations" For A Non-Edge Loop With Burgers Vector Of a/2 [111] 99

24. Void And Precipitate Microstructure In The Vanadium Samples Of Group I Irradiated With 18 MeV Cu Ions To 1 dpa. 107

25. Voids And Precipitates In The Vanadium Samples Of Group I Which Were Electropolished After Annealing And Then Irradiated With 18 MeV Cu Ions To 1 dpa . 108

26. Void Wall In Vanadium Irradiated At 650°C With 14 MeV Cu Ions To 5 dpa 111

27. Void And Precipitate Denuding Along Grain Boundaries In Vanadium Irradiated at 650°C With 14 MeV Cu Ions To 5 dpa. 112

LIST OF FIGURES-Continued

Page

28. Dislocation Structure In The Vanadium Samples Of Group I Irradiated, As Annealed, With 18 MeV Cu Ions To 1 dpa 113

29. Dislocation Structure In The Vanadium Samples Of Group I Irradiated, After Electropolishing, With 18 MeV Cu Ions To 1 dpa 114

30. Voids And Precipitates In Sample 5 Of Table 7 Irradiated At 700°C To 1 dpa 118

31. Precipitates And Their Diffraction Pattern In Sample 5 Of Table 7. 120

32. The General Shape And Relative Orientation Of The Large Precipitates In The Vanadium Samples Of Group I. 121

33. Energy Dispersive X-Ray Analysis Of A Precipitate And An Adjacent Region Of Matrix In An Irradiated Sample of Group I. 123

34. Average Void Size As A Function Of Temperature For The Vanadium Samples Of Group I Irradiated to 1 dpa. 127

35. Void Density As A Function Of Temperature For The Vanadium Samples Of Group I Irradiated To 1 dpa. . 128

36. Void Swelling As A Function Of Temperature For The Vanadium Samples Of Group I Irradiated To 1 dpa. . 129

37. Void Size Distribution In The Vanadium Samples Of Group I Irradiated At 650 and 700°C To 1 dpa . . . 130

38. Voids In The Precipitate-Free Matrix Of A Sample In Group II Irradiated At 700°C To 2 dpa. 134

39. Voids In The Vanadium Sample Of Group II Irradiated, As Annealed, At 600°C With 18 MeV Cu Ions To 2 dpa. 136

LIST OF FIGURES-Continued

Page

40. Voids In The Vanadium Sample Of Group II Irradiated, After Electropolishing, At 600°C With 18 MeV Cu Ions To 2 dpa 137

41. Voids In The Vanadium Sample Of Group II Irradiated, After Electropolishing, At 650°C With 18 MeV Cu Ions To 2 dpa 138

42. Voids In The Vanadium Samples Of Group II Irradiated At 700°C With 18 MeV Cu Ions To 2 dpa. 139

43. Dislocation Structure In The Vanadium Sample Of Group II Irradiated At 600°C With 18 MeV Cu Ions To 2 dpa. 141

44. Dislocation Structure In The Vanadium Samples Of Group II Irradiated At (a) 650°C and (b) 700°C With 18 MeV Cu To 2 dpa. 142

45. Black Spot Damage And Voids In The Vanadium Samples Of Group II Irradiated With 14 MeV Cu Ions To 1 dpa. 144

46. Voids In The Vanadium Samples Of Group II Irradiated With 14 MeV Cu Ions To 1 dpa 145

47. Microstructure In The Vanadium Sample Of Group II Irradiated At 550°C With 14 MeV Cu Ions To 1 dpa . 146

48. The Effect Of Grain Boundaries On Void Formation In A Sample Of Group II Irradiated At 500°C With 14 MeV Cu Ions To 1 dpa. 148

49. Dislocation Structure In The Vanadium Sample Of Group II Irradiated At 500°C With 14 MeV Cu Ions To 1 dpa. 149

50. Dislocation Structure In The Vanadium Samples Of Group II Irradiated At 200 and 350°C With 14 MeV Cu Ions To 1 dpa 150

LIST OF FIGURES-Continued

Page

51. Voids In The Vanadium Samples Of Group II Containing Hydrogen And Irradiated With 18 MeV Cu Ions To 2 dpa 152

52. Void Shapes At Different Crystallographic Orientations In The Vanadium Sample Of Group II Irradiated At 700°C To 2 dpa 154

53. Void Shapes In The Vanadium Sample Of Group II Containing Hydrogen And Irradiated at 650°C To 2 dpa 156

54. Dislocation Loop Analysis In Vanadium Irradiated At 600°C To 2 dpa. 157

55. Precipitates Along <100> Directions In The Vanadium Sample Of Group II Irradiated At 550°C To 1 dpa 160

56. Average Void Size As A Function Of Temperature For The Vanadium Samples Of Group II 164

57. Void Density As A Function Of Temperature For The Vanadium Samples Of Group II 165

58. Void Swelling As A Function Of Temperature In The Vanadium Samples Of Group II Irradiated With 18 MeV Cu Ions To 2 dpa. 167

59. Void Swelling As A Function Of Temperature In The Vanadium Samples Of Group II Irradiated With 14 MeV Cu Ions To 1 dpa 168

60. A Comparison Of The Void Swelling Resulting From This Study With The Results Obtained At ANL. . . . 183

61. Void Swelling And Relative Amount Of Precipitation As A Function Of Temperature In The Vanadium Samples Of Group II. 184

LIST OF TABLES

Page

1. Void Parameters In Neutron Irradiated Vanadium 46

2. Void Parameters In Heavy-Ion Irradiated Vanadium 53

3. Orientation Dependence Of E_d^{th} In Vanadium. 60

4. Chemical Analysis Of The Vanadium Used In This Study 84

5. Samples And Irradiation Conditions For Group I. 102

6. Samples And Irradiation Conditions For Group II 103

7. Description Of Samples Sent To Grumman Aerospace Corporation For Depth Analysis Of C, O, and N Concentrations 116

8. Impurity Concentration As A Function Of Depth In The Vanadium Samples Of Table 7. 117

9. Sources Of Error In The Quantitative Data. 124

10. Summary Of Void And Precipitate Data For The Vanadium Samples Of Group I. 126

11. Summary Of The Dislocation Data For The Samples Of Group I 132

12. Summary Of The Contrast Behavior Of Loops Labeled In Figure 54 158

13. Summary Of Void Data For The Vanadium Samples Of Group II Irradiated With 18 MeV Copper Ions To 2 dpa. 162

14. Summary Of Void Data For The Vanadium Samples Of Group II Irradiated With 14 MeV Copper Ions. . . . 163

LIST OF TABLES-Continued

Page

15. Summary Of The Dislocation Data For The Vanadium Samples Of Group II Irradiated With 18 MeV Copper Ions To 2 dpa 169

16. Summary Of The Dislocation Data For The Vanadium Samples Of Group II Irradiated With 14 MeV Copper Ions To 1 dpa 170

17. Summary Of The Data For The Rod-Shaped Precipitates In The Vanadium Samples Of Group II. 172

CHAPTER I

INTRODUCTION

Fast neutron irradiation of solids results in the displacement of atoms from their normal lattice sites forming vacancies and interstitials. With the exception of helium production, these point defects are responsible for the major radiation damage effects that occur in a fast neutron environment. Two effects of interest are the formation of dislocation loops (planar clusters of either vacancies or interstitials) and the formation of voids (three dimensional aggregates of vacancies) in pure metals and alloys subject to high temperature, high energy neutron bombardment.

Dislocation loop formation affects the mechanical properties of the material and is an important parameter controlling the formation of voids through the increased density of sinks for point defects. In addition, preferred nucleation and growth of loops to relieve stress is believed to be responsible for the irradiation-enhanced creep observed in materials.

Several requirements for void formation limit its occurence to a temperature range of approximately 0.2 to 0.5 T_m, where T_m is the absolute melting temperature. Within this temperature range, void formation in fast neutron irradiated materials results in a volumetric swelling due to the displaced interstitials; and, because of the temperature and flux dependence of swelling, differential swelling can occur.

The swelling associated with voids and the stresses produced by the swelling gradients have become one of the major problems in the development of commercial Liquid Metal Fast Breeder Reactors (LMFBR's). The problems associated with the formation of voids are not limited to the LMFBR program; designers of future Controlled Thermonuclear Reactors (CTR's) are also finding that void formation and the associated effects will be a serious problem to overcome. The effect of void formation on the success of these two potential energy sources has prompted an active international research effort to study voids and the factors that control their nucleation and growth. The objective of that effort is to provide theoretical models that can accurately predict the dimensional behavior of LMFBR and CTR components during the respective reactor's lifetime.

Historical Review

Radiation-induced voids were first observed in 1966 by Cawthorne and Fulton in transmission electron microscopy (TEM) specimens of stainless steel irradiated in the Dounreay Fast Reactor(1), and their results became generally known when published in 1967(2). Although Greenwoood, Foreman and Rimmer suggested in 1959 that such a phenomenon might occur(3), voids were not discovered until 1966 because very high fast neutron fluences ($\sim 10^{22}$ n/cm^2) were required to produce an observable density of voids in the temperature range of void formation. The discovery of void formation in stainless steel was soon followed by the observation of voids in pure nickel(4) exposed to a fast neutron dose two orders of magnitude lower than in the stainless steel observations of Cawthorne and Fulton; thus, it was apparent that void formation depended on various material parameters.

Because of the implications of void formation and resultant swelling on the design of LMFBR's and CTR's, theoretical and experimental investigations were directed at the study of void formation and the parameters affecting void nucleation and growth. These early studies resulted in two major conferences during 1971 on the subject of voids, and the proceedings of these conferences(5, 6) give a good summary of the work in the area of void formation up to mid-1971. A more recent conference at Harwell on the subject of voids in late 1974(7) provides some of the most recent information regarding this phenomenon. Additional information on voids and loops may be found in the proceedings of several other major conferences dealing with irradiation effects(8-12).

New data on fast neutron induced void formation has been slow in coming forth. The reason is that long irradiations (one to two years) are required to produce voids in existing facilities, such as EBR-II and DFR. These facilities cannot provide the high fast neutron fluences needed to simulate the type of damage expected during the lifetime of future LMFBR's and CTR's, unless long irradiations on the order of those lifetimes are used. Fortunately, it was recognized early that charged-particles could simulate the displacement effects of fast neutrons in a short period of time.

The advantages of using charged-particles to increase the damage rate by several orders of magnitude were first recognized in 1969 by Nelson and Mazey at Harwell(13). Using low energy heavy ions, they were able to produce, in a matter of hours, a damage state in stainless steel which normally required a year or more of fast neutron irradiation to produce. They later found that 20 MeV carbon ions would produce similiar results in a larger volume of the sample(14-17). Their work was confirmed in the U.S. when Keefer and coworkers(18) were able to obtain similar results by bombarding stainless steel with high energy protons and when Kulcinski et al.(19) observed voids in stainless steel bombarded with copper ions.

The major difference between neutron and charged-particle irradiation is the magnitude of the elastic scattering cross section. Since charged-particles interact with the lattice atoms in atomic collisions, the cross section is approximately 10^6 times higher than the neutron cross section(15). As a consequence, the mean free path between collisions is reduced from centimeters for neutrons to hundreds of angstroms for heavy-ions. This severely limits the penetrating power of a heavy-ion, resulting in the damage being isolated near the irradiated surface.

The charged-particle that best simulates fast neutron damage is the self-ion (bombarding particle of same species as target); this eliminates the objectional feature of introducing a high concentration of impurity atoms into the target during the irradiation. In stainless steel studies the commercial concentration of copper (about 0.2%) and nickel (8-20%) allows readily available Cu and Ni ions to be used as self-ions (19,20,21). However, studies of fast neutron damage in pure metals suffer from the lack of suitable heavy ion sources to produce the self-ions. Notable exceptions to this have been the self-ion studies on nickel(22, 23), aluminum(24,25), vanadium(26,27), and molybdenum(28).

With the aid of charged-particle irradiations, investigators are now able to produce, in convenient laboratory times, the type of damage expected to occur during the lifetime of a component in future LMFBR's or CTR's. In addition to the high damage rate, ion irradiation allows the experiments to be carried out under more controlled conditions. Temperature, charged-particles flux, and dose can all be independently varied. Transmutation effects are eliminated or can be closely controlled. For example, the experimenter can control the type and energy of bombarding particle, as well as the type and concentration of gaseous and solid impurities in the target material. However, because of the small depth of penetration of charged-particles, experiments to measure bulk property changes, such as creep or yield stress, cannot be performed. Only void size, shape, density, and associated dislocation and precipitate microstructure can be observed in an electron microscope.

It should also be mentioned that charged-particle simulation of fast neutron damage relies heavily on the theoretical assignment of a displacement production rate to the region under observation in the electron microscope.

Vanadium

Vanadium was originally chosen for this study because vanadium and vanadium-base alloys were considered as potential materials for use in both LMFBR's and CTR's. Since that time vanadium and its alloys have been dropped from consideration as LMFBR materials (a result of their high affinity for the oxygen in the liquid sodium coolant). However, vanadium and its alloys are still among the refractory metals considered for use as first wall material in CTR's. The first wall of a CTR will experience high 14 MeV neutron fluxes which produce atomic displacements that can cause changes in microstructure during the irradiation. At CTR operating temperatures, these microstructural changes in the form of voids, dislocation loops, and enchanced precipitation can produce dimensional and mechanical property changes which may greatly affect the lifetime of the first wall and the success of the CTR as a potential energy source.

Studies of void formation in neutron irradiated vanadium are severely limited by the long irradiation times required in presently available fast reactors and the difficulty in controlling the irradiation environment. Current data (discussed in Chapter IV) on void formation in neutron irradiated vanadium come from relatively low fluence studies ($< 5 \times 10^{22}$ n/cm^2) and are not sufficient to confidently predict first wall lifetimes. For this reason, charged-particle irradiations, with their high damage rates, are used to study void formation in potential reactor materials. Charged-particle irradiations also have an advantage over reactor irradiations in that the sample environment is more easily controlled; this is important because of the high solubility of interstitial impurities, such as oxygen, nitrogen, and carbon, in vanadium.

It is the purpose of this dissertation to study the fundamental parameters affecting void formation in heavy-ion irradiated, high purity vanadium. The parameters of interest are dose and temperature; however, during the course of this investigation it was found that sample preparation techniques, annealing environment, and irradiation environment also affected the results obtained. These effects and the results are discussed in detail in Chapters VI and VII. The irradiations were carried out with either 14 or 18 MeV copper ions using the University of Wisconsin Tandem Van de Graaff Accelerator (HVEC model EN), and the analysis was done by transmission electron microscopy (TEM) of the irradiated specimens. Unlike some of the previous investigations of heavy-ion irradiated vanadium (discussed in Chapter IV), this investigation did not study the effects of implanted helium on void formation. This study is meant to provide the groundwork on which to base future studies on the effects of gases and other impurities on void formation in vanadium. The vanadium in this study was irradiated to much lower damage levels, at much lower damage rates, and at lower temperatures than previous investigations using heavy-ions. The result of using the lower damage levels, damage rates, and temperatures is to allow a better correlation with the low dose, low damage rate neutron irradiations and to provide valuable data for use in theoretical models of void nucleation and/or as initial conditions in computer simulation of void growth in vanadium.

CHAPTER II

THEORETICAL ASPECTS OF RADIATION DAMAGE CALCULATIONS

The Unit of Radiation Damage

The correlation of the damage produced by fast neutrons and charged-particles requires a simple criterion by which one can compare the doses received during reactor irradiations and charged-particle irradiations. The criterion chosen is the theoretical number of atoms displaced at $0^{o}K$ during the irradiation, and the unit of radiation damage is the dpa (displacement per atoms).

The dpa is defined as the fraction of atoms displaced from their lattice positions during the irradiation exposure. Although the dpa is the accepted unit of damage in the scientific community, it has its drawbacks. First, the dpa unit does not tell how the lattice atoms were displaced, one by one or in a cascade. Secondly, the dpa unit infers nothing about the gas generation rates or the solid transmutation rates in a reactor. Some processes, such as void nucleation, are thought to be extremely sensitive to the gas concentration in the metal. Third, many processes are damage rate dependent, and the dpa unit is independent of damage rate.

The remainder of this chapter will describe how the dpa value is determined in neutron, heavy-ion, and electron irradiations.

Neutron Irradiations

A term often found in the literature on radiation damage is primary knock-on atom or, as it is often referred to, PKA. The PKA is the initial lattice atom displaced from its lattice site through some interaction with a neutron. Of primary interest are the PKA's energetic enough to cause cascades and a large number of subsequent displacements. The method used to calculate the number of displaced atoms is described below for the case of a PKA produced as a result of an elastic collision between a fast neutron and a lattice atom. Other nuclear reactions (particularly in a CTR environment) often account for many more displacements; these reactions will also be considered.

The energy transferred, T, from an incident particle of energy E to a lattice atom in an elastic collision is(29)

$$T = \frac{4mM}{(m + M)^2} E \sin^2 (\psi/2) \qquad (1)$$

where m is the mass of the incident particle, M is the mass of the struck atom, and ψ is the center of mass scattering angle. In the case of neutrons,

$$T = \frac{4A}{(1 + A)^2} E \sin^2 (\psi/2) \qquad (2)$$

where A is the mass number of the struck atom.

The maximum energy energy transferred to the struck atom is

$$T\,(\max) = \Lambda E \qquad (3)$$

where

$$\Lambda = \frac{4mM}{(m + M)^2} \tag{4}$$

or, in the case of incident neutrons,

$$\Lambda = \frac{4A}{(1 + A)^2} \tag{5}$$

If E_d is the average kinetic energy required by an atom to be displaced from its normal lattice position, then the minimum value of E able to transfer this energy is(30)

$$E\ (\min) = E_d/\Lambda\ . \tag{6}$$

The probability that an incident neutron of energy E will transfer to a lattice atom on amount of kinetic energy between T and T + dT is given by the differential cross section, $d\sigma\ (E,T)$. Therefore, the production rate (per unit neutron energy) of PKA's with kinetic energy between T and T + dT by neutrons of energy E is given by

$$F_{PKA}(E,T)\ dT = N\,\phi\,(E)\ \frac{d\sigma\ (E,T)}{dT}\ dT \tag{7}$$

where N is the density of the target atoms, and $\phi(E)$ is the energy dependent neutron flux.

By defining a function $\nu(T)$ as the number of displacements produced by a PKA of energy T, the expression for the displacement rate of lattice atoms in a flux $\phi(E)$ is given by

$$F_D(E) = N\,\phi(E) \int_{E_d}^{\Lambda E} \nu(T)\ \frac{d\sigma\ (E,T)}{dT}\ dT\ . \tag{8}$$

(Expressions for $\nu(T)$ are discussed in Appendix A.)

The dpa rate from elastic collisions is then given by the expression

$$\text{dpa rate} = \int_{o}^{E_{max}} dE\ \phi(E) \int_{E_d}^{\Lambda E} \nu(T)\ \frac{d\sigma(E,T)}{dT}\ dT. \tag{9}$$

and the total dpa for a given irradiation is found by a simple integration over time.

The above expression for dpa rate was derived for the case of elastic collisions. A similar expression holds when all reactions resulting in displacements are taken into account and is given by

$$\text{dpa rate} = \Sigma_i \int_{o}^{\infty} \phi(E)\ dE \int_{E_d}^{T_{max}} \nu(T)\ \frac{d\sigma_i(E,T)}{dT}\ dT \tag{10}$$

where $d\sigma_i(E,T)$ is the differential cross section for transferring an amount of kinetic energy between T and T + dT to a lattice atom after a reaction of the ith type with a neutron of energy E. Equation 10 can be simplified by defining the total displacement cross section $\sigma_d(E)$:

$$\sigma_d(E) = \Sigma_i \int_{E_d}^{T_{max}} \nu(T)\ \frac{d\sigma_i(E,T)}{dT}\ dT. \tag{11}$$

The dpa rate is then given by

$$\text{dpa rate} = \int_0^\infty \phi(E) \quad \sigma_d(E)\ dE. \tag{12}$$

The types of reactions one usually considers in these calculations are (n,n), (n,n'), (n,2n), (n,γ), (n,α), and (n,p) reactions. The total displacement cross section, σ_d, for vanadium, as reported by Çabriel, Amburgay, and Greene$^{(31)}$, is plotted as a function of energy in Figure 1. The total displacement cross section in Figure 1 is dominated by the (n,γ) cross section at low energies (10^{-1} to 10^2 eV) and by the elastic cross section, (n,n) at intermediate energies (10^2 to 10^7 eV). A series of resonances in the elastic cross section is responsible for the peak at 10^4 eV. At 3.26×10^5 eV (threshold energy) the inelastic cross section, (n, n'), begins to contribute to the total displacement cross section. The dominant reactions at the highest energies ($>10^7$ eV) are the (n,p), (n,α), and (n,2n) reactions with respective threshold energies of 3×10^6 eV, 7×10^6 eV, and 1.128×10^7 eV.

Another aspect of neutron irradiations to be considered in the formation of voids is the gas generation rate. The gases of interest are helium and hydrogen, and they are produced as a result of (n,α), (n, n'α), (n,p) and (n,n'p) reactions. For the case of helium, the gas generation rate is approximately given by:

$$\begin{array}{c}\text{Helium}\\ \text{Production}\\ \text{Rate}\end{array} = N \int_0^{E_{\max}} \phi(E) \left[\sigma_{n,\alpha}(E) + \sigma_{n,n'\alpha}(E)\right] dE \tag{13}$$

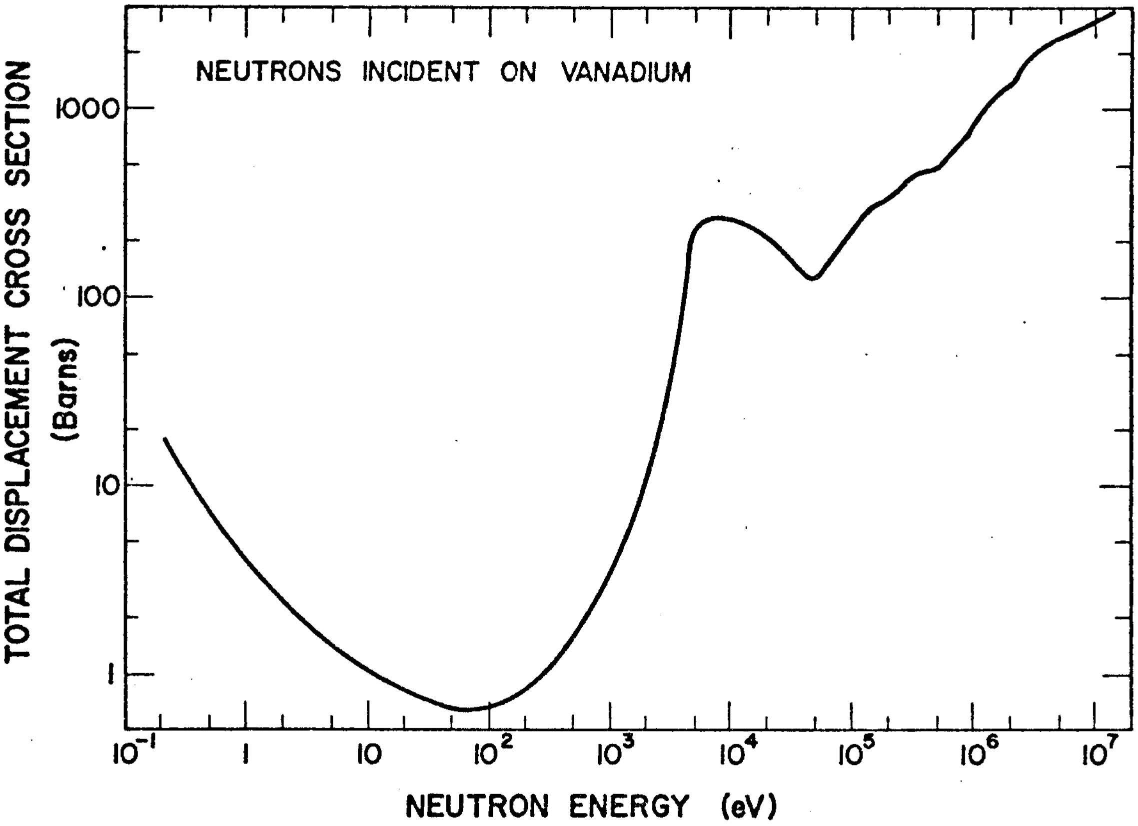

FIGURE 1. The total displacement cross section in neutron irradiated vanadium. (From the calculations of Gabriel et al.(31).)

A similar type of expression holds for the hydrogen production rate. The gas production rates are important when one is trying to simulate a neutron environment by simultaneously injecting gas atoms (He, H, or both) while irradiating with heavy-ions.

Charged-Particle Irradiations

When a solid is irradiated with energetic ions, the incident ions produce energetic PKA's and subsequent cascade damage as they penetrate the material. The resulting damage is similar to neutron damage. The disadvantages of such irradiations are short range, thus narrow damage zone, and some uncertainty in the calculation of damage for each irradiation.

When a charged-particle passes through a solid, it loses energy by two important mechanisms. It can excite or eject atomic electrons, or it can transfer energy to a lattice atom as a whole(32). If the kinetic energy of the struck atom, T, is sufficiently large ($T \geq E_d$), the atom will be displaced from its lattice position. The ejected or excited electrons, because of small momenta, do not result in displaced atoms. Therefore, only those collisions which transfer energy as a whole to the lattice atoms will result in displacements. These collisions are often labeled "nuclear collisions" in the literature.

The most widely accepted model for determining the energy loss of a charged-particle is the energy partition model of Lindhard, Scharff, and Schiott(33) (often referred to as LSS). In the

LSS model the total energy loss of a charged-particle is partitioned into separate electronic and nuclear terms, and expressions for these terms are derived using a Thomas-Fermi treatment. The results of the LSS model are an electronic stopping power proportional to the velocity of the incident ion and a nuclear stopping power expressed in terms of a universal differential scattering cross section.

Before proceeding further it is necessary to define the dimensionless measures of energy and range used in the LSS model. These reduced units are

$$\varepsilon = E/E_L \tag{14}$$

and

$$\rho = R/R_L \tag{15}$$

where

$$E_L = Z_1Z_2e^2(M_1 + M_2)/aM_2 \tag{16}$$

and

$$R_L = (M_1 + M_2)^2/(4\pi a^2NM_1M_2). \tag{17}$$

In these equations "a" is the screening length given by

$$a = 0.8853(\hbar^2/me^2)(Z_1^{2/3} + Z_2^{2/3})^{-\frac{1}{2}} \tag{18}$$

m and e are the mass and charge of the electron, Z is the atomic number, M is the mass, N is the density of target atoms, E is the energy of the incident ion, and R is the path length of the ion. (Subscripts 1 and 2 refer to the incident ion and target atoms, respectively.)

Through a perturbation procedure, the LSS model derives an universal differential scattering cross section for nuclear collisions, $d\sigma$, for scattering in a screened potential $U(r)$. Their result is

$$d\sigma = \pi a^2 f(t^{\frac{1}{2}})/(2t^{3/2})\ dt \tag{19}$$

where $t^{\frac{1}{2}} = \varepsilon \sin(\psi/2)$ and ψ is the center of mass scattering angle. The function $f(t^{\frac{1}{2}})$ is dependent upon the potential $U(r)$ chosen. Figure 2 shows the function $f(t^{\frac{1}{2}})$ which has been numerically calculated by LSS from a Thomas-Fermi potential. Analytical approximations of $f(t^{\frac{1}{2}})$ are often used; one such approximation for a Thomas-Fermi potential is given by Winterbon et. al.(34) to be

$$f(t^{\frac{1}{2}}) = \lambda t^{1/6} \{1 + (2\lambda t^{2/3})^{2/3}\}^{-3/2} \tag{20}$$

with $\lambda = 1.309$.

In reduced units the nuclear stopping power is

$$(d\varepsilon/d\rho)_n = (R_L/E_L)(dE/dR)_n \tag{21}$$

where

$$(dE/dR)_n = N \int t\ d\sigma. \tag{22}$$

Using Eq. 22 the following expression for $(d\varepsilon/d\rho)_n$ is easily derived:

$$(d\varepsilon/d\rho)_n = \int_0^E dx\ f(x)/\varepsilon \tag{23}$$

where $x = t^{\frac{1}{2}}$.

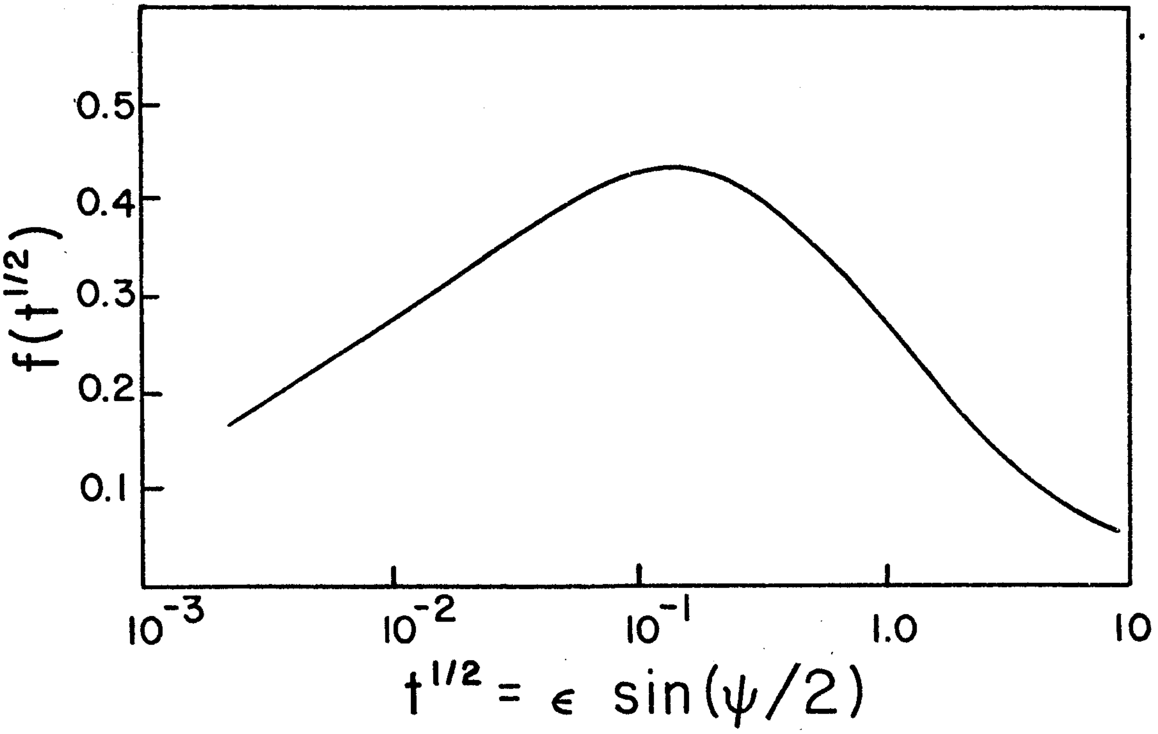

FIGURE 2. The LSS function $f(t^{\frac{1}{2}})$ numerically calculated from a Thomas-Fermi potential - Lindhard, Scharff, and Schiott(33).

In an earlier report Lindhard and Scharff(35) proposed that the electronic stopping power is proportional to the ion velicity for velocities $v < v_o Z_1^{2/3}$ ($v_o = 2\pi e^2/h$); that is, for ion energies $E < E_{lim}$. On the basis of this report, the electronic stopping power in the LSS model is given (in reduced units) by

$$(d\varepsilon/d\rho)_e = k\varepsilon^{\frac{1}{2}} \tag{24}$$

where k is a constant in the LSS model depending on Z_1, Z_2, A_1, and A_2 (A is the atomic mass number). Except in the case of $Z_1 << Z_2$, k is normally on the order of 0.1 to 0.2. (For vanadium ions incident on vanadium, k = 0.151 and E_{lim} = 83 MeV; for copper ions incident on vanadium, k = 0.142 and E_{lim} = 140 MeV.)

The nuclear and electronic stopping powers are shown in Figure 3 with k = 0.15 in the electronic stopping expression.

By knowing the electronic and nuclear stopping powers, the average total path length of an incident ion with reduced energy ε_o is

$$\bar{\rho} = \int_o^{\varepsilon_o} \left[(d\varepsilon/d\rho)_n + (d\varepsilon/d\rho)_e\right]^{-1} d\varepsilon. \tag{25}$$

The above formula is not quite correct since the slowing down process involves statistical fluctuation in the energy loss. Of greater experimental interest is the projected range or penetration depth of the incident particle given by

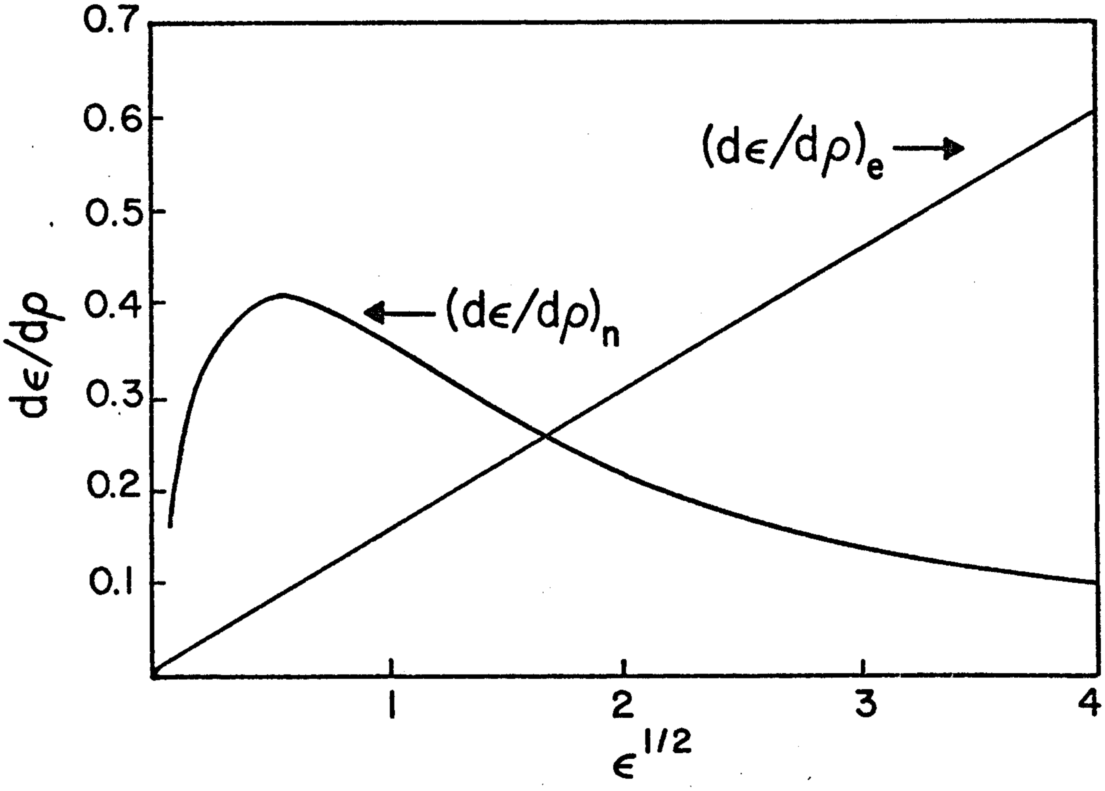

FIGURE 3. Nuclear and electronic stopping powers in reduced units from the LSS model (The electronic stopping is for k = 0.15) - Lindhard, Scharff, and Schiott(33).

$$\rho_d = \int_0^{\rho} <\cos \phi> \quad d\rho' \tag{26}$$

where ϕ is the lab scattering angle.

The dpa value for charged-particle irradiations is related to the nuclear stopping power of the incident particle at any given depth. If ε_D is defined as the reduced damage energy (energy which is ultimately given to recoiling atoms), then the damage energy deposited per unit penetration depth is (from Eq. 23).

$$(d\varepsilon_D/d\rho_d) = (1/ <\cos \phi>) \int_0^{\varepsilon} \omega_D(x) f(x)/\varepsilon \, dx \tag{27}$$

where $\omega_D(x)$ is the damage efficiency defined in Appendix A. The dpa value as a function of energy (and therefore depth) is given by

$$\text{dpa} = (J/N)(E_L/R_L)\ (\beta/2E_d)(d\varepsilon_D/d\rho_d) \tag{28}$$

where J is the incident ion density (ions/cm^2) and $\beta/2E_d$ is a factor defined in Appendix A.

In the above discussion it was assumed that the mono-energetic charged-particles have an unique range. In reality the slowing down process is statistical in nature, and the fluctuations in the electronic and nuclear energy losses contribute to the straggling and results in a spread in the energy of the ions at any given depth. Corrections to the above results should therefore be made to account for the straggling.

The general procedure is to estimate the energy straggling by relating it to the range straggling$^{(19)}$. The distribution of penetration depths is assumed to Gaussian$^{(36)}$ and is given by

$$P(\rho_d) = \frac{1}{\sqrt{2\pi}\;\Delta\rho_d} \exp\left[\frac{-(\rho_d - \bar{\rho}_d)^2}{2(\Delta\rho_d)^2} \right] \tag{29}$$

where $(\Delta\rho_d)^2 = \overline{\rho_d^{\,2}} - (\bar{\rho}_d)^2$. Using this result the dpa value as a function of ρ_d is

$$\mathrm{dpa}(\rho_d) = \frac{J}{N}\,\frac{E_L}{R_L}\,\frac{\beta}{2E_d} \int_{\rho_d}^{\infty} P(\rho'_d)\,\frac{d\varepsilon_D}{d\rho_d}(\rho'_d - \rho_d)\,d\rho'_d \tag{30}$$

where

$\frac{d\varepsilon_D}{d\rho_d}(\rho'_d - \rho_d)$ = the damage energy deposited per unit depth by an ion whose penetration depth is $(\rho'_d - \rho_d)$.

A computer code (E-DEP-1) by Manning and Mueller$^{(37,38)}$ which calculates dpa values in the manner described above has been adapted for use on the U.W. computer. The results of the computer calculations are shown in Figure 4 for 14 MeV copper ions incident on a vanadium target; the total fluence for the irradiation is 1.0×10^{16} ions/cm^2 and a value of $E_d = 43$ eV is assumed for vanadium (see Appendix A for determination of E_d).

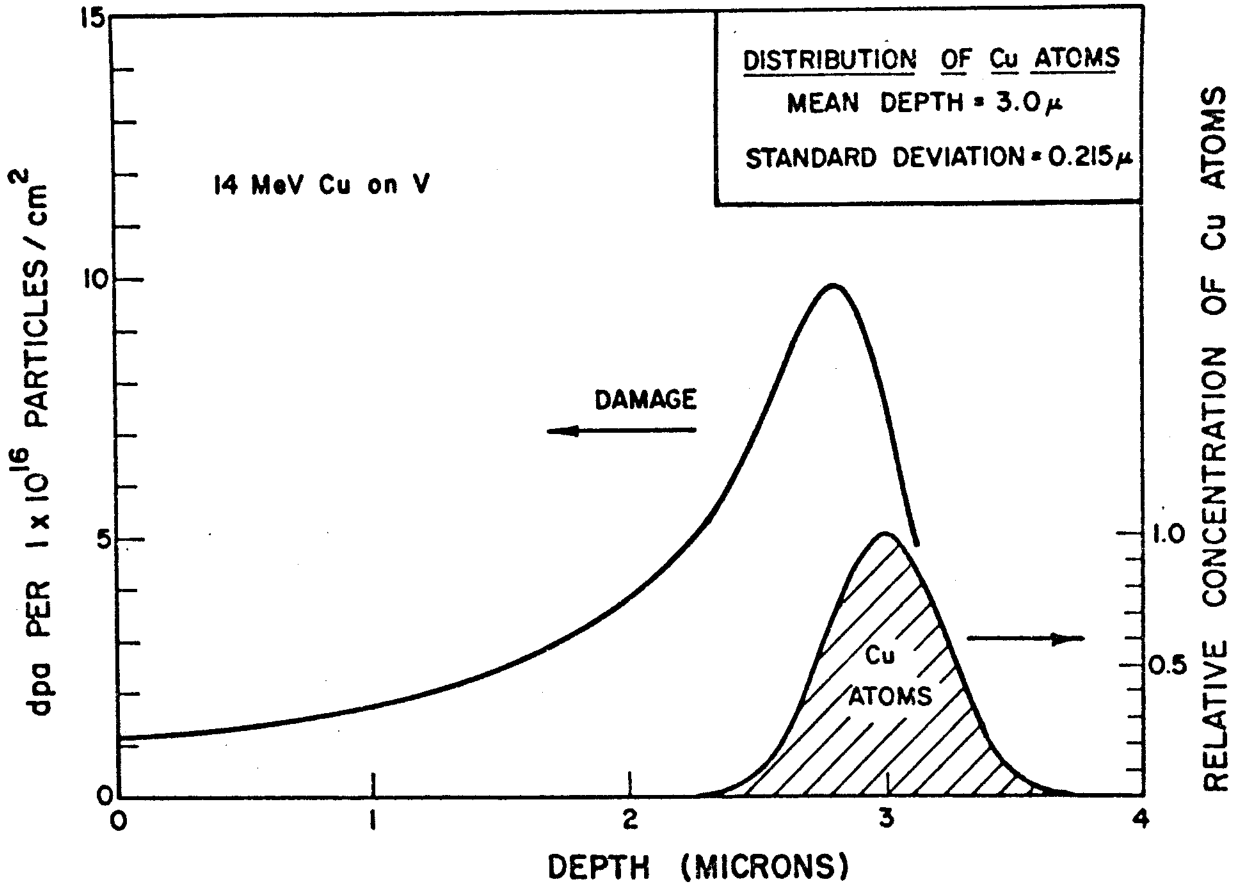

FIGURE 4. Depth distribution of damage and copper atoms in vanadium irradiated with 14 MeV copper ions as calculated using the E-DEP-1 code of Manning and Mueller(37,38) (E_d = 43 eV).

Electron Irradiations

Electrons with high enough energies ($\sim$1 MeV) are also able to produce displacements by direct interaction through the Coulomb potential with the nuclei of a solid(30). Unlike irradiations with neutrons or heavy-ions, electron irradiations (with energies less than a few MeV) do not produce cascades and only result in a small number of displacements per collision ($\sim$1-2). With the advent of High Voltage Electron Microscopy (HVEM) in irradiation damage studies, the use of electron irradiations have a particular advantage in that the damage may be observed while it is produced.

The energy transferred to a lattice atom by an electron scattered through an angle ψ in the center of mass coordinate system is given by

$$T = T_m \sin^2 (\psi/2) \tag{31}$$

where T_m, the maximum energy which could be transferred, is

$$T_m = 2 \frac{E}{Mc^2} (E + 2mc^2). \tag{32}$$

In the above equation E is the kinetic energy of the electron, M the mass of the target atom, m the rest mass of the electron, and c the velocity of light.

The total cross section for producing displacements (primaries plus secondaries) by an electron of energy E can be written as

$$\sigma_{tot}(E, E_d) = \int_{E_d}^{T_m} \nu(T) \frac{d\sigma}{dt} dT \qquad (33)$$

where E_d is the displacement energy as defined before, $\nu(T)$ is given by the simple Kinchin and Pease model(39) in Appendix A (Eq.'s A-1), and $d\sigma/dT$ is the differential scattering cross section for transferring an energy T to an atom by an electron of energy E. . The integral of Eq. 33 can be solved analytically for the McKinley-Feshback(40) form of $d\sigma/dT$, but numerical solution is necessary if using the Mott(41,42) series expansion of $d\sigma/dT$.

O.S. Oen(43) has used the Mott series to calculate the displacement cross section (Eq. 33) of 37 different elements for electron energies ranging up to about 150 MeV. The results are tabulated for different values of E_d. The results for vanadium, using E_d = 43 eV, are plotted in Figure 5.

Once the displacement cross section is determined, the dpa rate is given by

$$\text{dpa-rate} = \phi(E)\, \sigma_{tot}\, (E, E_d) \qquad (34)$$

where $\phi(E)$ is the flux of incident electrons. If the electron beam is not monoenergetic, then Eq. 34 must be integrated over the energy spectrum of the electrons.

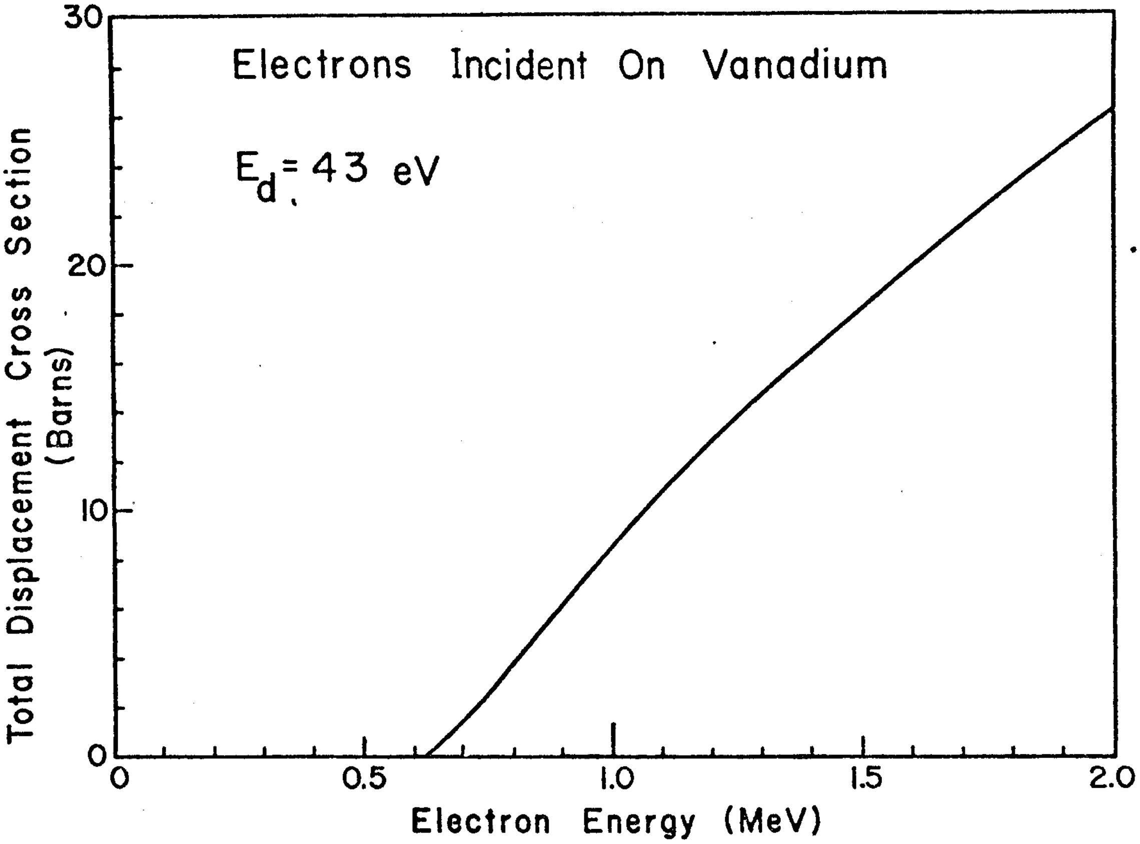

FIGURE 5. The total displacement cross section in electron irradiated vanadium (From the tables of Oen(43)).

CHAPTER III

THEORY OF VOID SWELLING

General Conditions For Void Swelling

The nature of void swelling in metals is now qualitatively understood. There are four general conditions necessary for void swelling to occur. They are:

1. The supersaturation of vacancies and interstitials must be large enough to allow voids and dislocation loops to nucleate and grow.
2. Both vacancies and interstitials must be mobile in the solid.
3. An excess vacancy concentration (relative to the interstitial concentration) must be established in the solid. This requires a preferential sink for interstitials.
4. Trace quantities of insoluble gases or surface active impurities must be present to stabilize the void embryos and prevent collapse to vacancy loops.

Irradiation of the metal lattice produces a large number of vacancy-interstitial pairs. A majority of these defects recombine with each other or migrate to various sinks (dislocations, voids, precipitates, and grain boundaries) in the solid. However, the dynamic balance between defect production and loss during irradiation allows the concentrations of point defects to greatly exceed the thermal equilibrium concentrations. This supersaturation of vacancies and interstitials results in the nucleation and subsequent growth of voids and dislocation loops (vacancy loops may shrink after forming). If the temperature becomes too high ($\sim 0.5T_m$), then the irradiation induced concentration of vacancies approaches the thermal equilibrium value and void nucleation and growth ceases. The vacancy supersaturation, S_v, is given by

$$S_v = C_v/C_v^e \tag{35}$$

where C_v is the irradiation induced vacancy concentration and C_v^e is the thermal equilibrium vacancy concentration.

In order that voids and dislocation loops may both nucleate and grow it is necessary that the vacancies and interstitials be able to migrate. Interstitials easily meet this requirement since they migrate in metals at very low temperatures(29). Vacancies do not become mobile until the temperature of the metal exceeds approximately 0.2 T_m; this accounts for the lower temperature limit on void formation.

It is generally assumed that there is no preferential attraction for vacancies or interstitials at the surfaces of voids which have grown beyond the critical nucleus size. Both vacancies and interstitials randomly migrate to the void surfaces. Therefore, an excess vacancy concentration is needed to assure the arrival of more vacancies than interstitials at the void surfaces; otherwise, the voids would not nucleate and grow. Since the irradiation produces an equal number of vacancies and interstitials, a preferential sink for interstitials must exist if there is to be an excess vacancy concentration. Irradiation produced dislocation loops and the pre-existing dislocation microstructure act as such a sink. The presence of the dislocations results in a slight (a few percent) preferential drift of the interstitials to the dislocations due to the long range elastic interaction between interstitials and dislocations(3,44-46). This preferential drift results in the net excess vacancy concentration needed.

The relative stability of voids and vacancy loops can be assessed by comparing the energy of a void of m vacancies with the energy of a dislocation loop of m vacancies. For a spherical void this energy is given by(47,48)

$$E_{void} = 4\pi\gamma(3\Omega m/4\pi)^{2/3} \tag{36}$$

where γ is the surface energy and Ω is the atomic volume. The energy of a circular perfect dislocation loop of radius R_L composed of m vacancies is given by(48)

$$E_{loop} = 2\pi R_L G b^2 \tag{37}$$

where G is the shear modulus and b is the Burgers vector. In body-centered cubic (bcc) metals, the vacancies generally condense on {110} planes in which the area per atom is $a_o^2/\sqrt{2}$ (a_o is the lattice constant). Therefore, the radius of a vacancy loop formed by the condensation of m vacancies on one of the {110} planes in a bcc metal is

$$R_L = (\sqrt{2}\, m\Omega/\pi a_o)^{\frac{1}{2}} \qquad (38)$$

where $\Omega = a_o^3/2$ is the atomic volume in the bcc crystal structure. The energy of the perfect dislocation loop of m vacancies in a bcc metal is given by

$$E_{loop} = 2\pi G b^2 (\sqrt{2} m\Omega/\pi a_o)^{\frac{1}{2}}. \qquad (39)$$

A comparison of the void and loop energies in Eqs. 36 and 39 will only result in qualitative conclusions concerning the relative stability of the two types of vacancy clusters. This is because the energies are fairly close together and the important parameters, G and γ, are not accurately known. It is generally accepted(47,48) that the void is the stable defect cluster for small m (less than several thousand vacancies); but, as m increases, the vacancy loop is the energetically favored cluster and the voids (with diameters greater than several tens of angstroms) will collapse. However, it is possible for large voids to be stable if the void energy, E_{void}, is reduced by other factors. For example, the void energy can be lowered by the presence of insoluble gas (such as helium) within the void cavity which exerts a positive pressure on the void surface, or the energy can be lowered through a reduction in the surface energy, γ, by surface active impurities. The stability of large voids has been demonstrated by the large voids (m greater than 10^5 vacancies and diameters greater than 200 Å) that have been reported(5-12).

The remainder of this chapter will discuss in more detail dislocation loop formation, void nucleation, and void growth.

Loop Formation

The nucleation and growth of dislocation loops has not been as extensively investigated (both theoretically and experimentally) as the phenomenon of void formation; however, there are some aspects of loop nucleation and growth which are understood and which will be discussed below.

Vacancy and interstitial loops nucleate because of the supersaturation of point defects generated in the metal lattice during irradiation. Vacancies may condense out as voids or vacancy loops; interstitials, on the other hand, only condense out as interstitial loops. (It is important to keep in mind that the majority of the vacancies and interstitials recombine or annihilate at various sinks in the solid.) Point defects generally condense on close-packed planes to form dislocation loops; in the bcc metals, the loops normally form on {110} planes, but unfault by shearing over to a glissile configuration at an early stage in their formation. Since all dislocations preferentially attract interstitials, vacancy loops should have an extremely difficult time nucleating and, as will be shown, should shrink and not grow if formed.

The incubation time for nucleating loops is very short(49,50) when compared to the incubation time for voids; thus, the dislocation loop microstructure forms very quickly and is fully developed before the steady state void nucleation begins. The equations governing loop nucleation are identical to the equations governing void nucleation (see following section) with the exception that the free energy expressions are changed. Russell and Powell(49) showed that interstitials have a large effect on the vacancy loop nucleation rates and may reduce the nucleation rate to zero. In addition, insoluble gas atoms can interfere with vacancy loop nucleation by promoting void nucleation. In the case of interstitial loop nucleation, they showed that the nucleation rates are not as sensitive to the presence of vacancies.

So far only what might be considered as actual nucleation of vacancy loops has been treated, and it has been shown(49) that under such a treatment vacancy loop nucleation is extremely difficult. There are, however, other means by which vacancy loops can form and which in a strict sense cannot be considered as nucleation. One of the alternative means by which vacancy loops can form is by the collapse of nucleated voids (possibly plate-like voids) as has already been mentioned at the beginning of this chapter. Another effect that may result in vacancy loop formation is the collapse of the vacancy-rich center of a collision cascade in neutron or heavy-ion irradiated materials(51). Levy(52) has also proposed the formation of vacancy loops by the interaction of a climbing dislocation with existing interstitial loops or pinning sites. If vacancy loops form by any of these mechanisms, their fate may be explained by growth theory (discussed below) which predicts that the vacancy loops will shrink unless the interstitial bias is reduced.

The interstitial loop concentration increases very rapidly (due to the short incubation time and highly mobility) and saturates at a level determined by the pre-irradiation microstructure, the temperature, and the dose rate. The equilibrium concentration of interstitial loops, C_L^i, after completion of nucleation (at saturation) is given by Eyre$^{(51)}$ to be

$$C_L^i = C_o^i K^{\frac{1}{2}} \exp(-E_m^i/2kT) \tag{40}$$

where C_o^i is a geometrical constant, K is the defect production rate, and E_m^i is the interstitial migration energy.

The growth rates of unfaulted dislocation loops (loops unfault at an early stage in bcc metals) during irradiation are governed by the following rate equations$^{(51)}$:

for interstitial loops

$$(dr_L/dt)_i = (1/b)\{Z_iD_iC_i - D_vC_v + D_vC_v^e \exp(-F_{el}b^2/kT)\} \tag{41}$$

and for vacancy loops

$$(dr_L/dt)_v = (1/b)\{D_vC_v - Z_iD_iC_i - D_vC_v^e \exp(-F_{el}b^2/kT)\} \tag{42}$$

where C_i and C_v are the interstitial and vacancy concentrations respectively, D_i and D_v are their diffusivities, F_{el} is the elastic energy of the loop, b is its Burgers vector, and Z_i is the bias term defining the preferential attraction of dislocations for interstitials. Values for C_i and C_v are found by solving the rate equations (Eqs. 51 and 52) in the Void Growth section of this chapter. The important point to emerge from Eqs. 41 and 42 is that interstitial loops are basically stable defect clusters which can undergo continuous growth during irradiation, while vacancy loops are basically unstable defect clusters which undergo bias driven shrinkage at low temperatures ($Z_iD_iC_i > D_vC_v$) and shrinkage by thermal vacancy emission at higher temperatures ($D_vC_v^e$ becomes appreciable). The vacancy loops may be stable and undergo growth if there is a large inbalance in C_v and C_i ($C_i << C_v$) due to some other sink in the solid which has a very large bias for interstitials; the vacancy loops may also grow if impurity atmospheres around the vacancy loops (dislocation poisoning) reduce their preferential attraction for interstitials$^{(53)}$ or affect the thermal emission of vacancies from the loops.

Void Nucleation

Void nucleation, which refers to the rate at which small void embryos appear in the solid, is the least understood process of void formation. Once nucleated, the voids are stable vacancy clusters which may undergo further growth. The void nucleation rate which determines the final void density is of central importance in the understanding and control of swelling in irradiated metals.

Nucleation is generally treated as a separate process that precedes growth. This treatment considerably simplifies the conservation equations and most theories of void formation in metals have adopted the "nucleation followed by growth" approach(48). It is important, however, to recognize that nucleation of new voids may proceed in parallel with the growth of existing voids.

The nucleation of voids in metals can be termed as homogeneous or as heterogeneous. Homogeneous nucleation refers to the formation of small void embroyos by the statistical agglomeration of individual point defects undergoing random walks in the solid. Heterogeneous nucleation refers to the formation of voids on existing structural features of the solid. There is no general consensus on which void nucleation mechanism is predominant, and nucleation probably occurs by a combination of homogeneous and heterogeneous processes.

Inert gases, such as the helium generated by (n,α) reactions, are known to have a strong effect on void nucleation. The primary role of the gas is to help support the surface energy force through internal pressure. The gas enters the nucleation process by simultaneously precipitating with vacancies and interstitials or by the heterogeneous nucleation of voids on single gas atoms or gas atom clusters. Although helium can have an important role in void nucleation(25), early studies with electrons(54) and charged particles(22,55) indicated that the need for helium was not an absolute requirement.

Soluble gases such as oxygen, nitrogen, and hydrogen and such solutes as carbon have also been observed to affect void nucleation(52,56). These solutes may have an indirect effect on void nucleation by serving as traps for vacancies, interstitials, and gas atoms or by changing various sink biases through impurity poisoning of the elastic strain field surrounding the sinks. These solutes may also directly affect the nucleation process by adsorbing at the void: matrix interface and lowering the surface energy.

The understanding of void nucleation in metals is not simply a matter of applying classical nucleation to the system. Classical theory was developed to explain the condensation of a single species; on the other hand, void nucleation involves at least two species (the vacancy and its antiparticle the interstitial). A void can grow by adding a vacancy or by releasing as interstitial, which is highly improbable; a void can shrink by adding an interstitial or by emitting a vacancy. If helium or some other impurity is involved in the nucleation process, then three species must be considered in the nucleation theory.

The first theoretical treatment of void nucleation was developed simultaneously and independently by Katz and Wiedersich(57,58) and by Russell(59) on the homogeneous nucleation of voids in the absence of gas atoms and solutes. Since that time further theoretical studies by Russell(60-64), Katz and Wiedersich(65,66), Wiedersich, Burton, and Katz(67), Wiedersich(68), and Loh(69) have accounted for the role of gas atoms (soluble and insoluble) and impurity atoms, along with vacancies and interstitials, in void nucleation. More recently, time dependent void nucleation has been considered(70). Russell has now developed and will soon publish(71) an updated theory of void nucleation. The remainder of this section will discuss the particular approach of Russell to void nucleation.

Initially Russell(59) derived a rate equation from kinetic considerations by expressing the nucleation rate as the flux of clusters between adjacent size classes in a one dimensional phase space consisting of cluster size. He(60-64) then expanded his model to a two dimensional phase space consisting of cluster size (net number of vacancies) and the number of impurity atoms associated with each cluster. The void is then characterized by the net number of vacant lattice sites, n, and the number of associated impurities, x.

The most probably behavior of a void consisting of n vacancies and x impurities is described by the fluxes in the n:x phase space. The fluxes are given by(60,62,63,71)

$$J_n(n,x) = \beta_v\rho - \alpha_v\rho - \beta_i\rho \tag{43}$$

$$J_x(n,x) = \beta_x\rho - \alpha_x\rho - xK_x^c\rho \tag{44}$$

where β_v, β_i, and β_x are, respectively, the arrival rates of vacancies, interstitials, and impurity atoms; α_v and α_x are the rate of vacancy and impurity emission, respectively; ρ is the concentration; and K_x^c is the probability of radiation resolution of an impurity from the void.

By applying the continuity equation, the fluxes and concentration are related by the following difference equation:

$$\Delta_t\rho(n,x) + \Delta_n J_n + \Delta_x J_x = 0 \tag{45}$$

where the Δ's are the difference operators.

For the case of homogeneous nucleation of voids in the absence of impurities, the x-dependence in Eq. 45 is dropped, and Russell(59) has shown that the steady state nucleation rate (in the formalism of classical nucleation theory) is given by

$$J_k = Z'\beta_k N_o \exp(-\Delta G_k'/kT) \tag{46}$$

where Z' is a pseudo-Zeldovich factor, β_k is β_v evaluated at the critical nucleus size (n = k), N_o is the number of nucleation sites, and G_k' is the activation barrier for voids in the presence of interstitials. The activation barrier is related to the free energy by the equation

$$G'_k = kT \sum_{j=0}^{k-1} \ln \{\beta_i/\beta_v + \exp(\delta G_j^o/kt)\} \qquad (47)$$

where δG_j^o is the difference between the free energies of forming voids of j+1 and j vacancies ($\delta G_j^o = \Delta G_{j+1}^o - \Delta G_j^o$). The free energy change in forming a void of n vacancies (in the capillarity model) is given by(48,71)

$$\Delta G_n^o = -nkT \ln(S_v) + (36\pi\Omega^2)^{1/3} \gamma n^{2/3}. \qquad (48)$$

Powell and Russell(72) have evaluated the above expressions for the case of stainless steel at constant temperature (500 °C). The nucleation rates they calculated were much too low to account for experimentally observed void densities; this is to be expected since they did not take into account the effect of helium and other impurities. It is expected that similar calculations in other metals will also yield nucleation rates too low to account for the void densities that have been observed.

Russell(60) has shown that in the general case (represented by Eqs. 43-45) where vacancies, interstitials, and impurities are present it is impossible to solve the equations analytically. The equations can, however, be solved numerically, but this has been shown to be extremely time consuming(62).

There are, nevertheless, two limiting cases where some of the formalism of classical nucleation theory may be applied. The equations governing nucleation in the absence of impurities (Eqs. 46 and 47) are applicable in the presence of impurities as long as the state of the void is completely determined by the number of vacancies it contains. This will be the case if the impurities are immobile, the void will contain only the impurity it started with. It is also the case if the impurities are highly mobile and are able to reach equilibrium with the void between vacancy captures, in which case the impurity content is determined by the void size. In both cases the impurities may be gaseous or non-gaseous and their effect on the nucleation rate is through changes in the free energy, ΔG_n^o, Russell(61,62) has shown that the effect of the impurities in these limiting cases is to increase the nucleation rate. The increases in the nucleation rate can be substantial and can come closer to explaining the experimentally observed void densities.

In all the discussion so far it has been assumed that voids are neutral (unbiased) sinks; that is, they have no net attraction for either interstitials or vacancies. Recent calculations by Wolfer and Yoo(73) have shown that small voids may have a large bias for interstitials. They found that this bias, which is the result of a free surface image force interaction, significantly reduced the nucleation rate. They did, however, conclude that void nucleation was possible if impurities segregated to the voids and reduced the void bias.

Void Growth

In the absence of a comprehensive theory of void nucleation, all models for void growth (and hence swelling) assume a pre-existing density of embryonic voids. If early completion of nucleation is assumed, then the void density in the models remains equal to the pre-existing density; otherwise, the void density is periodically increased to account for continuous nucleation. In the case of constant void density, swelling results only from the growth of existing voids. When there is continuous nucleation, however, swelling results from both void growth and increasing void density.

The theoretical treatment of void growth has generally followed two distinct approaches: the cellular models of Bullough and Perrin(44,74-76) and the rate theory models of Wiedersich(77,78), Harkness and Li(79,80), and Brailsford and Bullough(81-83). In their cellular model, Bullough and Perrin study the growth of a typical void situated at the center of a spherical cell; the radius of the cell is determined by the average void concentration. Coupled nonlinear diffusion equations in the cell are solved to yield the net vacancy flux to the void and hence the growth rate. On the other hand, the rate theory models formulate basic rate equations for the spatially averaged point defect concentrations and solve for the net accumulation rate of vacancies at voids. The following discussion will consider only the rate theory model of Brailsford and Bullough(81-83) since it is mathematically simpler, more physically correct, and more successful than the cellular model.

The rate theory approach has been preferred since it involves only the solution of two simultaneous quadratic equations. The fundamental rate equations for the steady state fractional vacancy and interstitial concentrations, C_v and C_i, are respectively

$$dC_v/dt = 0 = K' - D_v C_v k_v^2 - \alpha C_i C_v \tag{49}$$

and

$$dC_i/dt = 0 = K - D_i C_i k_i^2 - \alpha C_i C_v \tag{50}$$

where K is the defect production rate; K' is the effective vacancy generation rate given by K plus the total thermal vacancy emission rate, K_e, from all sinks in the material ($K' = K + K_e$); D_v and D_i are the vacancy and interstitial diffusion constants, respectively; α is the recombination coefficient; and k_v^{-1} and k_i^{-1} are, respectively, the mean free paths of a vacancy and interstitial in the presence of various sinks in the solid. Brailsford and Bullough(81) have determined values for k_v^2 and k_i^2 by calculating different effective sink strengths.

The solutions to Eqs. 49 and 50 are

$$C_v = D_i k_i^2/2\alpha \left[-(1 - \mu) + \{(1 + \mu)^2 + \eta\}^{\frac{1}{2}}\right] \tag{51}$$

$$C_i = D_v k_v^2/2\alpha \left[-(1 + \mu) + \{(1 + \mu)^2 + \eta\}^{\frac{1}{2}}\right] \tag{52}$$

where

$$\eta = 4\alpha K/D_i D_v k_i^2 k_v^2 \tag{53}$$

and

$$\mu = K_e \, \eta/4K \tag{54}$$

The swelling rate can be determined directly by evaluating the net flow of defects into the voids and is given by

$$d(\Delta V/V)/dt = 4\pi R_V \rho_V (D_v C_v - D_i C_i - D_v \bar{C}_v) \tag{55}$$

where ρ_V is the void density, R_V is the average void radius, and $\bar{C}_v$ accounts for the thermal emission of vacancies.

The rate theory of swelling developed by Brailsford and Bullough and briefly described above is limited to quasi-steady state conditions. It is difficult to apply such a theory in a case where the microstructure and defect concentrations are changing rapidly with time (such as in the first wall of an inertially confined fusion reactor). In order to understand void growth under such conditions, the rate theory model of Brailsford and Bullough has recently been upgraded by Ghoniem and Kulcinski$^{(84)}$ to include the fully dynamic case. The computer code, TRANSWELL, developed by

Ghoniem and Kulcinski(85) to solve the fully dynamic rate equations is also capable of solving the steady state equations which are applicable to the heavy-ion irradiations being carried out at the University of Wisconsin.

The important contribution of the theoretical models presented (both nucleation and growth) is not that they can make independent predictions of expected swelling, but that they serve to indicate which are the dominant physical properties.

CHAPTER IV

PREVIOUS STUDIES OF IRRADIATION DAMAGE IN VANADIUM

Neutron Irradiated Vanadium

Voids in vanadium were first observed in 1968 by Wiffen and Stiegler(86,87) in unalloyed vanadium that was used as cladding in a fuel irradiation experiment. The vanadium cladding was irradiated at 630°C to a fast neutron fluence of 1.7×10^{22} n/cm^2 in EBR-II. Further studies on neutron irradiated vanadium have shown that voids are {100} cubes and form at temperatures as low as 150°C (88) but most studies concentrated on the temperature range from 385°C to 750°C(89-96) and at fluences from 1.6×10^{20} n/cm^2 to 3.6×10^{22} n/cm^2. Voids were not observed at 800°C during neutron irradiation(91). A summary of these results is given in Table 1.

The temperature range where voids form in vanadium during neutron irradiation generally falls within the regime from 0.3 to 0.5 T_m, with the exception of the voids formed at 150°C which corresponds to 0.19 T_m. The formation of voids at 150°C is surprising in view of the reported Stage-III annealing peak in vanadium which is reported to be due to the annihilation of vacancies(97,98); however, the annealing peak at 175°C has also been attributed to the migration of oxygen(99,100,101) and the observance of voids at 150°C may support this view. Since the controversy concerning the

TABLE 1

VOID PARAMETERS IN NEUTRON IRRADIATED VANADIUM

Temperature (^{o}C)	Average Void Diameter (Angstroms)	Void Density (10^{15}voids/cm^3)	ΔV/V (%)	Fluence ($10^{22}n/cm^2$)	Total Interstitial Impurities (wt-ppm)	Reference
630	120	5.0	0.4	1.7	Not Given	86, 87
150	68	0.94	0.3	0.016	920	88
150	283	0.035	1.4	0.016	1400	
150	110	0.5	0.9	0.016	3000	
420	35	6.0	0.01	0.022	170	89, 90
630	70	1.0	0.02	0.037	170	
750	110	0.1	0.07	0.027	170	
335	140	0.34	0.05	0.05	5000	91
435	280	0.2	0.22	0.05	5000	
600	780	0.015	0.38	0.05	5000	
800	0	0	0	0.05	5000	
385	50	12	0.08	0.53	220	92
385	45	120	0.56	0.53	1250	
475	82	10.6	0.34	0.97	1000	
550	170	5.9	1.77	1.4	1000	
600	230	2.0	1.47	1.4	1000	
450	50	30.0	0.2	0.3	1000	93
465	98	16.0	1.04	1.1	365	94
525	102 - 168	1.2 - 8.0	0.3 - 1.1	1.1	365	
625	138	9.0	1.54	2.5	365	

TABLE 1 (continued)

Temperature (^{o}C)	Average Void Diameter (Angstroms)	Void Density (10^{15}voids/cm^3)	ΔV/V (%)	Fluence (10^{22}n/cm^2)	Total Interstitial Impurities (wt-ppm)	Reference
450	60	13.5	0.2	3.6	6 PZR[a]	
550	213	1.25	0.6	3.6	6 PZR	
600	258	0.94	0.8	3.6	6 PZR	
450	110	10.6	0.7	3.6	Commercial Purity	95
550	224	1.6	0.9	3.6	Commercial Purity	
600	281	0.32	0.4	3.6	Commercial Purity	
600	100 - 350	Not Given	0.1	0.16	30 appm[b]	
600	Not Given	Not Given	3.7	0.16	30 appm + 10 appm He	96
600	Not Given	Not Given	0.7	0.16	30 appm + 36 appm He	

a) Six Pass Zone Refined

b) Mostly Oxygen

annealing peak at 175°C has not been resolved and voids were observed at 150°C, it must be concluded that voids will form in neutron irradiated vanadium from 150°C to 750°C (0.2 to 0.5 T_m) and at fluences greater than 1.6 x 10^{20} n/cm^2 (about 0.3 dpa).

As expected, when the temperature dependence of void formation in vanadium was studied(89-92,94,95), the void size was found to increase with temperature while the void density decreased with temperature. The results of Table 1 indicate that the peak swelling occurs at a temperature between 550°C and 600°C during neutron irradiation. In particular, the results of Bartlett et al.(95) indicate that the peak swelling temperature occurs at 550°C in commercial purity vanadium and at 600°C in 6 PZR (six pass zone refined) vanadium. (The effect of impurities is discussed below).

As has already been mentioned and as indicated in Table 1, the interstitial impurities affect the formation of voids in vanadium. Elen(88) attempted to study void formation as a function of interstitial impurity content. He found that void size, density, and swelling varied with impurity content. Elen was unable to draw specific conclusions concerning the effect of each type of impurity but did observe an <u>increase</u> in swelling with higher oxygen content. Wiffen(92) also studied the effect of interstitial impurities on void formation in vanadium at 385°C and found that the void density was an order of magnitude higher in samples containing

1250 wt-ppm of interstitial impurities than in samples containing 220 wt-ppm impurities. This is contrary to the normal behavior where impurities tend to supress void formation. The lowering of the peak swelling temperature to 550°C in the commercial purity vanadium of Bartlett et al.(95) can be attributed to a slight increase in void size and density at 550°C. In the same study the commercial purity samples irradiated at 450°C and 600°C showed a slight decrease in void density and increase in void size when compared with the high purity samples. Clearly, much more work is needed to determine how the interstitial impurities affect void formation.

It has long been known that helium assists the nucleation of voids in pure metals. The work of Cambini et al.(96) illustrates this by the significant increase in swelling in vanadium pre-injected with 10 appm helium prior to neutron irradiation. They also found a sharp <u>decrease</u> in void swelling when the helium level was increased from 10 to 36 appm; they offered no explanation for this observation.

Radiation induced precipitates were observed in neutron irradiated vanadium by Elen(88-90), Wiffen(87,92), and Cambini(96). These precipitates are thought to result from contamination of the samples before and during the irradiation with carbon, oxygen, or nitrogen. Elen(90) described the precipitates as platelets showing stacking fault contrast and observed that the long axis of their projections on {111} planes is in the ⟨112⟩ directions. The precipitates reported by all three authors are thought to be the same plate-like precipitates, but no further analysis by any of the authors is given.

In addition to the work on pure vanadium, several investigators(88,89,92,94) have studied the alloying effect of titanium on void formation in vanadium. The addition of titanium was found to suppress void formation. Carlender et al.(94) suggest that this suppression may be explained by any of the following three mechanisms: 1) gettering of impurity interstitials necessary for void nucleation; 2) the formation of Ti-O precipitates to act as vacancy sinks; or 3) the addition of substitutional solute that could serve as point defect traps and promote recombination. The first two mechanisms are supported by post-irradiation observations of precipitates in all vanadium-titanium alloys and by internal friction measurements showing that the addition of titanium does remove oxygen from solution.

In the above studies of void formation in neutron irradiated vanadium, very little information concerning the dislocation loop structure is given. Elen(88-90) observed small interstitial loops of the a/2 ⟨111⟩ type, typical for bcc metals, and local clustering of similarly oriented loops. No data of loop size or density are given in any of the above studies. The post-irradiation annealing of dislocation loops in vanadium irradiated with neutrons (less than 10^{20} n/cm^2) at reactor ambient temperatures has also been studied(102,103). In general, the loops are only resolved as black dots before annealing; during annealing the loops were observed to grow as their density decreased. Shirashi et al.(103) observed the growth of vacancy loops during post-irradiation annealing of samples irradiated to 8.2 x 10^{19} n/cm^2 and the growth of interstitial loops during post-irradiation annealing of samples irradiated to fluences of 4.2 x 10^{19} n/cm^2 or less. They also found that the interstitial loops disappeared after annealing to temperatures greater than 500°C, a result of the interstitial loops growing into the developing dislocation network. The vacancy loops remained until the annealing temperature exceeded 630°C, a point where the thermal emission of vacancies is sufficient to cause the remaining loops to disappear.

Heavy-Ion Irradiated Vanadium

Heavy-ions were first used to irradiate vanadium by Kulcinski and Brimhall(104) in 1971. They found voids in vanadium irradiated with 7.5 MeV Ta ions at 700°C and 800°C to 30 to 22 dpa, respectively. They found no voids in samples irradiated at 900°C to 22 and 83 dpa. Further studies using Ni(105-108), Ta(107), and V(26,27,109) beams to irradiate vanadium have provided additional data on void formation in vanadium at the higher dpa levels unobtainable in present reactors, in convenient laboratory times. These studies span the temperature range from 650°C to

$900^{\circ}C$ with damage levels from 1 to 60 dpa and damage rates varying from 10^{-4} to 10^{-2} dpa/sec. The voids observed in these studies have been {100} cubes, but some {111} truncation of the cubes has been reported(26). A summary of these heavy-ion studies on vanadium is given in Table 2.

As indicated in Table 2, void formation in heavy-ion bombarded vanadium has only been studied in the temperature regime of 0.42 to 0.55 T_m; no previous attempt has been made to study voids below $650^{\circ}C$ under heavy-ion bombardment. The work by Santhanam et al.(105) using a 3.25 MeV nickel beam indicates that the peak swelling temperature is approximately $700^{\circ}C$ in high purity vanadium at a dose rate of 4×10^{-3} dpa/sec; however, in the same study, using the same beam and dose rate, they found the peak swelling temperature shifted to approximately $750^{\circ}C$ in commercial purity vanadium. In another study by Agarwal et al.(109) using a 3 MeV vanadium beam and a dose rate of 5.5×10^{-3} dpa/sec,the peak swelling temperature was again found to occur at approximately $700^{\circ}C$ in the high purity vanadium. It may be concluded that, independent of irradiating ion species, the peak swelling temperature in high purity vanadium irradiated with heavy-ions at a dose rate on the order of 5×10^{-3} dpa/sec is about $700^{\circ}C$. This represents a shift in the peak swelling temperature of about 100 to $150^{\circ}C$ by increasing the dose rate from approximately 3×10^{-6} dpa/sec for neutron irradiations to 5×10^{-3} dpa/sec for heavy-ion irradiations. As

TABLE 2

VOID PARAMETERS IN HEAVY-ION IRRADIATED VANADIUM

Temperature ($^{\circ}$C)	Average Void Size (Angstroms)	Void Density (10^{15} voids/cm^3)	$\Delta V/V$ (%)	Ion and Energy	dpa	C, O, N Impurities (wt-ppm)	Helium Content[a] (appm)	Reference
700	440	0.27	2.3	7.5 MeV Ta	30	1100	-	104
800	665	0.1	2.9	7.5 MeV Ta	22	1100	-	
900	None Observed	-	-	7.5 MeV Ta	22	1100	-	
900	None Observed	-	-	7.5 MeV Ta	83	1100	-	
650	120	0.97	0.21	3.25 MeV Ni	60	145	10	105
700	288	0.98	2.84	3.25 MeV Ni	60	145	10	
750	206	1.9	2.17	3.25 MeV Ni	60	145	10	
850	414, 407[b]	0.035,0.22[b]	0.38,1.83[b]	3.25 MeV Ni	60	145	10	
650	112	1.55	0.25	3.25 MeV Ni	60	145	100	
750	141	1.7	0.61	3.25 MeV Ni	60	145	100	
650	52	18.0	0.22	3.25 MeV Ni	60	1220	10	
750	225	1.95	2.8	3.25 MeV Ni	60	1220	10	
850	185	1.1	0.89	3.25 MeV Ni	60	1220	10	
650	45-55	8.7-19.0	0.13	3.25 MeV Ni	60	1220	100	
700	60	16.0	0.27	3.25 MeV Ni	60	1220	100	
750	107	2.4	0.40	3.25 MeV Ni	60	1220	100	
750	640	0.01	0.27	46 MeV Ni	2.4	1100	3	107
750	300	0.2	0.54	46 MeV Ni	9	1100	3	
750	350	0.17	0.73	46 MeV Ni	16	1100	3	
700	330	0.25	0.6	7.5 MeV Ta	15	1100	-	
800	550-900	0.005-0.05	0.7	7.5 MeV Ta	16	1100	-	
900	None Observed	-	-	7.5 MeV Ta	15	1100	-	

a) Pre-Injected

b) Near Grain boundary

TABLE 2 (continued)

Temperature (°C)	Average Void Size (Angstroms)	Void Density (10^{15} voids/cm^3)	ΔV/V (%)	Ion and Energy	dpa	C, O, N Impurities (wt-ppm)	Helium Content[a] (appm)	Reference
700	69	6.0	0.2	3 MeV V	2.4	145	-	26, 27
700	101	1.84	0.25	3 MeV V	4.26	145	-	
700	200	0.45-0.93	0.13-0.2	3 MeV V	7.0	145	-	
700	315-375	0.15-0.34	0.9 -1.5	3 MeV V	22.0	145	-	
700	344-412	0.23-0.37	1.6 -2.0	3 MeV V	34.0	145	-	
700	218-300	0.34-0.93	0.3 -0.48	3 MeV V	42.5	145	-	
700	337-425	0.30-0.52	0.85	3 MeV V	54.4	145	-	
650	68	5.5	0.12	3 MeV V	1	145	-	27[c]
650	110	2.0	0.18	3 MeV V	3.8	145	-	
650	150	1.7	0.4	3 MeV V	14	145	-	
650	70	3.0	0.076	3 MeV V	23	145	-	
650	64	2.6	0.052	3 MeV V	41	145	-	
650	61	2.0	0.03	3 MeV V	54	145	-	
750	350	1.7	0.73	46 MeV Ni	16	1100	3	108
750	None Observed	-	-	46 MeV Ni	16	1100	-	
750	120-142	3.0- 5.0	0.66-0.83	5 MeV Ni	50-60	1100	100-300[d]	
750	116-140	5.0-10.0	0.92-1.15	5 MeV Ni	50-60	1100	-	
650	125	1.0	0.13	3 MeV V	20	530	-	109[c]
720	700	0.12	2.44	3 MeV V	20	530	-	
750	580	0.1	1.4	3 MeV V	20	530	-	
810	750	0.025	1.0	3 MeV V	20	530	-	
900	680	0.0075	0.2	3 MeV V	20	530	-	

c) Void Parameters Estimated from Plotted Data
d) Simultaneously Injected

expected, the void size increased with temperature(109), the exception being the work by Santhanam et al.(105) where they found that the void density peaked at 750°C in the high purity vanadium samples.

The effect of the total damage dose, at constant temperature, on void formation in vanadium has been studied by the group at Argonne(26,27). Their results show that the swelling increased with dose, peaked, and then slowly decreased! The peak occurred at about 14 dpa for irradiations at 650°C and at about 34 dpa for irradiations at 700°C. The void size also increased with dose, reached a maximum, and then slowly decreased; the void density decreased with dose, reached a minimum, increased slightly, and then began to decrease again. The peak in the void size and the minimum in the void density both occurred at the same dose as the swelling peak. The behavior has been attributed to the profuse precipitation which begins to occur in the <u>high purity</u> vanadium (irradiated with 3 MeV vandium ions) at approximately the dose where the swelling and void size exhibit a peak. This precipitation will be discussed more fully below.

The only attempt, reported to date, to study the effect of interstitial impurities on void formation in vanadium has been by the group at Argonne. In their earlier work(105) they compared high purity vanadium (145 wt-ppm) with commercial purity (C.P.) vanadium (1220 wt-ppm) and found a shift in the peak swelling temperature (as already mentioned) and an increase in void density in the C.P. vanadium at lower temperatures (650 and 700°C). The increase in void density was attributed to interstitial impurity enhancement of the void nucleation process. The void size was reduced in the C.P. vanadium when compared with the high purity vanadium, and the total swelling (at the peak) remained about the same. In a more recent study(109), the group at Argonne found that the addition of interstitial solutes (nitrogen, carbon, and oxygen) strongly suppresses void swelling in vanadium. This is contrary to their previous work discussed above.

It has been shown that helium assists the nucleation of voids in vanadium under neutron irradiation(96). Several other studies(26,27,104,107-109) have shown that voids will form in vanadium in the absence of helium. The work of Brimhall(107,108) showed that helium was necessary when using 46 MeV Ni ions but was not necessary with 7.5 MeV Ta or 5 MeV Ni. The study of helium effects by Santhanam et al.(105) involved only samples doped to 10 and 100 appm helium. (No samples were irradiated without helium.) They found a bimodal distribution of voids and helium gas bubbles at 750°C in samples with 100 appm helium. The void density was also inhomogeneous from grain to grain at that temperature. In grains that contained a high density of bubbles, the void density was low; whereas, in grains with a lower density of bubbles, the void density increased. At 650°C the void density increased with helium content, but at 750°C the void density (neglecting helium bubbles) decreased as the helium content increased from 10 to 100 appm. The decrease in void density at 750°C may be due to the initial microstructure of the highly doped sample (100 appm) which consisted of a high concentration of small bubbles. These bubbles may be a predominant point defect sink and hence reduce the vacancy concentration to levels below that required for further nucleation. Brimhall and Simonen(108) concluded in their studies that helium was important at relatively low dose rates (8×10^{-4} dpa/sec), but had little effect at higher dose rates (1.2×10^{-2} dpa/sec).

There has been only one set of experimental results on the effect of bombarding ion species. The work of Santhanam et al.(105) using Ni ions can be compared with the work of Santhanam et al.(26) using V ions. In the nickel ion irradiations, precipitates were observed to form on the void faces; however, when the samples were irradiated with vanadium ions no precipitates were found on the void faces. In both experiments low energy ions were used and the damage was examined at a depth near the peak damage (also near end of range of the incident ion). The precipitates are most likely nickel and demonstrate the problem associated with non-self-ion irradiations, particularly if the damage is examined near the end of range.

It has already been mentioned that the group at Argonne observed profuse precipitation in their high purity vanadium irradiated with 3 MeV vanadium ions. These precipitates were only found in samples irradiated at 650°C and 700°C(27) (and recently at 550°C and 600°C in an unpublished study(110)). No precipitates were observed in samples irradiated at higher temperatures(109). The degree of precipitation was much more in the samples irradiated at 650°C than that found in the samples irradiated at 700°C. The amount of precipitation was also found to increase with dose. These precipitates were identified(109) as platelets, perhaps only one or two atom layers thick, with an {012} habit plane. The precipitates are now believed to be a metastable precipitate associated with carbon in vanadium(109).

The dislocation density was also measured in several of the above studies and was found to decrease with both dose(26,27) and temperature(109). Individual dislocation loops were not reported in any of these studies. This is not surprising since the loops can be expected to grow very quickly to large sizes at the high doses and temperatures employed. Such large loops are not individually resolvable but form the dislocation network which develops. The only study of loops in heavy-ion irradiated vanadium has been the work of Heershap and Schuller(111). They studied the post-irradiation annealing of vanadium irradiated with fast fission fragments and found that the vacancy loops, which were detected, annealed at 600°C.

There has been only one study to date of void formation in light-ion irradiated vanadium. In that study(112), vanadium was irradiated with 240 keV helium ions from 250 to 700°C and to damage levels ranging from 1.1 x 10^{-2} dpa to 22 dpa. The peak concentrations of helium which corresponds to these damage levels are 125 to 250,000 appm helium, respectively. With this amount of helium injected, it is hard to distinguish whether they were investigating helium bubble formation in vanadium or void formation. In any case, they found that swelling increased with dose at all temperatures. The peak in bubble concentration shifted to lower temperatures as the dose increased, and the bubble size was found to increase with temperature. Kaminsky et al.(113) have also irradiated vanadium with low energy helium ions. Their studies were on the phenomenon of surface blistering and are of no further interest in this investigation.

Electron Irradiated Vanadium

The studies of electron irradiated vanadium that are of interest here are those irradiations that determine the damage threshold, E_d^{th}, in vanadium by electron accelerator or High Voltage Electron Microscope (HVEM) irradiations and those HVEM irradiations of vanadium where loops were studied.

The value now accepted for E_d^{th} in vanadium is 26 ± 2 eV as determined by Miller and Chaplin(114). The value of E_d^{th} is determined by Eq. 32, which can be rewritten as

$$E_d^{th} = 2(E_{min}/Mc^2)(E_{min} + 2mc^2) \qquad (56)$$

where E_{min} is the minimum electron energy which will produce observable damage. The value of E_d^{th} given above is supported by further data generated by Jung and Lucki(115) and Chaplin et al.(116). These studies were performed with electron accelerators and the damage production was determined from changes in electrical resistivity at about 20°K for the work by Miller and Chaplin(114), at 6°K in the work by Chaplin et al.(116), and at 4.5°K in the study by Jung and Lucki(115).

In a study to determine the orientation dependence of the threshold displacement energy, Mitchell et al.(117) used an HVEM to irradiate various metals, including vanadium. In their study they increased the voltage of the HVEM until observable damage was produced. The irradiations were performed at ambient temperatures so that the interstitials clustered into observable defects. Exact crystallographic orientations were selected using extinction contours and Kikuchi lines. For the case of vanadium they observed sharp thresholds for all three orientations: <100>, <110>, and <111>; their results, given in Table 3, show that <100> is the easiest displacement direction.

TABLE 3

Orientation Dependence of E_d^{th} In Vanadium

Direction	E_d^{th} (eV)
<100>	30
<110>	39
<111>	34

The results of Table 3 are in fairly close agreement with the value of $E_d^{th} = 26$ eV determined in accelerator irradiations. The values determined are very important for HVEM irradiations where it is possible to irradiate a sample along an exact orientation. In such cases it is desirable to use the value of $E_d = E_d^{th}\langle hkl \rangle$ as the displacement energy instead of the value of $E_d = 5/3\ E_d^{th}$ which is commonly used for random orientations (see Appendix A).

HVEM irradiations of vanadium to study void or loop formation have not been reported in the literature. However, Saunderson and Weber(118) have irradiated vanadium in the University of Wisconsin HVEM at room temperature to study loop formation. Initial results at about 45°C indicate that the loops are interstitial in nature with Burgers vectors of the type $a/2\langle 111 \rangle$. At a damage level of 0.05 dpa the loop density was 2×10^{15} loops/cm^3 and the average loop diameter was 400 angstroms.

CHAPTER V

EXPERIMENTAL EQUIPMENT AND PROCEDURE

Heavy-Ion Irradiation Facility

The fundamental requirement of an irradiation facility for void formation studies is to produce a region of uniform damage within a sample while the sample is maintained at an elevated temperature. Furthermore, the damage region must be sufficiently removed from the surface (at least 0.5 microns(119)) so that the results are representative of the bulk material; the damage must also be produced at a reasonable rate (greater than 10^{-4} dpa/sec) to insure the production of sufficient damage in convenient irradiation times.

The high energy, heavy-ion beams used in this study are provided by the University of Wisconsin tandem Van de Graaff accelerator (HVEC model EN). The U.W. Heavy-Ion Irradiation Facility, which incorporates the tandem accelerator and has been fully described elsewhere(120,121), is shown schematically in Figure 6. Negative ions (Cu in this study), produced in the SPIGS (Sputter Penning Ion Gauge Source) heavy-ion source developed by Smith and Richards(122), are injected into the low energy end of the accelerator. Inside the accelerator the negative ions are accelerated to the high voltage terminal (at 3.6 MV in this study) where they are stripped of electrons in the nitrogen gas stripper canal; the positive ions produced are further accelerated through the high energy end of

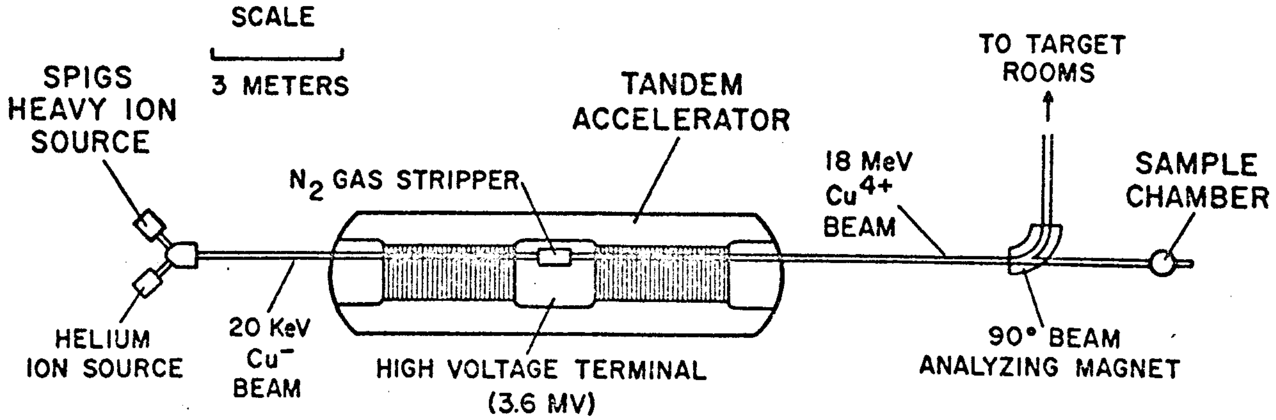

UNIVERSITY OF WISCONSIN HEAVY ION IRRADIATION FACILITY

FIGURE 6. Schematic of the heavy-ion irradiation facility at the University of Wisconsin-Madison. Copper ions from the SPIGS source are injected into the tandem accelerator. The resulting energetic heavy-ions, in this case 18 MeV Cu^{4+}, bombard the specimens (vanadium) located in the sample chamber. (The sample chamber is actually ¼° off the tandem axis.)

the accelerator to a final energy determined by the charge state, q, of each ion and given by

$$E_{ion} = (q + 1)V \tag{57}$$

where V is the accelerator terminal voltage. The beam exits from the accelerator and is focused and steered on to the samples in the target chamber. The undesired components of the beam are separated from the desired beam (usually Cu^{3+} or Cu^{4+}) by the focal properties of the quadrupole lens and a 1/4° bend in passing through the 90° analyzing magnet (which is not capable of bending the heavy-ion beam into existing target rooms). Analysis of the beam striking the samples is discussed below.

The target chamber of the U.W. Heavy-Ion Irradiation Facility is designed to mate with the relatively poor vacuum (5×10^{-6} Torr) of the accelerator beam line and yet provide a high vacuum environment (1×10^{-8} Torr) in the sample region to reduce the contamination of refractory metals, such as vanadium, with gaseous impurities. This high vacuum sample environment is achieved by using three differentially pumped stages (see Figure 7). The first pumping stage, which mates to the accelerator beam line, uses a 200 liter/sec diffusion pump equipped with a liquid nitrogen cold trap to maintain pressures near 2×10^{-6} Torr. The intermediate pumping stage is separated from the first stage by an anti-creep liquid nitrogen cold trap and a 9.5 mm aperture. The intermediate

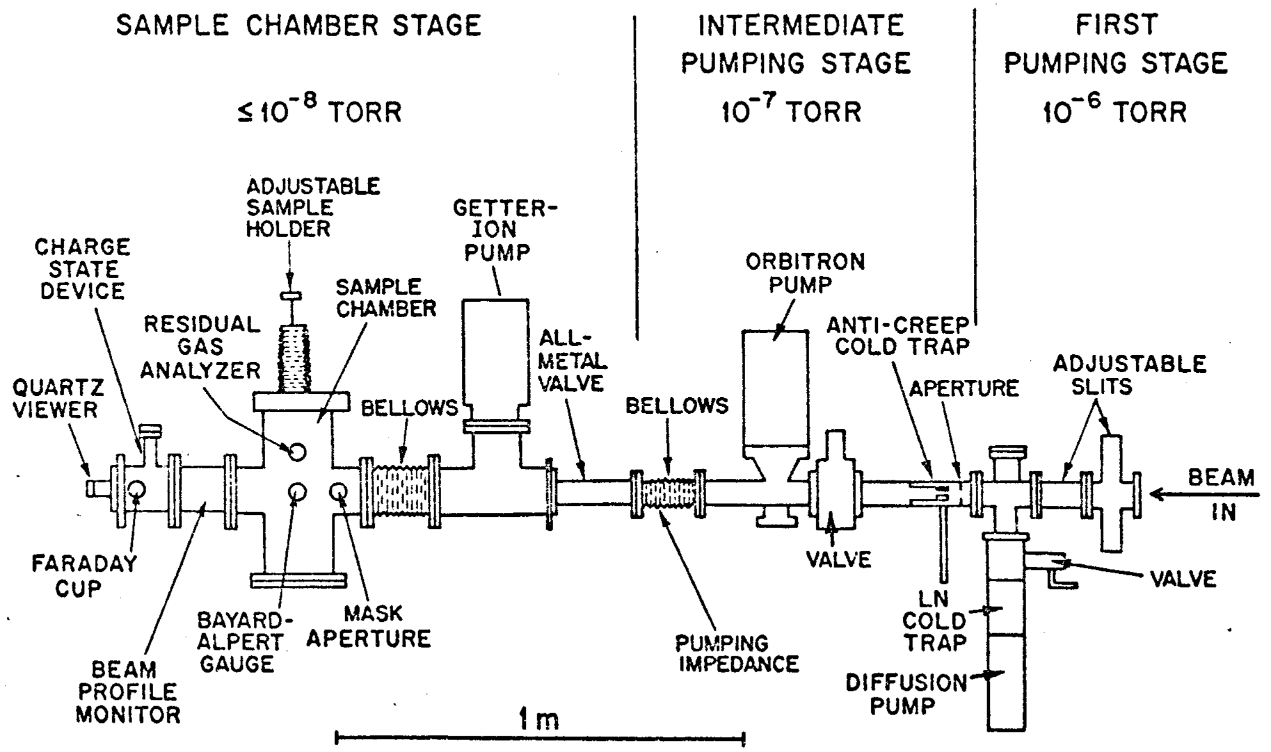

FIGURE 7. The target chamber of the University of Wisconsin Heavy-Ion Irradiation Facility.

stage is pumped by a 300 liter/sec orbitron pump(123) and maintains a pressure of about 1 x 10^{-7} Torr during an irradiation. The sample chamber region is isolated from the intermediate stage by a pumping impedance composed of fifteen 6.5 mm apertures in series which provide a very low conductance. The sample chamber is pumped by a 600 liter/sec getter-ion pump (National Electrostatics Corporation) which maintains a vacuum of less than 1 x 10^{-8} Torr during irradiations at elevated temperatures.

The high vacuum sample chamber is equipped with various diagnostic devices to characterize the vacuum environment (pressure and residual gas) and the ion beam striking the samples (energy, composition, intensity and uniformity). The relative positions of these diagnostic devices are illustrated in Figure 7.

The pressure in each of the three vacuum regions is measured independently. Ionization type gauges (RCA-1949) are employed in the first and intermediate stages; in the sample chamber a Bayard-Alpert type gauge (Westinghouse 5966) is used. A residual gas analyzer (VGA-100, Varian Associates) is used to measure the partial pressure composition of the sample chamber and also serves as a helium leak detector if the need arises. A partial pressure analysis of the sample chamber vacuum during an in situ anneal at 1050°C and subsequent irradiation at 700°C of a vanadium sample is shown in Figure 8. (Data similar to that used to derive the results of Figure 8 are shown in Figure 17 in the following section.) During

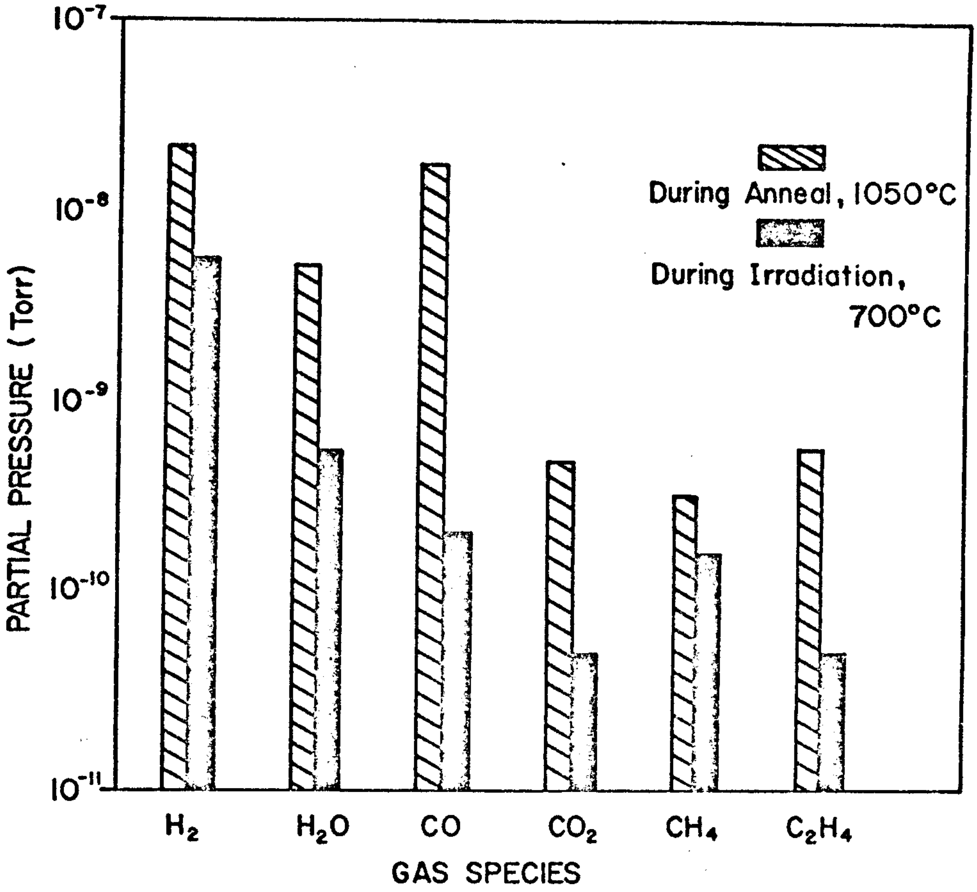

FIGURE 8. Partial pressure analysis of the residual gas in the target chamber during a high temperature anneal at 1050°C and a subsequent irradiation at 700°C.

a high temperature anneal in the tandem target chamber H_2 and CO are the main constituents of the residual gas; however, at lower temperatures H_2 is the major component of the residual gas.

The energy, composition, intensity, and uniformity of the ion beam striking the sample are measured so that the damage state of each sample may be determined. Figure 9 illustrates the positions of the diagnostic apparatus, relative to the heater and sample positions, used to characterize the beam. The energy and composition of the beam is measured by recording, in a solid state detector, the energies of ions scattered through 90° by a thin gold foil. A typical spectrum obtained for a Cu beam is shown in Figure 10a; the analysis of that spectrum (accounting for the mass and energy dependence of the laboratory Rutherford cross section) is given in Figure 10b. The beam striking the samples is almost entirely composed of Cu^{4+} (95.1% for this spectrum) with small amounts of Cu^{2+} (4.8%) and Cu^{1+} (0.06%). No nitrogen components of the beam have been detected. The uniformity and sample intensity are determined by the beam scanner, movable slits (see Figure 7), Faraday cups (the mask aperture also has a Faraday cup position), and the ability to monitor beam current striking the samples (the samples, heater and heat shield are electrically connected to form a Faraday cup).

The samples are heated by a 4 cm diameter, cylindrical, thermal radiation furnace. The furnace is constructed of 0.025 mm tantalum sheet and is surrounded by a fifteen layer, spirally wound

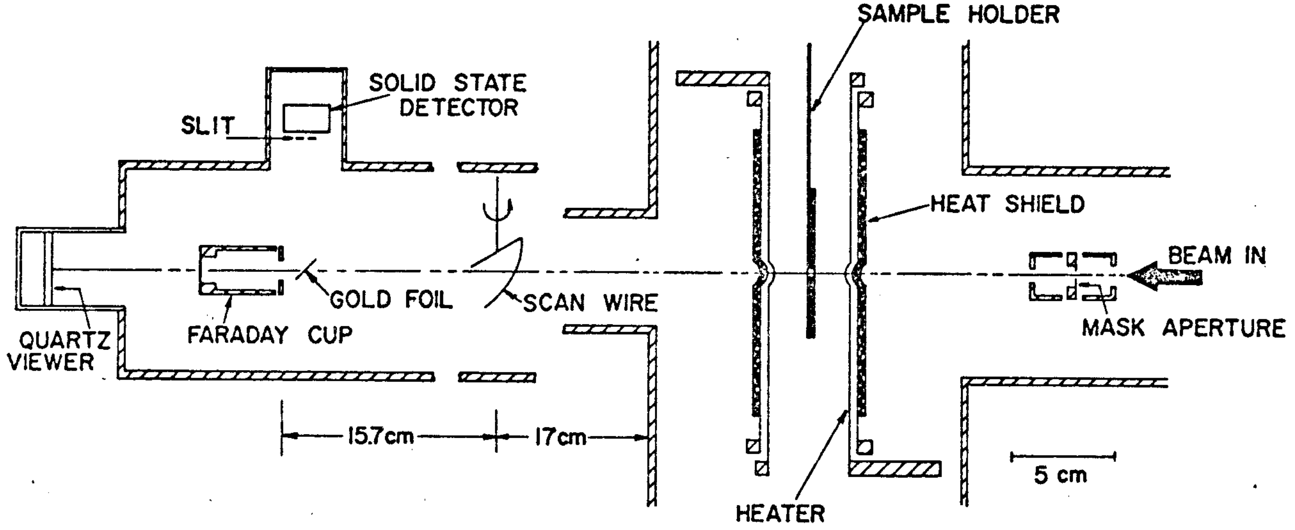

FIGURE 9. Detailed schematic of the sample chamber showing ion beam diagnostic devices, heater, heat schield, and sample holder.

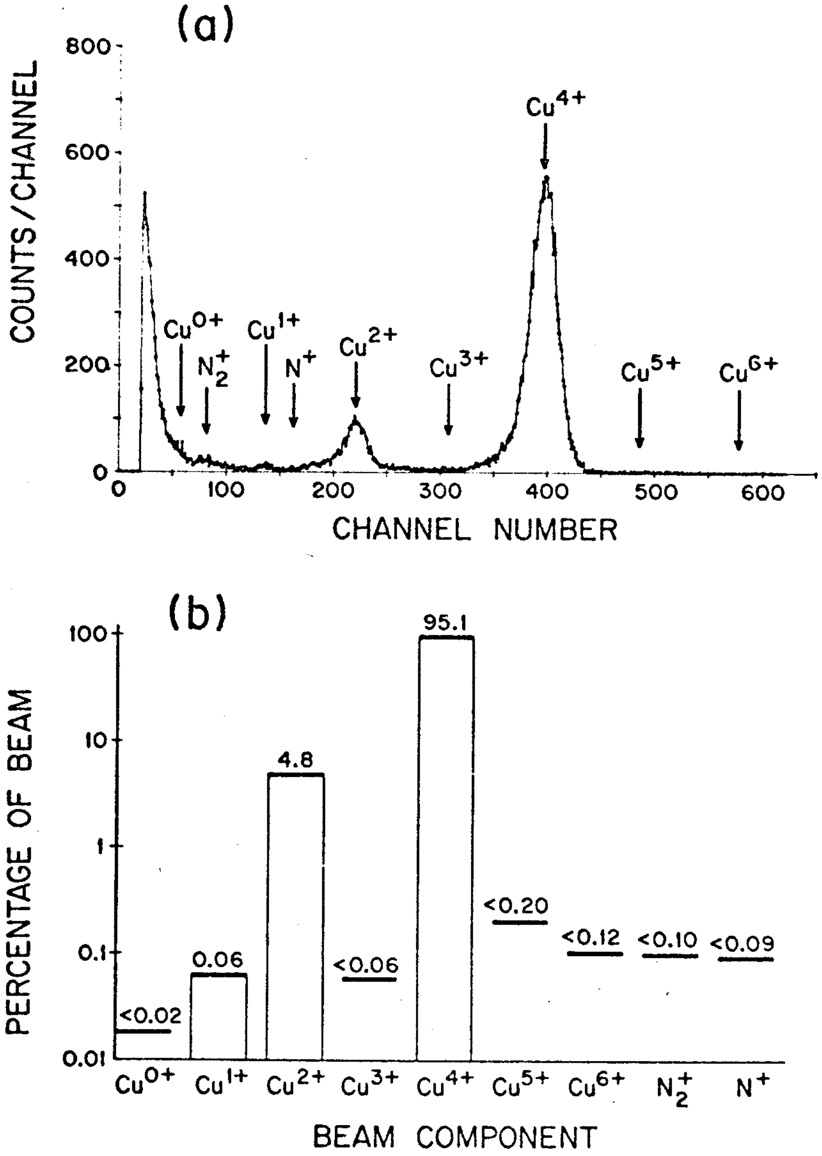

FIGURE 10. (a) A typical energy spectrum for a Cu ion beam as recorded in the solid state detector. (b) The composition as determined from the above spectrum.

heat shield, also constructed of 0.025 mm tantalum sheet. The ion beam is transmitted through 1 cm holes in the furnace and heat shield for sample irradiation or beam analysis. The furnace, heat shield, and sample holder are shown schematically in Figure 11. This furnace has operated successfully providing sample temperatures that range from 150 to 1050°C. The power requirement of the furnace for a sample at 1000°C is about 400 watts.

The samples are mounted in a tantalum holder which is suspended from an adjustable bellows seal along the axis of the heater (see Figure 7). The adjustable bellows allows vertical motion of the samples, thus permitting the irradiation of more than one sample or area. Initially the sample holder was designed to accomodate foil strips, 7 cm x 1.25 cm, as illustrated in Figure 12. There were six sample positions, interspaced with five holes for beam alignment and analysis. Two chromel-alumel thermocouples were used to measure temperature. The foil strips proved to be inconvenient when preparing electron microscopy specimens (3 mm discs), and the two chromel-alumel thermocouples were insufficient for accurate temperature measurement along the entire length of the sample holder. In order to overcome these difficulties, a new holder was constructed of tantalum to accomodate eight 3 mm disc samples. This sample holder is shown in Figure 13 and is schematically illustrated in Figure 14a; a partial schematic of the new sample holder, shown in Figure 14b, illustrates in detail the positions of the chromel-alumel

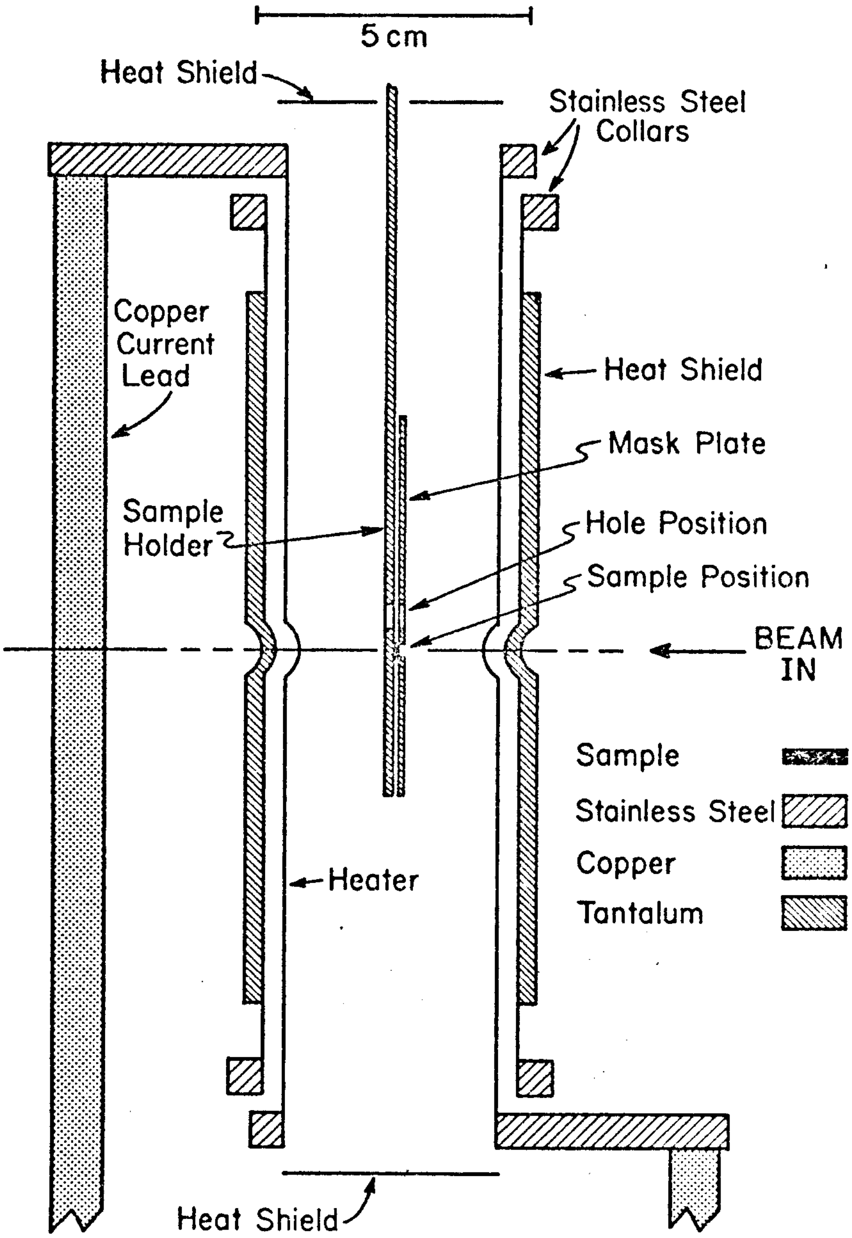

FIGURE 11. Schematic of the radiation heater assembly in the sample chamber.

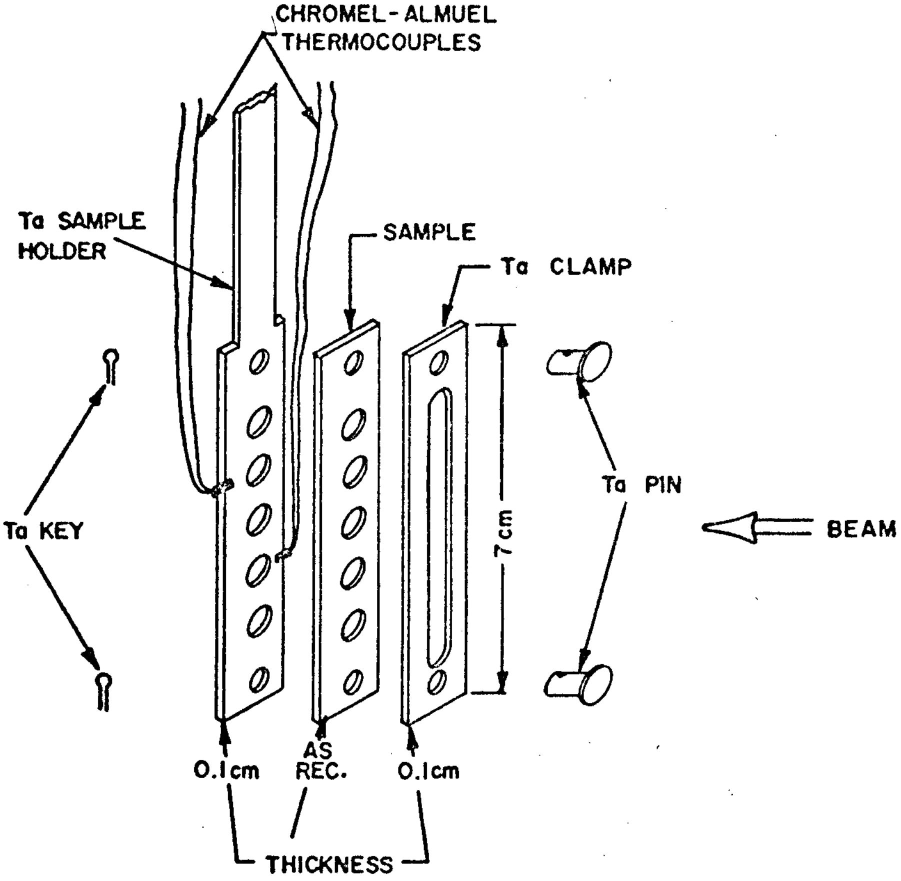

FIGURE 12. Sample holder for irradiating foil strips.

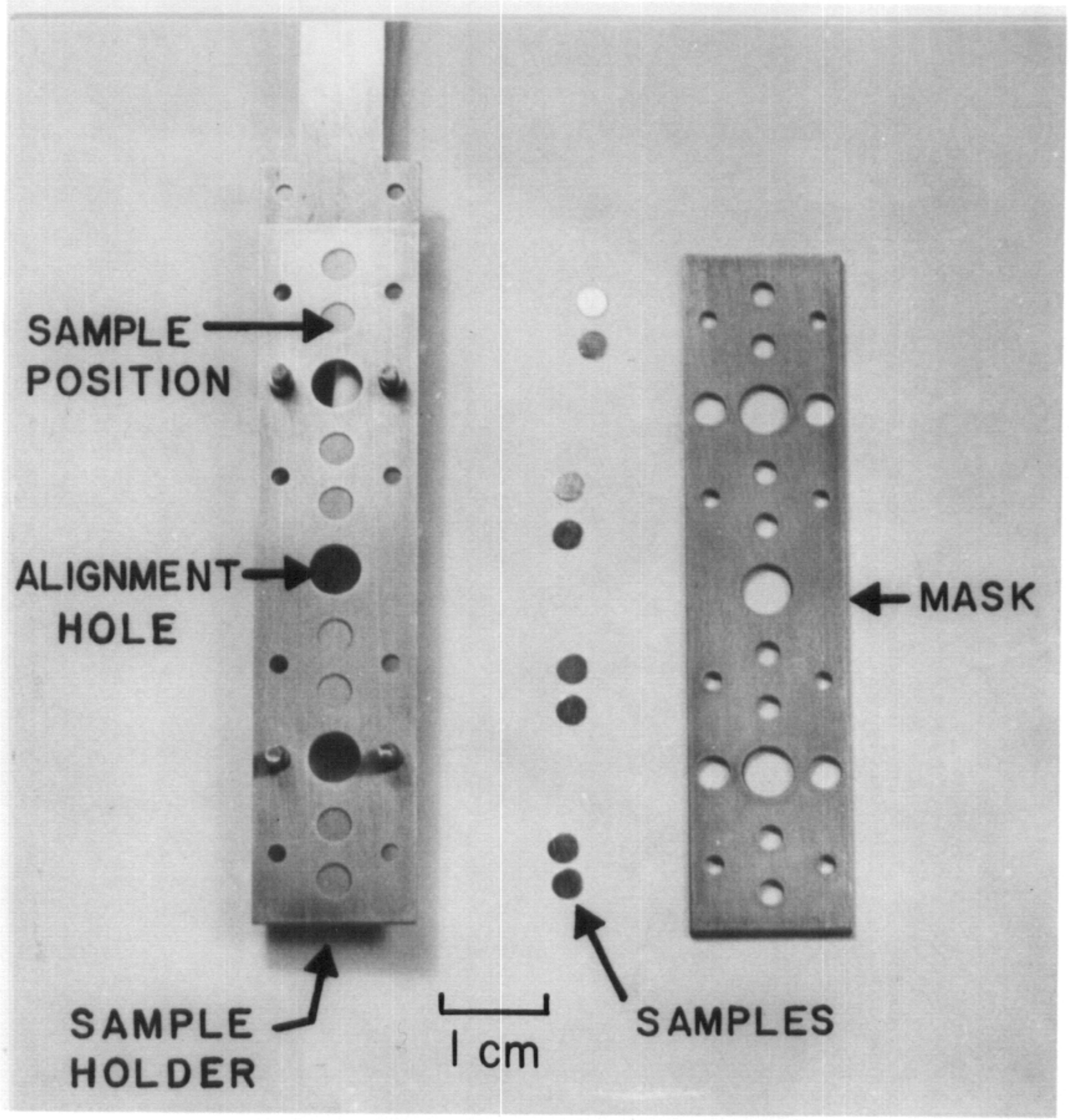

FIGURE 13. Sample holder for irradiating 3 mm discs.

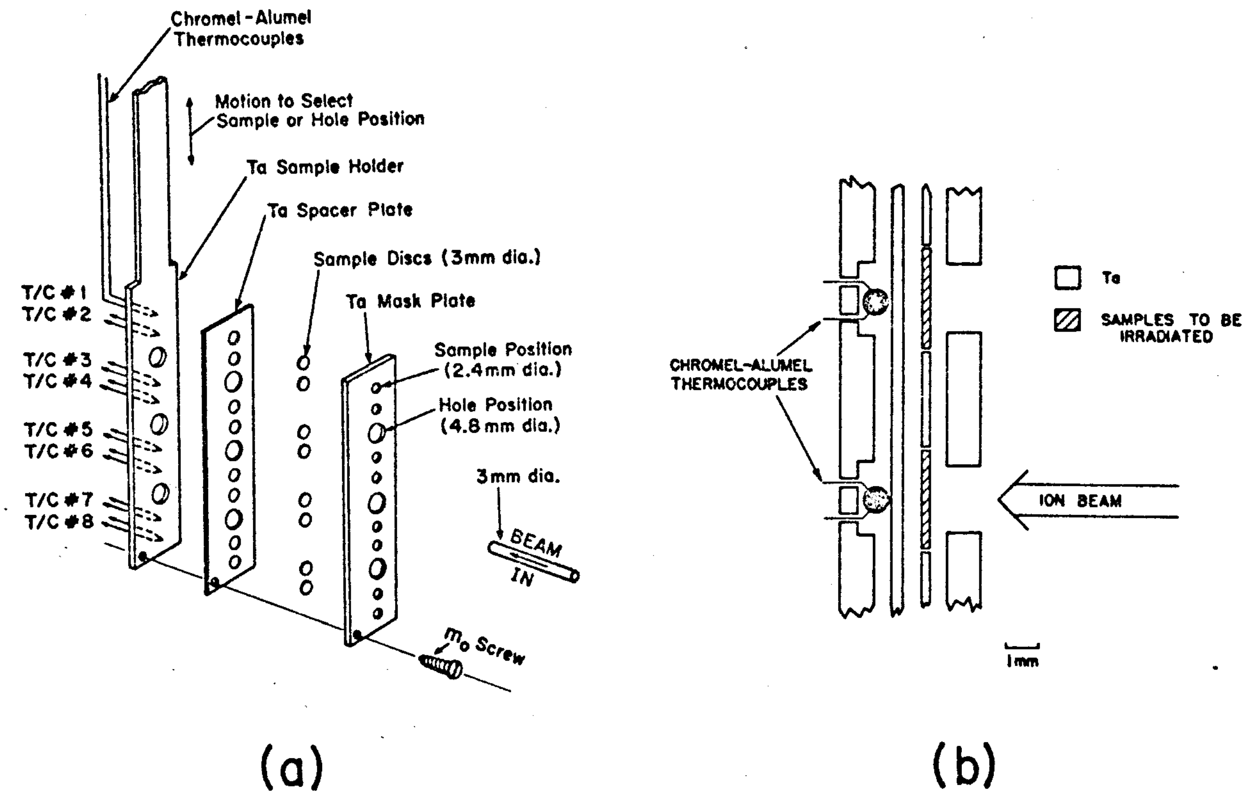

FIGURE 14. (a) Schematic of the sample holder for irradiating 3 mm discs. (b) Detailed schematic of the same holder showing the positions of the thermocouples relative to the 3 mm disc samples.

thermocouples (one per sample) and the samples in the sandwiched holder. With this sample holder design, three holes are available for optical alignment of the holder with respect to the beam axis and for transmission of the ion beam for analysis.

High Vacuum Annealing System

Initially, vanadium samples to be irradiated were annealed *in situ* (i.e., in the target chamber) to reduce the amount of contamination from handling. The results of a first series of irradiations(124) (to be discussed in Chapter VI) indicated that contamination was occurring during the high temperature annealing of vanadium in the tandem target chamber just described. In an effort to eliminate this contamination, a high temperature annealing furnace was constructed within an ultra-high vacuum, all metal bell jar (Model TNB-X, from Perkin-Elmer Ultek, Inc.).

The chamber of the metal bell jar is pumped by a 200 liter/sec Differential-Ion pump and a titanium sublimator (both are integral parts of the TNB-X vacuum system) which maintain a vacuum of 1×10^{-10} Torr at ambient temperatures. An 8 inch Poppet Valve is used to isolate the pump and sublimator from the bell jar chamber during sample loading, sample removal, or routine maintenance. A two stage, oil-less roughing system is used, thus eliminating the usual back streaming of mechanical pump oil. The first stage consists of a oil-less mechanical pump (Bell and Gossett) to reach a pressure of about 200 Torr. The second stage is an

Ultek sorption pump which will pump the chamber to about 10^{-3} Torr, a point at which the D-I (Differential- Ion) pump may be opened to the chamber (or started if it has been shut off and let up to air). The pressure in the chamber is measured with a Bayard-Alpert type gauge (Model 971-5005, Varian Associates). A residual gas analyzer (VGA-100, Varian Associates) is mounted on this vacuum system and allows a gas analysis during the annealing of the samples. A variable leak valve (Series 203, Granville-Phillips Co.) with a continuously variable conductance from 0.4 to 10^{-11} liter/sec (10^{-13} liter/sec when closed) is used to leak small quantities of known gas into the vacuum chamber to calibrate the residual gas analyzer (the RGA on the tandem target chamber was also calibrated on this vacuum system).

The samples to be annealed are placed on the sample holder shown in Figure 15. The support rods of the holder are made of tungsten, a tantalum mesh is used to support the samples, and the temperature is measured with two chromel-alumel thermocouples. The samples are annealed by electron bombardment in the furnace shown in Figure 16. To reach 1050°C a bias voltage of 660 volts and a filament emission current of 180 mA are normally required. The four tungsten filaments (.008 inch diameter) are heated by a current of 4.65 Amperes each (18.6 Amperes total).

During a typical anneal, the vanadium samples are heated to 1050 °C while maintaining a vacuum of 1×10^{-8} Torr. A

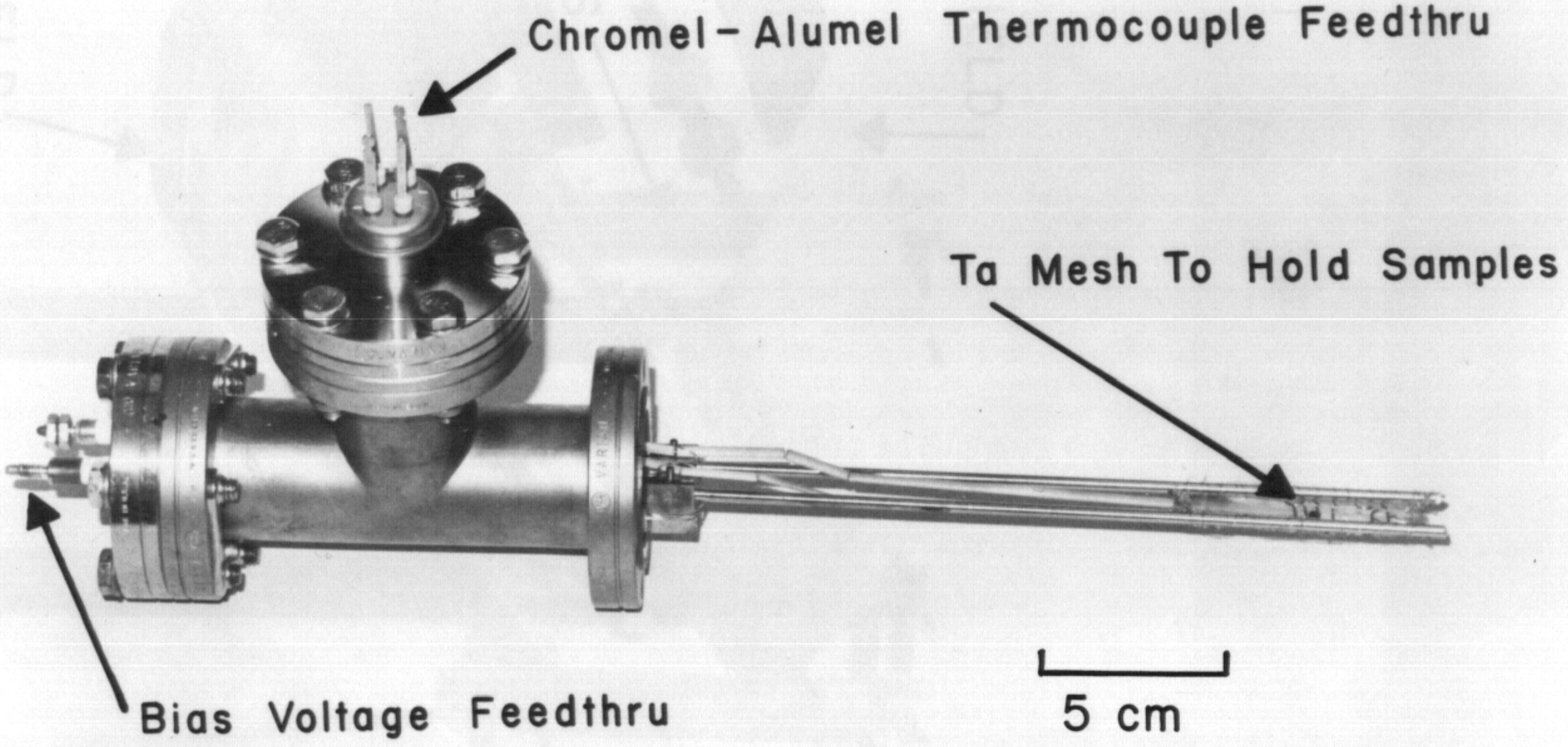

FIGURE 15. Sample holder for the high vacuum annealing furnace.

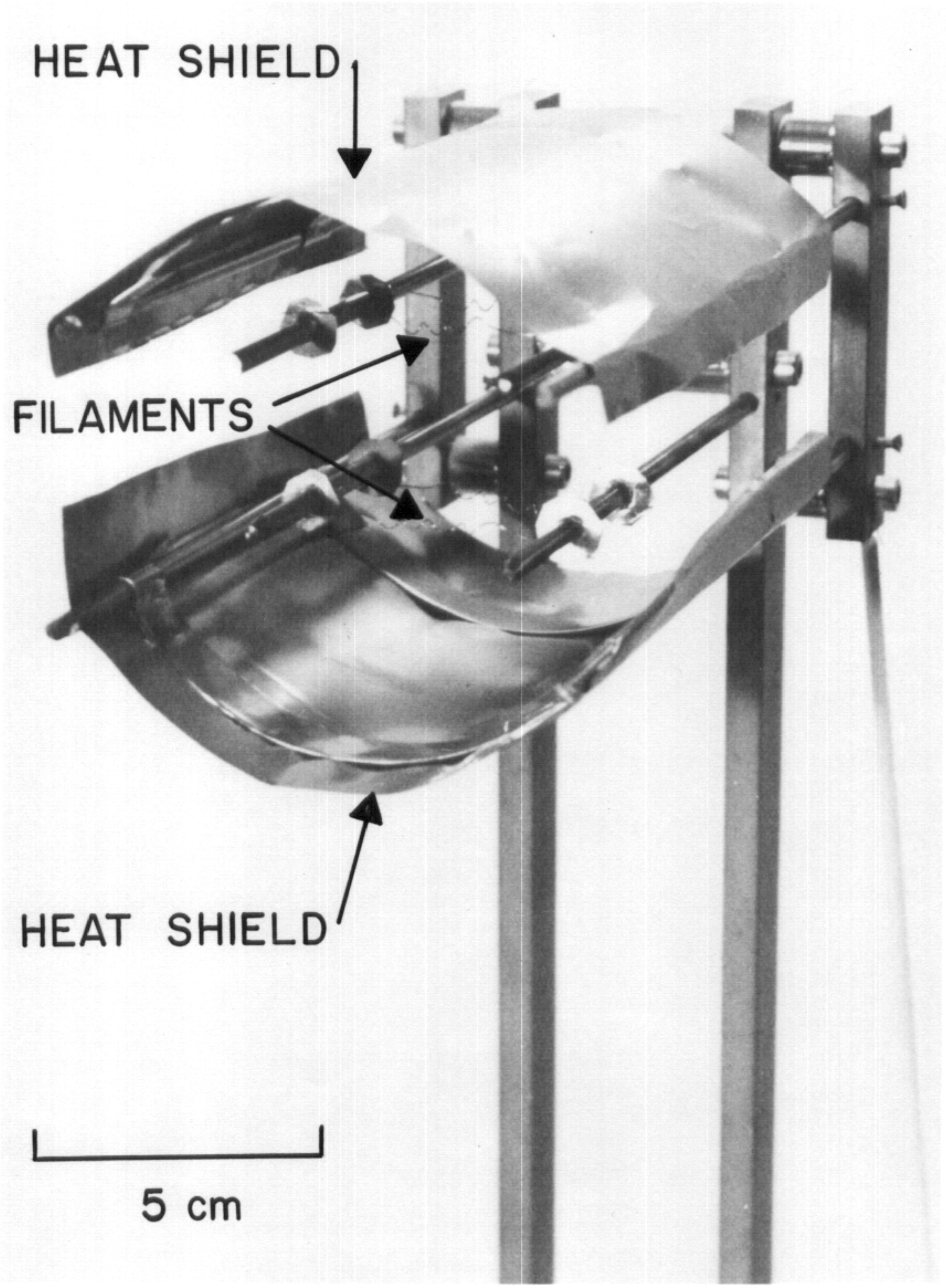

FIGURE 16. High vacuum annealing furnace.

0-50 amu RGA scan during an anneal is shown in Figure 17 (the sensitivity may be increased by an order of magnitude if needed). After properly accounting for the cracking patterns of the various gases and the sensitivity of the RGA for different gases, the interpretation of this scan is shown in Figure 18 and compared to a similar anneal in the tandem target chamber. As can be seen, the partial pressures of the residual gases during an anneal in the new high vacuum furnace are only a factor of 2 to 5 lower than those during an anneal in the tandem target chamber.

The major advantage of this new annealing environment over the environment of the tandem target chamber are:

1. Reduced pumping impedance around the samples.
2. More use of refractory metals.
3. Time to reach the annealing temperature (1050°C) is reduced from 96 hours to about 15 minutes.

This topic of annealing environments will be discussed further in Chapter VII.

Material Characterization

The high purity vanadium used in this study was obtained in sheet form from Dr. R.E. Reed of the Oak Ridge National Laboratory. The substitutional impurity content of the vanadium is less than 10 wt-ppm and the interstitial impurity content of the material is less than 200 wt-ppm. The analysis of this material by Oak

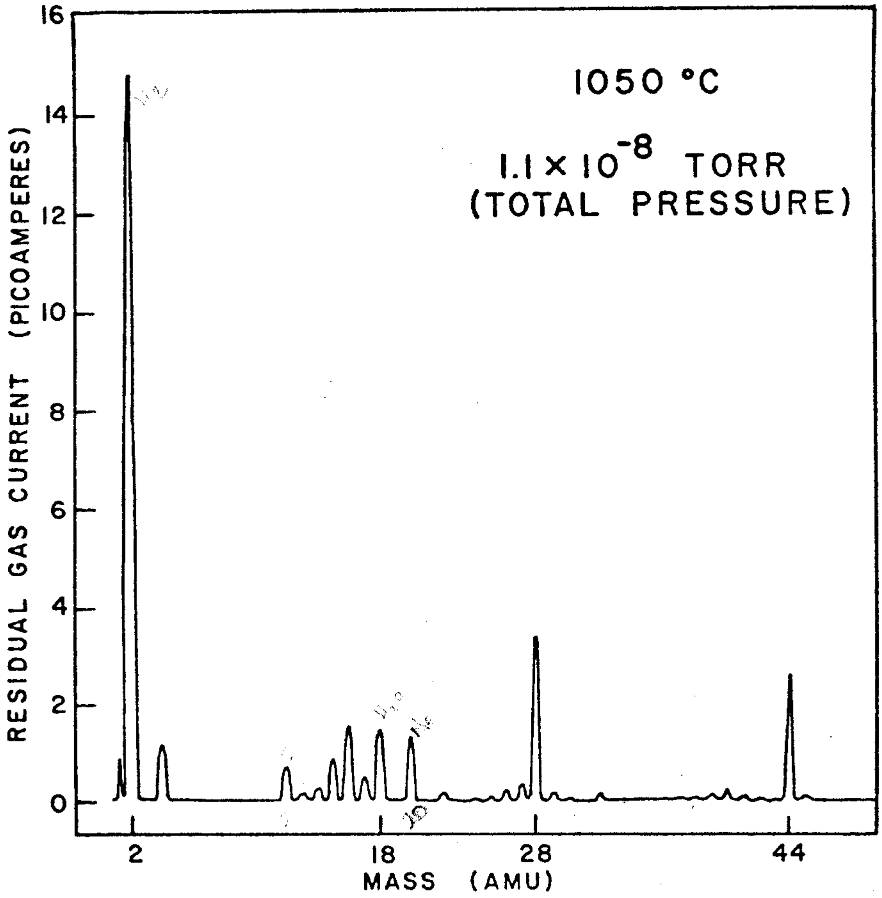

FIGURE 17. A residual gas scan (0 to 50 amu) during an anneal in the high vacuum annealing furnace.

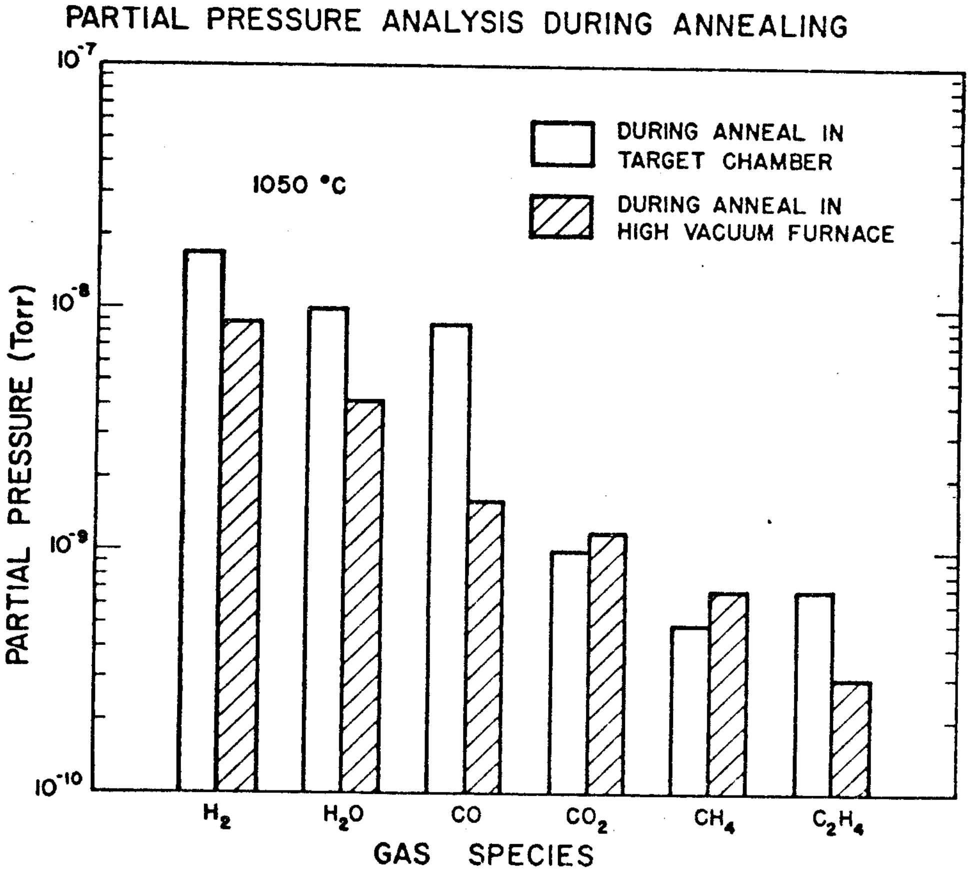

FIGURE 18. A comparison of the residual gases during annealing in the target chamber with the residual gas during annealing in the high vacuum furnace. (High vacuum furnace data from Figure 17.)

Ridge is given in Table 4. The bulk carbon content of this material was independently measured by the McDonnell-Douglas Corp. and found to be approximately 20 wt-ppm(125). Another analysis by the Grumman Aerospace Corp. (to be discussed in more detail in Chapter VI) found the carbon content to be about 20 wt-ppm, the oxygen content to be about 100 wt-ppm, and the nitrogen content to be less than 90 wt-ppm(126). These results agree fairly well with the Oak Ridge analysis within the limits of experimental error.

Sample Preparation

The procedures for the preparation of samples for irradiation and for transmission electron microscopy (TEM) will now be described. In many instances procedures changed as new techniques, sample geometry, or new vacuum systems were employed. In these cases, both old and new procedures will be described.

The shape of the samples was determined by the holder used for the irradiations. Specially machined strips of the vanadium sheet were prepared for the irradiations which used the sample holder shown in Figure 12 (from 9/74 to 11/75). The 3 mm disc samples for use in the holder of Figures 13 and 14 (from 5/76 to 4/77) were punched from the vanadium sheet. The sample strips and 3 mm discs were flattened between steel blocks, electropolished in a 20% H_2SO_4 and 80% methanol solution at -20°C (to remove any surface contamination and provide the polished surface necessary for TEM work), and washed in absolute methanol prior to annealing.

TABLE 4

CHEMICAL ANALYSIS OF THE VANADIUM USED IN THIS STUDY

Impurity	Content (wt-ppm)
C	50
O	48
N	71
H	3
Ta	0.2
W	1.8
Al	0.05
Fe	3
Si	3
Ti	0.1
Co, Cr, Cu. Ni	Not detected

The foil strips were annealed in the tandem target chamber for 1 hour at 1050°C. It took about 4 days to reach the annealing temperature as the heater assembly slowly degassed. The 3 mm disc samples were annealed in the high vacuum annealing furnace for 1 hour at 1050°C. It only took about 15 minutes to reach 1050°C in this system. A comparison of the residual gases in the two systems during annealing has already been given in Figure 18. The preirradiated grain structure of an annealed vanadium sample is shown in Figure 19. This sample was etched in a solution of 50% HNO_3 and 50% H_2O (distilled) for 15 seconds at room temperature. The grain structure has an ASTM Micro-Grain-Size number of 1.7(127).

The sample strips annealed in the tandem target chamber were usually irradiated with no further treatment. However, for two sets of irradiations (discussed in Chapter VI) the sample strips were removed from the target chamber after annealing and a portion of each sample strip was electropolished to remove approximately 0.025 mm from the surface to be irradiated. The samples were then reloaded into the target chamber for irradiation. The 3 mm discs were usually loaded into the target chamber after annealing with no further treatment; again, however, several discs were given an additional electropolish before irradiation.

The samples were irradiated with 14 or 18 MeV Cu ions depending on which charge state (+3 or +4) was used (a few samples were irradiated with O, Nb, and Ni). The ion flux striking the

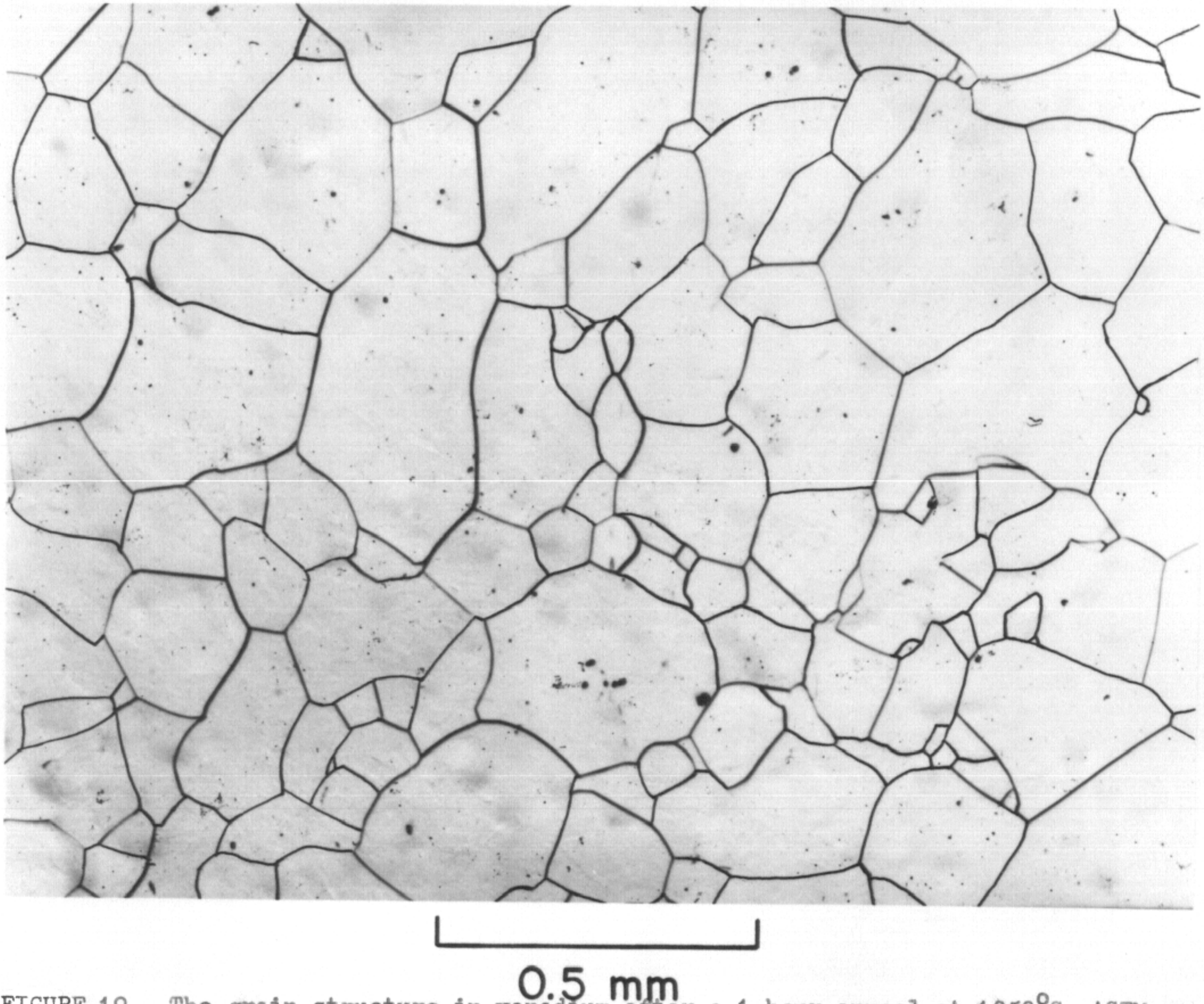

FIGURE 19. The grain structure in vanadium after a 1 hour anneal at 1050°C, ASTM grain size 1.7.

samples ranged from 6×10^{11} to 1.2×10^{12} ions/cm^2-sec. This corresponds to a damage rate of about 1 to 2×10^{-4} dpa/sec at a depth of 1 micron, where the TEM analysis is done (see Figure 20). The damage levels usually attained (at 1 micron) were 1.0 to 2.0 dpa. The temperature of the irradiations spanned the range from 150°C (0.19 T_m) to 850°C (0.52 T_m). The pressure during the irradiations ranged from 2×10^{-9} Torr (at lower temperatures) to 7×10^{-9} Torr (at higher temperatures). The residual gas analysis during an irradiation at 700°C has already been given in Figure 8. The amount of CO, CO_2, CH_4, C_2H_4 increases with temperature, but is significantly reduced at temperatures below 700°C.

The damage as a function of depth for 14 MeV copper ions incident on vanadium has already been shown in Figure 4 of Chapter II. Figure 20 is a similar curve for 18 MeV copper ions incident on vanadium, and illustrates the region where TEM analysis of the samples is done. This region is sufficiently removed from the surface, peak damage, and end of range of the copper ions; in this way the effect of the surface, the damage gradient, and the copper ions may be neglected. To expose the damage at the desired depth, the outer area of an irradiated foil is lacquered with "Microstop" (Michigan Chrome and Chemical Company) and the exposed inner area is electropolished at -25°C in a 20% H_2SO_4 and 80% methyl alcohol solution for 45 seconds. The amount of material removed was measured using an interference microscope. A white light was used to

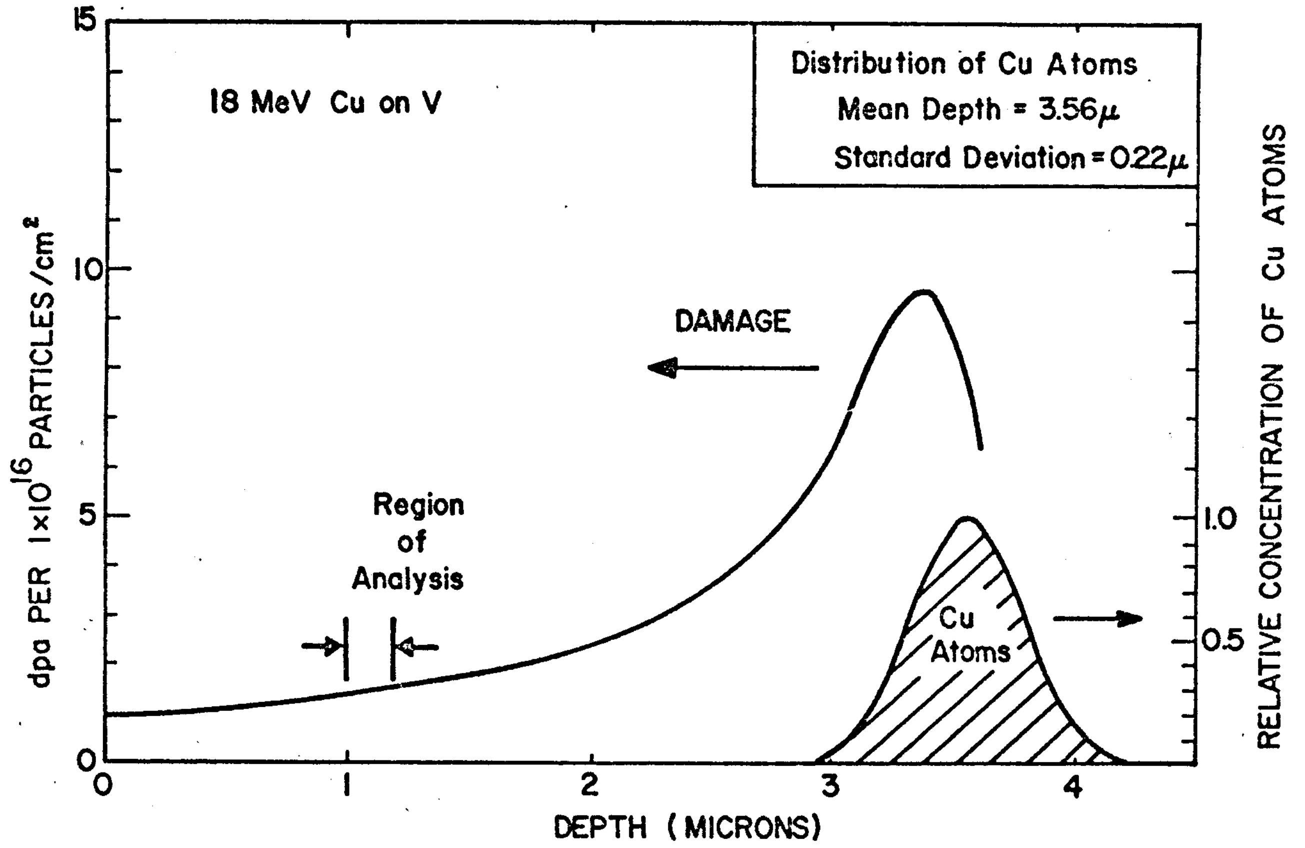

FIGURE 20. Depth distribution of damage and copper atoms in vanadium irradiated with 18 MeV copper ions, calculated using the E-DEP-1 code of Manning and Mueller(37,38) (E_d = 43 eV). Also shown is the region where all TEM analysis is done.

determine the integral number of fringes and an orange filter (λ = 5860 Å) was used to obtain better resolution and the fractional fringe shift. A typical step height measurement on an irradiated 3 mm disc is shown in Figure 21. The displacement of 3.5 fringes corresponds to a depth of 1.0 microns.

After the surface layer was removed and several step height measurements made, the samples were prepared for TEM analysis. It was necessary to cut a 3 mm disc from the samples irradiated in the form of foil strips; the samples irradiated as 3 mm discs already had the proper geometry. The disc surface with the exposed damage region was lacquered with "Microstop" to prevent electro-chemical attack. The specimens were thinned for TEM analysis by jet-polishing the unlacquered rear surface with a single-jet electropolisher (modified from Model 110 Twin-Jet Electropolisher, E.A. Fischione Instrument Mfg.) using a 20% H_2SO_4 and 80% methyl alcohol solution at -25°C. This tecnhique produced large regions (approximately 10^4 square microns) transparent to electrons.

Transmission Electron Microscopy (TEM)

The samples were examined in a JEOL 100B electron microscope which has been upgraded to operate at 120 kV. The TEM analysis of each foil generally included the investigation, in at least three different areas (three different grains if possible), of the irradiation produced microstructure in areas remote from

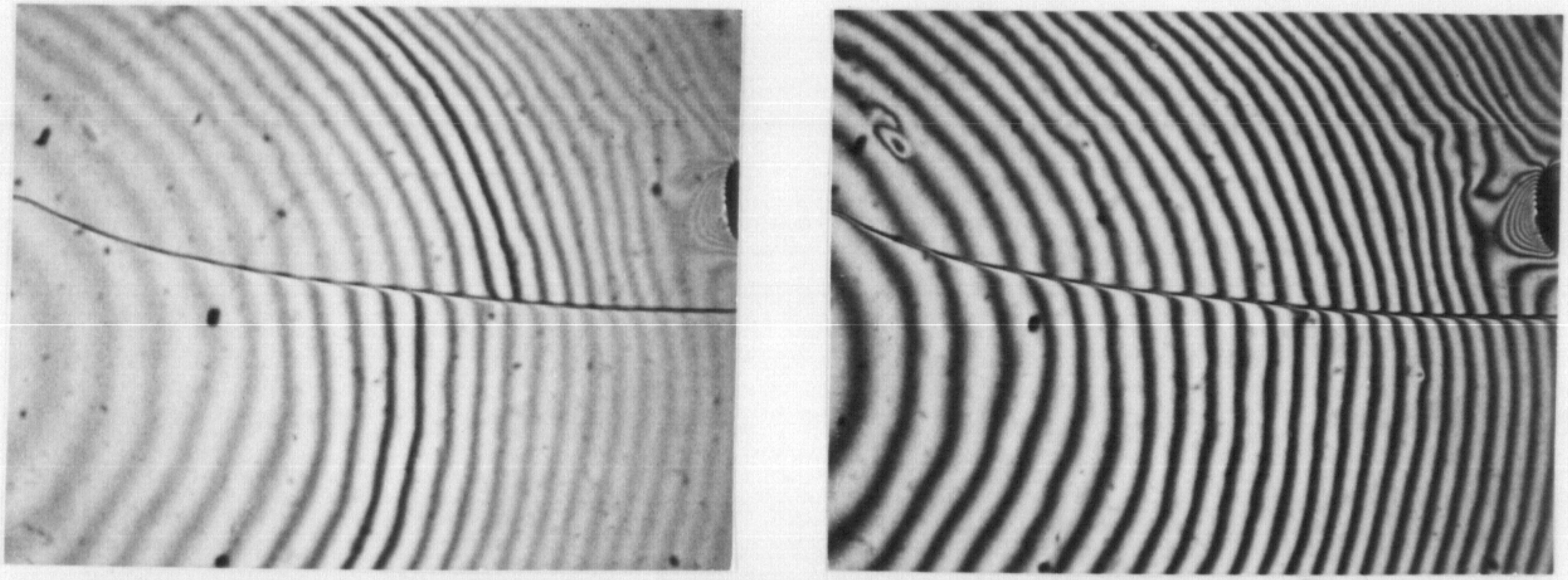

WHITE LIGHT

$\lambda = 5860$ Å

FIGURE 21. Step height measurement of the amount of surface removed from an irradiated sample. On this sample the amount removed produces a shift of 3.5 fringes which corresponds to a depth of 1 micron.

grain boundaries. In each area, stereo-micrographs of the microstructure were taken to determine foil thickness. The void microstructure was generally imaged in bright-field under absorption contrast and underfocussed conditions. The void images produced under such conditions are in maximum contrast with a bright central region surrounded by a weak (Fresnel-like) dark fringe. The dislocation structure in the same area was imaged under two-beam diffracting conditions. In a number of samples, the microstructure in the vicinity of grain boundaries was also investigated.

The foil thickness was determined in each area investigated by measuring the parallax between the two foil surfaces in a pair of stereo-micrographs. The parallax was measured with a Hilger-Watts Stereo Viewer. The foil thickness, t, is related to the parallax, p, by the equation

$$t = \frac{P}{2M \sin (\phi/2)} \tag{58}$$

where ϕ is the tilt angle and M is the magnification. (Equation 58 is only correct for symmetrical tilt about 0^o.) Foil surfaces were generally identified by pits, voids, or micro-dust on the surface.

The internal voids (voids which intersected the surface were not counted) in an area of known thickness were counted with a Zeiss TGZ3 particle-size analyzer (48 size classes). The variable spot size of the analyzer was superimposed over the image of each void, approximating the diameter of multi-faceted (or small) voids and the cube edge of the large cubic voids. The voids in each size class were corrected for the number of voids that intersected the surface by the expression(128,129):

$$n_i = \frac{n_i(\text{observed})}{1 - d_i/t} \quad (59)$$

where d_i is the mean diameter of size class i and t is the foil thickness.

The average void size (diameter or cube edge) is defined as

$$\bar{d} = \frac{\sum n_i d_i}{N_T} \quad (60)$$

where

$$N_T = \sum n_i \quad (61)$$

The standard deviation in void size is given by(129):

$$\sigma = \left\{ \frac{\sum n_i \, (d_i - \bar{d})^2}{N_T} \right\}^{1/2} \quad . \quad (62)$$

In determining the void volume fraction, it is preferable to use the volume averaged void size(129) given by:

$$\bar{D} = \left[\frac{\sum n_i d_i^3}{N_T}\right]^{1/3} \qquad (63)$$

The void number density, ρ_V, was calculated from the total number of voids, the foil thickness, and the foil area, i.e.,

$$\rho_V = N_T/At \qquad (64)$$

where A is the foil area. The void volume fraction is then given by the general expression

$$\Delta V/V = \alpha D^3 \rho_V \qquad (65)$$

where α is a factor that is dependent on void shape. For spherical voids

$$\alpha = \pi/6 \text{ (spherical)} \qquad (66)$$

and $\bar{D}$ is the volume averaged diameter; in the case of cubic voids

$$\alpha = 1 \quad \text{(cubic)} \qquad (67)$$

and $\bar{D}$ is the volume averaged cube edge. For vanadium α ranges from 0.75 (due to truncation) to 1.0 at the higher temperatures (above 500°C) and approaches $\pi/6$ at temperatures below about 500°C.

The dislocation density in the foil was determined by conventional methods(130). The dislocation loop density was calculated from the total number of loops (corrected for invisible loops) in the foil divided by the foil volume (A x t). The loops were also counted with the Zeiss TGZ3 particle-size analyzer and the average loop diameter determined. The nature of the loops (interstitial or vacancy) was more difficult to determine and the methods to do so will now be discussed.

Loops smaller than about 100 Å are generally only observable as "black dots" when imaged under kinematical conditions; however, loops of the same size lying close to a foil surface will exhibit black-white contrast when imaged under dynamical conditions. If a vector, $\underline{l}$, is defined in the sense of the black-white image, then the sign of $\underline{g} \cdot \underline{l}$ and the distance of the loop from the top or bottom surface will determine the nature of the loop(130). The Burgers vector of these loops is more difficult to determine, analysis requires the matching of experimental images under specific conditions with computer simulated images(131,132).

Loops with diameters from about 50 Å to 200 Å may be analyzed by the methods for large resolvable loops (>200 Å) if weak beam images are used(130,133). This is due to the decrease in extinction distance which enable smaller loops to be clearly resolved as loops rather than as black dots. This increase in resolution is very dependent on image stability since very long exposure times (on the order of 10 to 30 min) are required. Thus beam instability or image drift can negate the increased resolution at high magnifications.

Large resolvable loops (diameters >200 Å) are analyzed on the basis of theoretical image calculations for straight dislocations in an elastically isotropic medium based on the kinematical and dynamical theories of electron diffraction(134,135,136). The most important result of these calculations is that the dislocation image (intensity minimum) is displaced from the actual position of the dislocation by the local curvature of the reflecting planes. The image will lie to that side of the dislocation core where the lattice rotations introduced by the defect tend to minimize the deviation from the Bragg angle. Several methods(147,138,139,140) employing these theoretical results were developed for analyzing large edge dislocation loops; however, the methods were not always applicable to non-edge loops. A thorough treatment of the problems involved in the characterization of large loops (edge and non-edge) has been presented by Maher and Eyre(141). The technique of Maher and Eyre(141) was used in the analysis of loops in this study and a description of the technique follows. (This technique is also fully described in Loretto and Smallman(130)).

In order to analyze the nature of dislocation loops, it is necessary to adopt a convention for defining the Burgers vector of a loop. The convention normally used(130,141), and the one which will be adopted here, is to define the Burgers vector by taking the positive direction around the loop as clockwise when viewed from above the crystal and then apply the FS/RH perfect crystal convention of Bilby, Bullough, and Smith(142). (In the FS/RH convention a circuit starting at S is made around the dislocation line in a right-handed sense and this circuit is closed at F so that in the imperfect crystal F and S superimpose; the corresponding circuit is made in a perfect crystal and the closure failure in the sense of FS is taken as $\underline{b}$(130).) This procedure for determining the Burgers vector of a loop is illustrated in Figure 22 for a vacancy loop and an interstitial loop. The important consequence of this convention is that for interstitial loops $\underline{n} \cdot \underline{b} > 0$ and for vacancy loops $\underline{n} \cdot \underline{b} < 0$(136) ($\underline{n}$ is the upward drawn normal to the loop plane). Thus, if $\underline{n}$ and $\underline{b}$ can be determined, the nature of the loop is known.

The determination of the Burgers vector (± b) is based on the standard result for dislocations that the loop is invisible or exhibits residual contrast when $\underline{g} \cdot \underline{b} = 0$(130). This technique results in the direction of ±b but does not determine the sign of the Burgers vector. The sign (or sense) of the Burgers vector can be determined by the result, already mentioned, that the loop image lies to that side of the dislocation core where the lattice rotations introduced by the loop tend to minimize the deviation from the Bragg angle. When viewed from above (same convention as used to define $\underline{b}$), these image shifts can be described by the following inequalities:

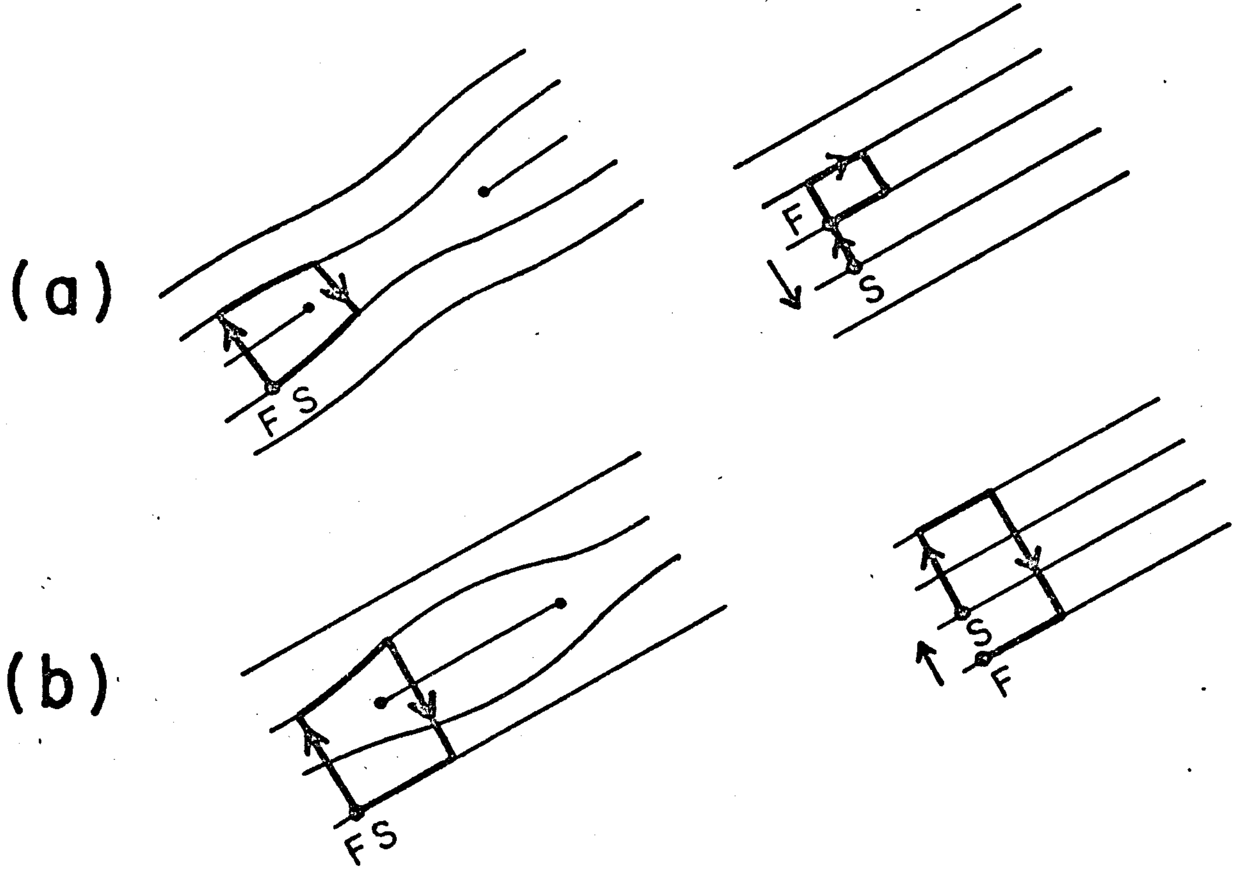

FIGURE 22. Illustration of the FS/RH convention for defining b and (a) a vacancy and (b) an interstitial dislocation loop (after Loretto and Smallman(130)).

$$(\underline{g} \cdot \underline{b})s_g > 0, \text{ outside contrast} \tag{68}$$

$$(\underline{g} \cdot \underline{b})s_g < 0, \text{ inside contrast.} \tag{69}$$

Once the sense of $\underline{b}$ is known, the nature of edge loops is easily determined since $\underline{b}$ is parallel to $\underline{n}$. (Proper indexing of $\underline{g}$ is critical.) The situation for non-edge loops must be considered more carefully.

In the case of non-edge loops, the sense of $\underline{b}$ is insufficient to determine the nature of the loop unless the relative orientation of $\underline{n}$ with respect to $\underline{b}$ is known. Maher and Eyre(141, 143) have considered the problem of non-edge loops and have described a set of conditions whereby the nature of a non-edge loop is determined by the sense of $\underline{b}$ alone (as in the case for edge loops). These conditions require that all possible loop normals for a given Burgers vector lie within a "safe orientation". The safe orientations of $\underline{n}$ (for a given $\underline{b}$) are bounded, on a stereographic projection, by $\underline{n}_j \cdot \underline{b} = 0$ and $\underline{n}_j \cdot \underline{z} = 0$ where z is the beam direction.

In the case of vanadium, $\underline{n}$ is of the $\langle 110 \rangle$ type and $\underline{b}$ is of the a/2 $\langle 111 \rangle$ type. To analyze loops in vanadium it is necessary to tilt the specimen and work near those zone axes ($\underline{z}$'s) where all possible $\underline{n}$'s are in safe orientations. This is illustrated in the [001] stereographic projection of Figure 23, where $\pm$ b = a/2 [111] has been assumed. All possible $\underline{n}$'s ($\underline{n}_1$, $\underline{n}_2$ and $\underline{n}_3$) are

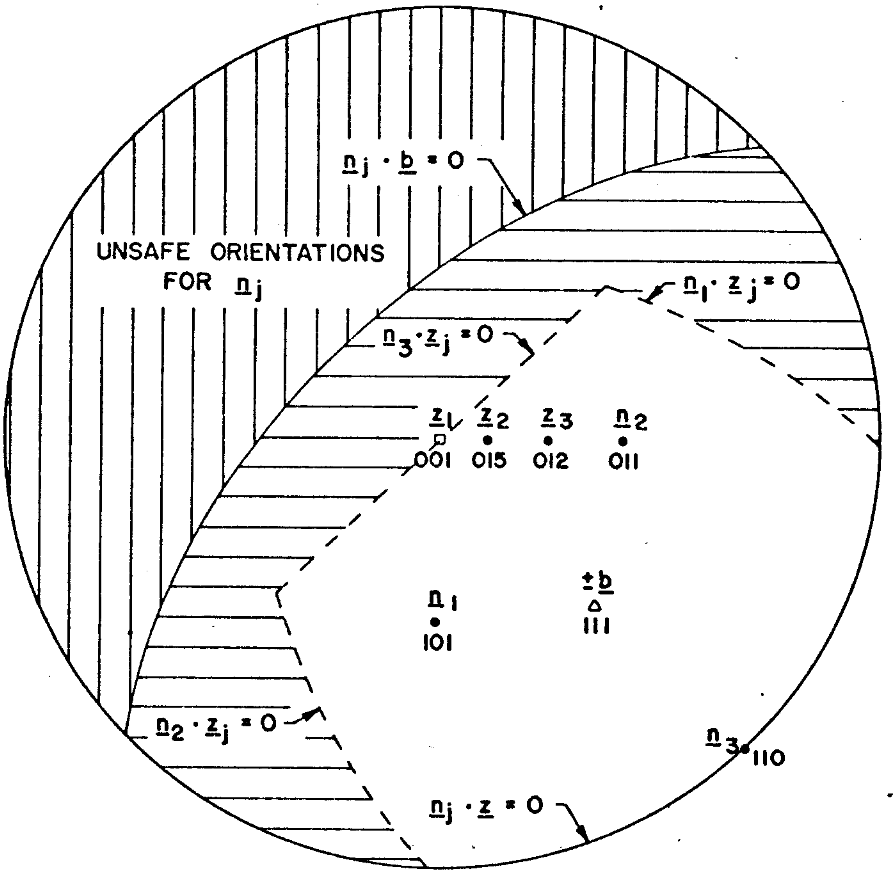

FIGURE 23. Stereographic projection showing those crystal orientations (any z in the unshaded region) where all the possible n's ([101], [011], [110]) are in "safe orientations" for a non-edge loop with a Burgers vector of a/2 [111].

shown, and for the case of $\underline{z} = \underline{z}_1$ only $\underline{n}_3$ is in an unsafe orientation; however, for any $\underline{z}$ in the unshaded region (such as $\underline{z}_2$ and $\underline{z}_3$ which are normally used in this study) all $\underline{n}$'s are in safe orientations and the contrast behavior of the loops with $\pm$ b = a/2 [111] is the same as for pure edge loops and the loop nature is readily determined. This same procedure is similarly applied to loops with the other a/2 <111> type Burgers vectors.

CHAPTER VI

EXPERIMENTAL RESULTS

Introduction

In this chapter the experimental results from a total of 60 irradiated specimens are presented. The irradiated vanadium samples are divided into two distinct groups which reflect differences in annealing environment and sample geometry. In the first group (Group I) the samples were prepared for irradiation as specially machined foil strips (see Figure 12) and annealed at 1050°C for 1 hour in the tandem target chamber (described in Chapter V). The 33 irradiated samples of Group I are listed in Table 5 along with the specific irradiation conditions. The 27 samples of the second group (Group II) were prepared as 3 mm discs and annealed at 1050°C for 1 hour in the special high vacuum furnace described in Chapter V. The samples of Group II are listed in Table 6 along with the irradiation conditions.

The distinction between the results observed in the two groups of samples is the presence of a large amount of irradiation-enhanced precipitation in the samples of Group I and the absence of the same precipitates in the samples of Group II. This difference in the observed microstructure (as will be discussed later) is attributed to the different annealing environments, not to the sample geometry which was conveniently changed at the time of the switch to the new annealing system. The results from

TABLE 5

SAMPLES AND IRRADIATION CONDITIONS FOR GROUP I[a]

Run Number	Sample Code Number	Temperature (^{o}C)	Incident Ion	Ion Energy (MeV)	Fluence (10^{16} ions/cm^{2})
1	T-10-00-13	710	Oxygen	17.5	1.0
2	T-10-00-15	700	Cu	16	0.4
2	T-10-00-16	700	Nb	16	0.016
2	T-10-00-17	700	Cu	16	2.0
3	T-10-00-19	700	Cu	14	1.0
3	T-10-00-20	700	Cu	14	2.0
3	T-10-00-21	700	Cu	14	5.0
3	T-10-00-22	700	Cu	14	0.6
4	T-10-00-24	710	Cu	14	1.0
4	T-10-00-25	710	Cu	14	0.5
4	T-10-00-26	710	Cu	14	2.0
4	T-10-00-27	710	Cu	14	0.6
4	T-10-00-28	710	Cu	14	1.0
5	T-10-00-30	750	Cu	14	0.9
5	T-10-00-31	650	Cu	14	4.0
5	T-10-00-32	650	Cu	14	2.0
5	T-10-00-33	650	Cu	14	1.0
6	T-10-00-36	650	Cu	14	0.5
6	T-10-00-37	650	Ni	14	1.0
6	T-10-00-38	650	Ni	14	0.2
7	T-10-00-40	700	Cu	18	0.7
7	T-10-00-41	700	Cu	18	0.7
7	T-10-00-42	700	Cu	18	0.7
7	T-10-00-43	600	Cu	18	0.7
7	T-10-00-44	600	Cu	18	0.7
8	T-10-00-47[b]	750	Cu	18	0.7
8	T-10-00-48[b]	700	Cu	18	0.7
8	T-10-00-49[b]	650	Cu	18	0.7
8	T-10-00-50	750	Cu	18	0.7
8	T-10-00-51	700	Cu	18	0.7
8	T-10-00-52	650	Cu	18	0.7
9	T-10-00-55[b]	700	Cu	18	0.8
9	T-10-00-56	700	Cu	18	0.8

a) Samples of Group I were prepared as foil strips and annealed in the tandem target chamber.

b) Electropolished after annealing to remove 25 microns.

TABLE 6

SAMPLES AND IRRADIATION CONDITIONS FOR GROUP II[a]

Run Number	Sample Code Number	Temperature (°C)	Copper Ion Energy (MeV)	Fluence (10^{16} ions/cm^2)
10	T-10-00-57	750	18	0.9
10	T-10-00-58[b]	750	18	0.05
11	T-10-00-65	750	18	1.5
11	T-10-00-66	700	18	1.5
11	T-10-00-67	650	18	1.5
11	T-10-00-68	600	18	1.5
11	T-10-00-69[b]	750	18	1.5
11	T-10-00-70[b]	700	18	1.5
11	T-10-00-71[b]	650	18	1.5
11	T-10-00-72[b]	600	18	1.5
12	T-10-00-73[b]	650	18	1.5
12	T-10-00-74[b]	600	18	1.5
12	T-10-00-75[b]	550	18	1.5
12	T-10-00-76[b]	500	18	1.5
13	T-10-00-77[b]	850	14	1.9
13	T-10-00-78[b]	800	14	1.9
13	T-10-00-79[b]	700	14	0.5
13	T-10-00-80[b]	700	14	0.1
13	T-10-00-81[b]	600	14	0.5
13	T-10-00-82[b]	500	14	0.5
13	T-10-00-83[b]	350	14	0.5
13	T-10-00-84[b]	200	14	0.5
14	T-10-00-85	650	14	0.5
14	T-10-00-86	600	14	0.5
14	T-10-00-87	550	14	0.5
14	T-10-00-88	200	14	0.5
14	T-10-00-89	150	14	1.0

a) Samples of Group II were prepared as 3 mm discs and annealed in a special high vacuum furnace.

b) Electropolished after annealing to remove 10 microns.

the transmission electron microscopy (TEM) analysis of the samples in Groups I and II will now be presented.

Group I

Qualitative Results

The results from the samples irradiated during the first 6 irradiations (Runs 1 thru 6) listed in Table 5 do not contribute significantly to the quantitative results. During these first 6 irradiations considerable testing of the heavy-ion source and optimizing of the various ions beams were performed to determine beam stability and which ion beams (and charge states) would be suitable for irradiation damage experiments. The first six irradiations were also a time for testing of the target chamber facility and installing (or improving) diagnostic devices for measuring temperature, beam current on target, and integration of that current. In addition, the samples from these irradiations were used to test and perfect the various techniques to prepare the irradiated samples for TEM analysis; as a result, many of the examined samples showed no damage (too much surface removed) or lacked the necessary thin area for TEM work (poor final thinning technique). In those samples which showed damage, it was difficult to correlate the observed microstructural changes with a specific damage level or temperature since beam instabilities produced considerable error in the estimate of the integrated current, the temperature was not always accurately known, and the amount of surface removed to expose the damage varied considerably. These samples did, however, provide initial information concerning the irradiation produced microstructure (voids and a high density of precipitates) and provided the specimens necessary to perfect the TEM preparation techniques, which could only be tested on irradiated samples.

Through the experience gained during the irradiation and subsequent preparation of the samples from Runs 1 thru 6, the samples irradiated in Runs 7, 8 and 9 were irradiated under well characterized conditions and were prepared for TEM analysis by techniques which had been perfected to give reproducible surface removal, an accurate measure of the amount removed, and a high percentage of successfully thinned samples. The changes in microstructure observed in these irradiated samples are similar to the changes observed in those samples (which were successfully prepared for TEM analysis) from Runs 1 thru 6. These irradiation produced changes in the microstructure will now be described.

The main microstructural changes observed in the irradiated samples of Group I are the formation of both voids and precipitates. The precipitates (and the voids) were not observed in any unirradiated samples subject to the same thermal treatment and vacuum conditions. Transmission electron micrographs of the void and precipitate microstructure that developed is shown in Figure 24 for samples irradiated (as annealed) at 600, 650, 700, and 750°C with 18 MeV copper ions to 1 dpa (damage examined at a depth of about 1 micron). The microstructures shown in Figure 24 are representative of the microstructures observed in the other samples of Group I, with the exception discussed in the following paragraph.

In an effort to shed some light on the source and possible solution to the precipitate problem, several samples of Group I were electropolished (as indicated in Table 5) to remove approximately 25 microns from the surface after annealing and before irradiation. These samples were then irradiated at 650, 700, and 750°C under the same conditions as other samples in Group I which had not been electropolished. The void and precipitate microstructures in the samples irradiated with 18 MeV Cu ions to 1 dpa at 650 and 700°C after electropolishing are shown in Figure 25; no damage was observed in the sample irradiated at 750°C. The microstructure of these samples differs dramatically from the microstructure observed in the other samples of Group I (Figure 24). The samples which were electropolished show a significant reduction in the precipitate volume (about a factor of 100), a decrease in void size, and an increase in void density.

Voids were observed to form under irradiation at all temperatures (600-750°C), but the void distribution was noticeably more inhomogeneous at the higher temperatures. The average void size increased with temperature, the void density decreased with temper-

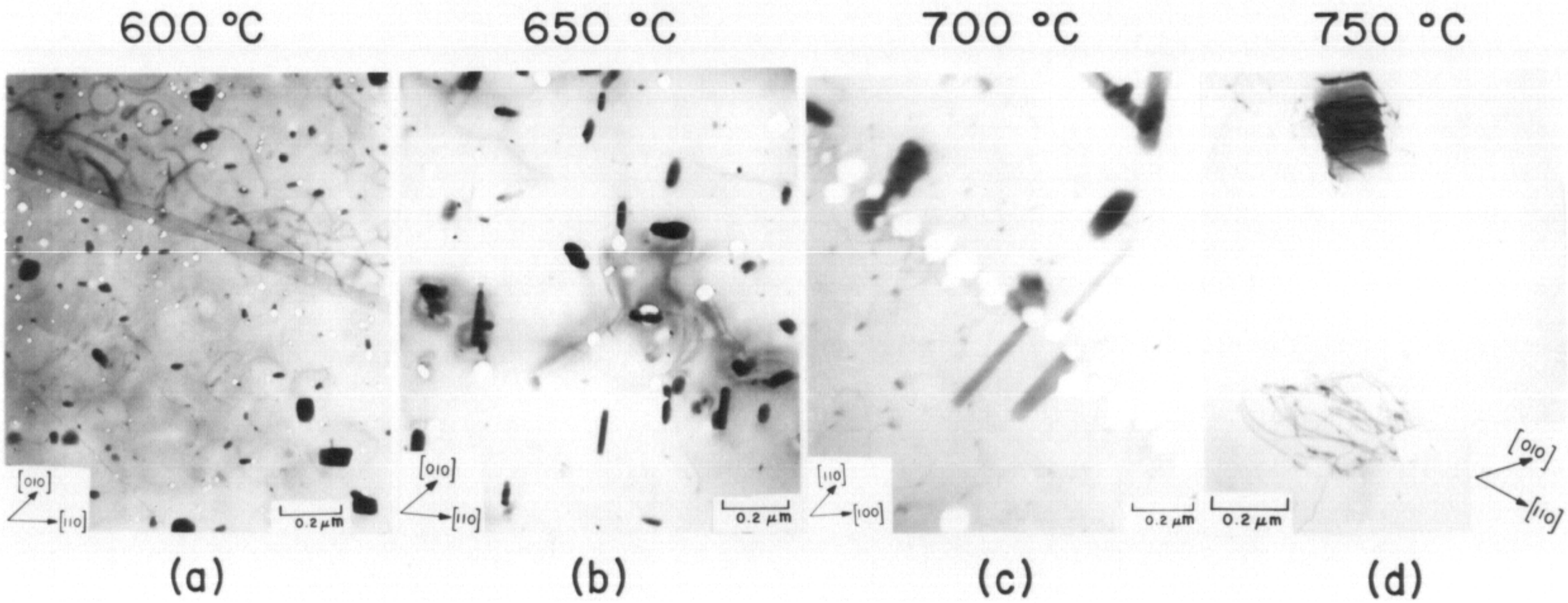

FIGURE 24. Void and precipitate microstructure in the vanadium samples of Group I irradiated with 18 MeV copper ions to 1 dpa.

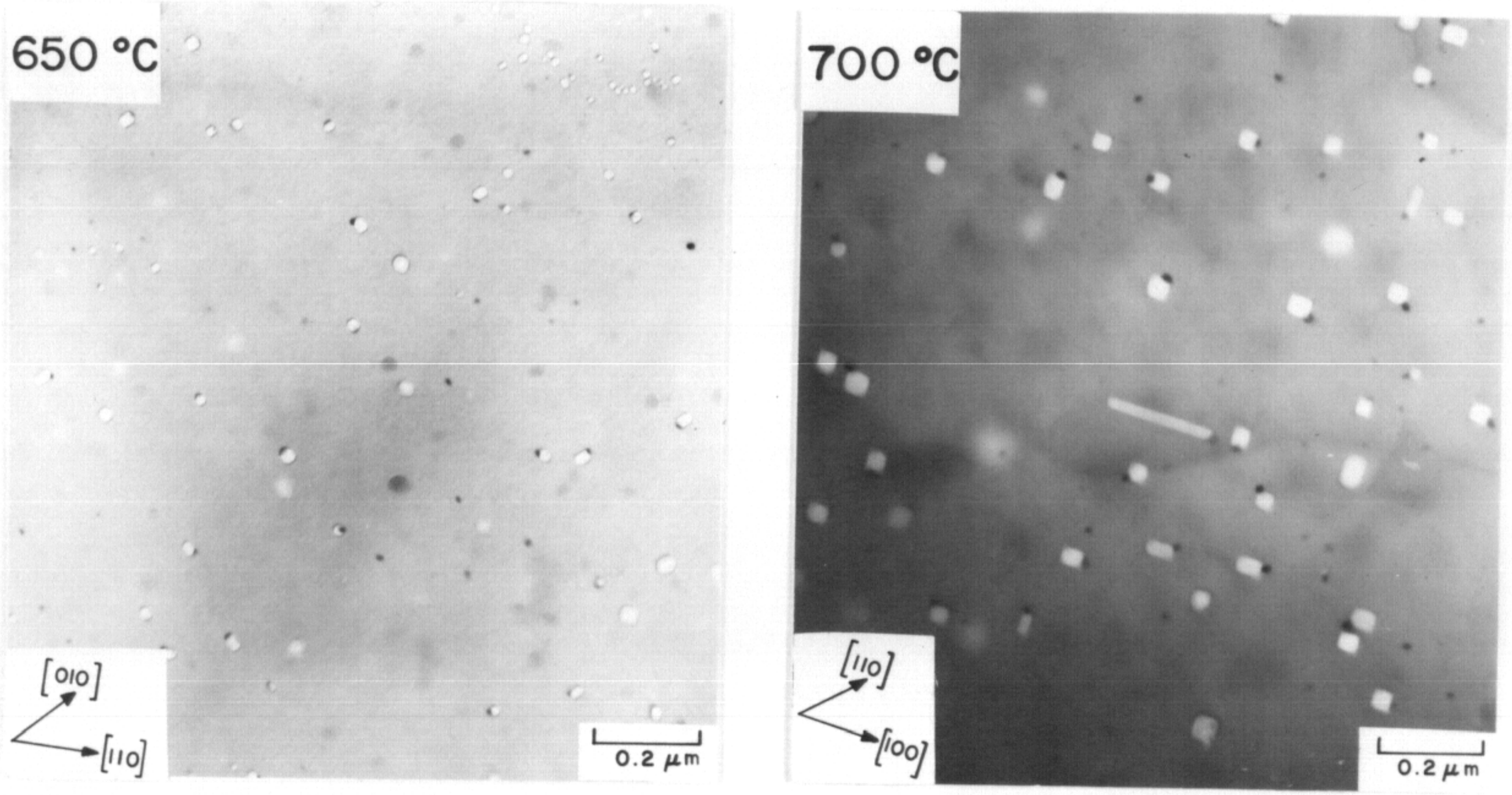

(a) (b)

FIGURE 25. Void and precipitates in the vanadium samples of Group I which were electropolished after annealing and then irradiated with 18 MeV copper ions to 1 dpa.

ature and the peak swelling occurred at 700°C. In general, the voids were found to be cubes with {100} faces, but some of the voids also exhibited some {110} and {111} faceting of the {100} cubes. Elongated voids were also observed, but only in the sample irradiated at 700°C after electropolishing (Figure 25b). Density measurements indicate that about 3% of the voids in this sample are of this morphology. These voids are elongated in $\langle 100 \rangle$ directions, are bounded by {100} planes, and typically have length to width ratios of up to ten.

The precipitates formed only under irradiation and were observed at all irradiation temperatures. The precipitate volume increased with temperature and the density decreased. As in the case for voids, the precipitate distribution was very inhomogeneous at the higher temperatures. Results concerning the nature of these precipitates will be presented in the section immediately following this section. In addition to the large precipitates discussed above and evident in Figure 24, there was another precipitate type observed only at 600°C. This type was a fine rod-shaped precipitate with its axis along one of the $\langle 100 \rangle$ directions. These precipitates are visible in the micrograph of Figure 24a.

Other microstructural features observed in the samples of Group I include void and precipitate clustering, void and precipitate denuded regions along grain boundaries, dislocation loops, dislocation networks, and dislocation punching from the large precipitates. The cluster of voids and precipitates observed in Figure 24c was determined to be a two dimensional wall (rather than a line) by stereo TEM techniques. Void and precipitate walls were observed in several samples containing extensive precipitation. A void wall that is denuded of precipitates is shown in Figure 26. Void and precipitate denuding along grain boundaries is shown in Figure 27 and there is also some evidence for grain boundary migration in the same micrograph. The dislocation structure in the samples irradiated (as annealed) at 600, 650, 700, and 750°C to 1 dpa is shown in Figure 28. Dislocation loops were observed in all these samples and considerable dislocation punching from the large precipitates was observed at the higher temperatures (Figure 28c, d). The dislocation density was difficult to determine at 700 and 750°C because of the intense tangle of dislocation formed by the precipitates. The dislocation structure in the samples irradiated, after electropolishing, to 650°C and 700°C is shown in Figure 29. The dislocation density in these samples is considerably reduced due to the lack of large precipitates which punch dislocations; dislocation loops were not observed in any significant density in the samples of Figure 29.

Nature of the Group I Precipitates

In this section the results from experiments to determine the nature of the large precipitates observed in the samples of

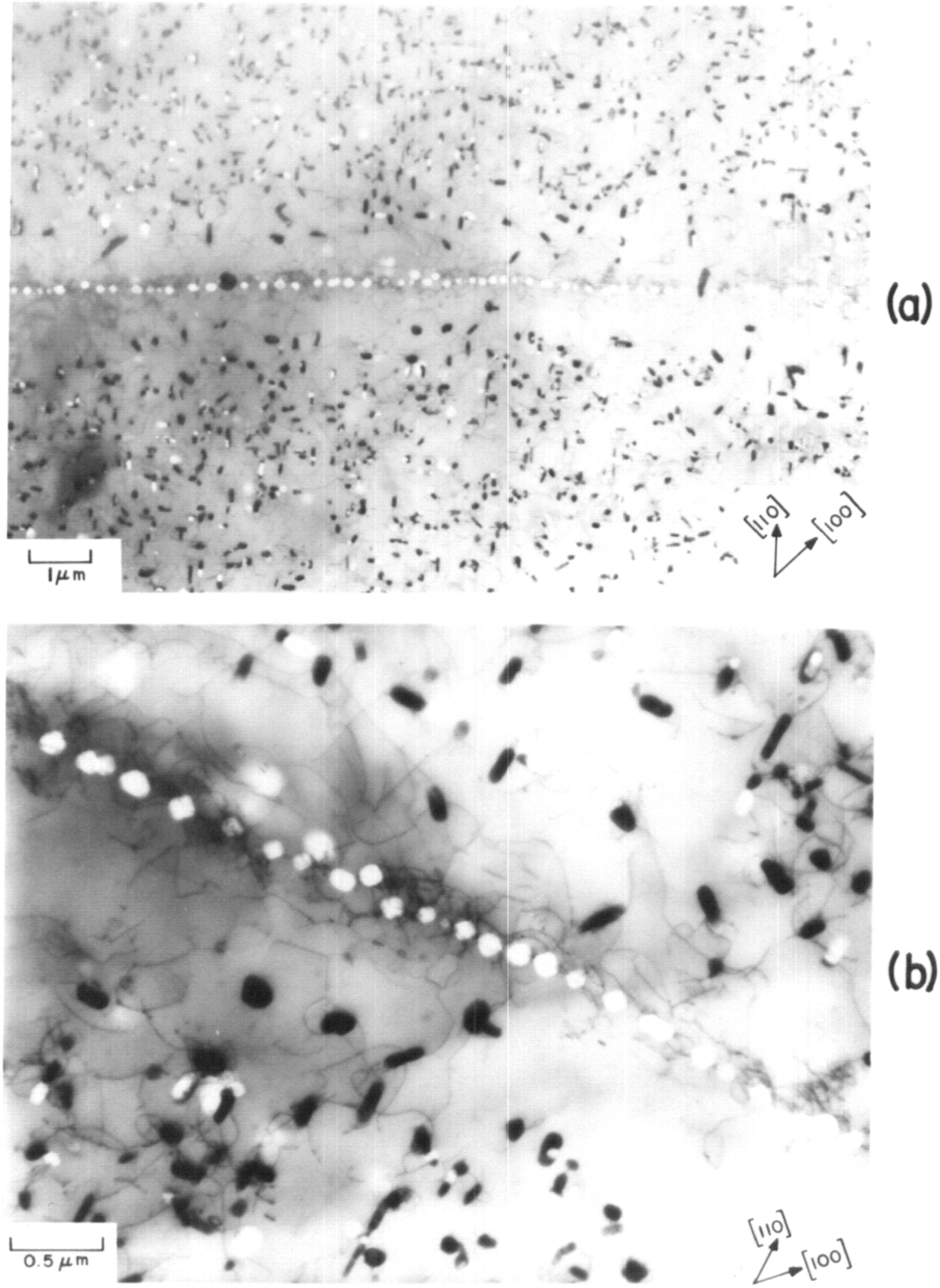

FIGURE 26. Void wall in vanadium (Group I) irradiated at 650°C with 14 MeV copper ions to 5 dpa.

FIGURE 27. Void and precipitate denuding along grain boundaries in vanadium (Group I) irradiated at 650°C with 14 MeV Cu ions to 5 dpa.

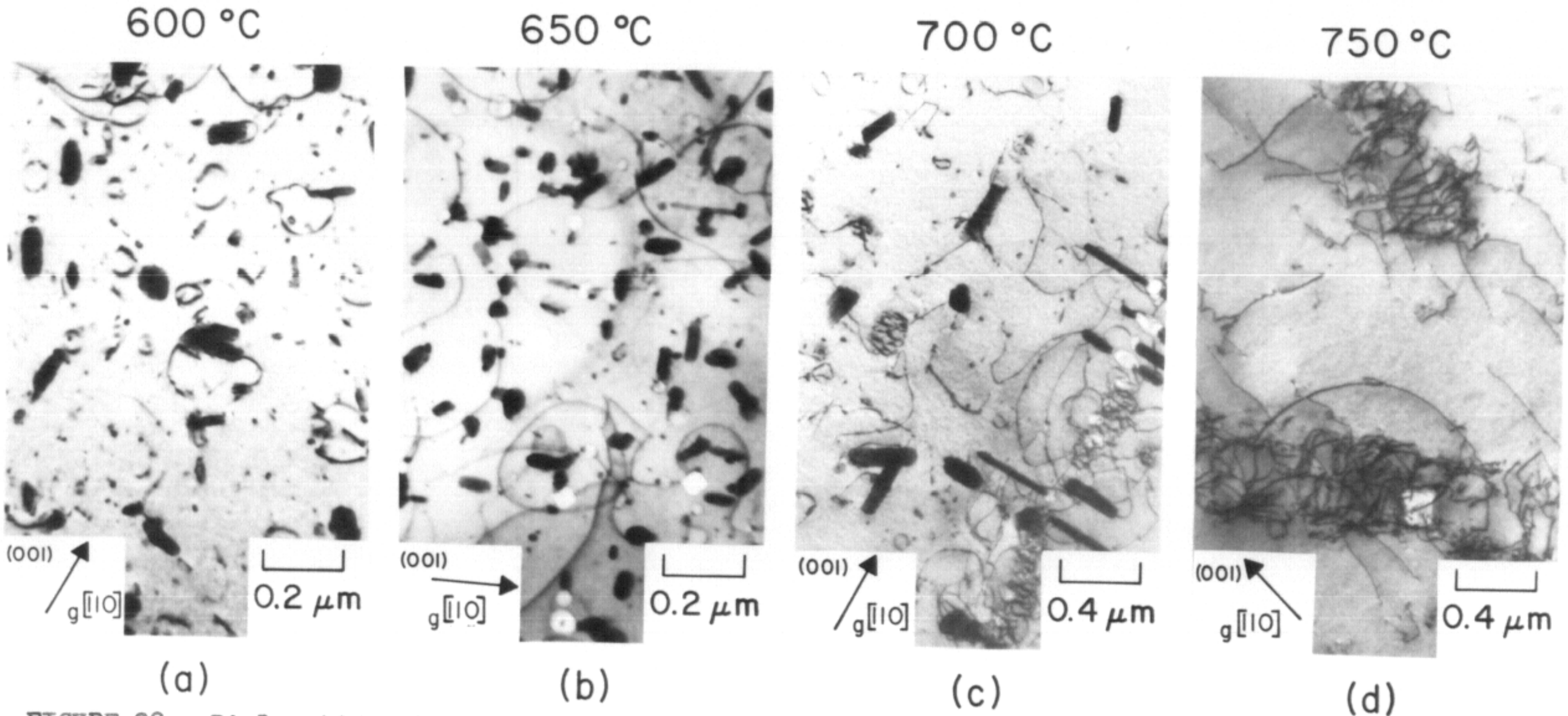

FIGURE 28. Dislocation structure in the vanadium samples of Group I irradiated "as annealed" with 18 MeV copper ions to 1 dpa.

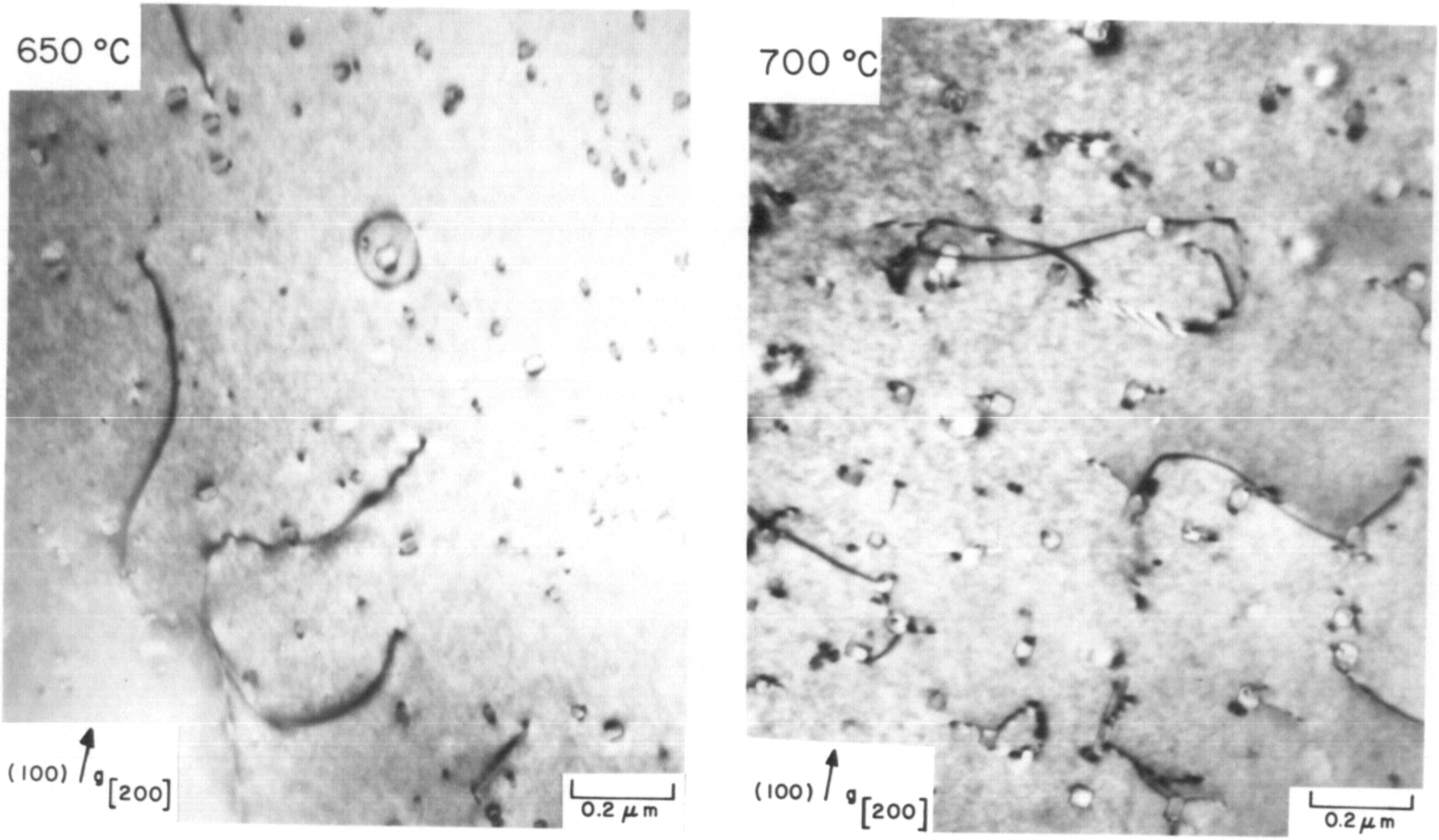

(a) (b)

FIGURE 29. Dislocation structure in the vanadium samples of Group I electropolished after annealing and irradiated with 18 MeV copper ions to 1 dpa.

Group I are presented.

Vanadium is easily contaminated with interstitial impurities; thus, it is important to know the interstitial impurity content as a function of depth. In an effort to obtain this information, several samples were sent to the Grumman Aerospace Corp. for analysis of the carbon, oxygen, and nitrogen concentrations as a function of distance from the surface. These samples and the treatment each received are listed in Table 7. The results of the analysis by Grumman(126) are given in Table 8.

The carbon and oxygen concentrations in the surface region (0.-0.5 micron) are higher than in the bulk region (0.5-3.6 microns), but such surface contamination is expected in vanadium. In all the samples the carbon and oxygen concentrations fall to bulk values within 0.5 microns of the surface(126). These values for the carbon and oxygen concentrations and the single value for the nitrogen are in close agreement with the values given in Table 4.

After the samples were returned from Grumman, TEM analysis of Sample 5 (see Table 7) revealed the presence of voids and precipitates as shown in Figure 30. The precipitates are identical to the precipitates observed in the other samples of Group I. Since all TEM analysis is carried out at depths greater than 0.5 microns from the surface, the results of Table 8 indicate that the observed

TABLE 7

DESCRIPTION OF SAMPLES SENT TO GRUMMAN AEROSPACE CORPORATION FOR DEPTH ANALYSIS OF C, O, N CONCENTRATIONS

Sample 1	(C-10-00-8) As received vanadium that has been electropolished to remove 25 microns from the surface.
Sample 2	(C-10-00-9) Initially in the same state as Sample 1, but then annealed at 1050°C for 1 hour in the tandem target chamber.
Sample 3	(C-10-00-10) Initially in the same state as Sample 2, but 5.5 microns removed from the surface by electropolishing after the anneal.
Sample 4	(C-10-00-11) Initially in the same state as Sample 2, but 17.5 microns removed from the surface by electropolishing after the anneal.
Sample 5	(T-10-00-56) Initially in the same state as Sample 2, but sample was then irradiated.
Sample 6	(T-10-00-55) Initially in the same state as Sample 2, but 15 microns removed from the surface by electropolishing after the anneal. Sample was then irradiated.
Sample 7	(T-10-00-54C) Initially in the same state as Sample 2, but 15 microns removed from the surface by electropolishing after the anneal. Sample was then exposed to irradiation vacuum environment.
Sample 8	(C-10-00-12) As received vanadium.

TABLE 8

IMPURITY CONCENTRATION AS A FUNCTION OF DEPTH IN THE VANADIUM SAMPLES OF TABLE 7[a]

Sample[b]	Carbon Concentration (wt-ppm)		Oxygen Concentration (wt-ppm)		Nitrogen Concentration (wt-ppm)	
Number	0-0.5 microns	0.5-3.5 microns	0.05 microns	0.5-3.5 microns	0-0.5 microns	0.5-3.5 microns
1	260 ± 30	9 ± 2	450 ± 80	130 ± 40	-	-
2	100 ± 10	16 ± 2	770 ± 80	80 ± 30	-	-
4	205 ± 40	18 ± 3	630 ± 90	50 ± 25	-	-
5	435 ± 25	18 ± 3	450 ± 70	160 ± 45	-	-
6	350 ± 25	17 ± 3	760 ± 80	90 ± 40	-	<90
8	1435 ± 45	12 ± 3	5600 ±200	70 ± 30	-	-

a) Analysis by the Grumman Aerospace Corporation(126).

b) Samples 3 and 7 were not analyzed.

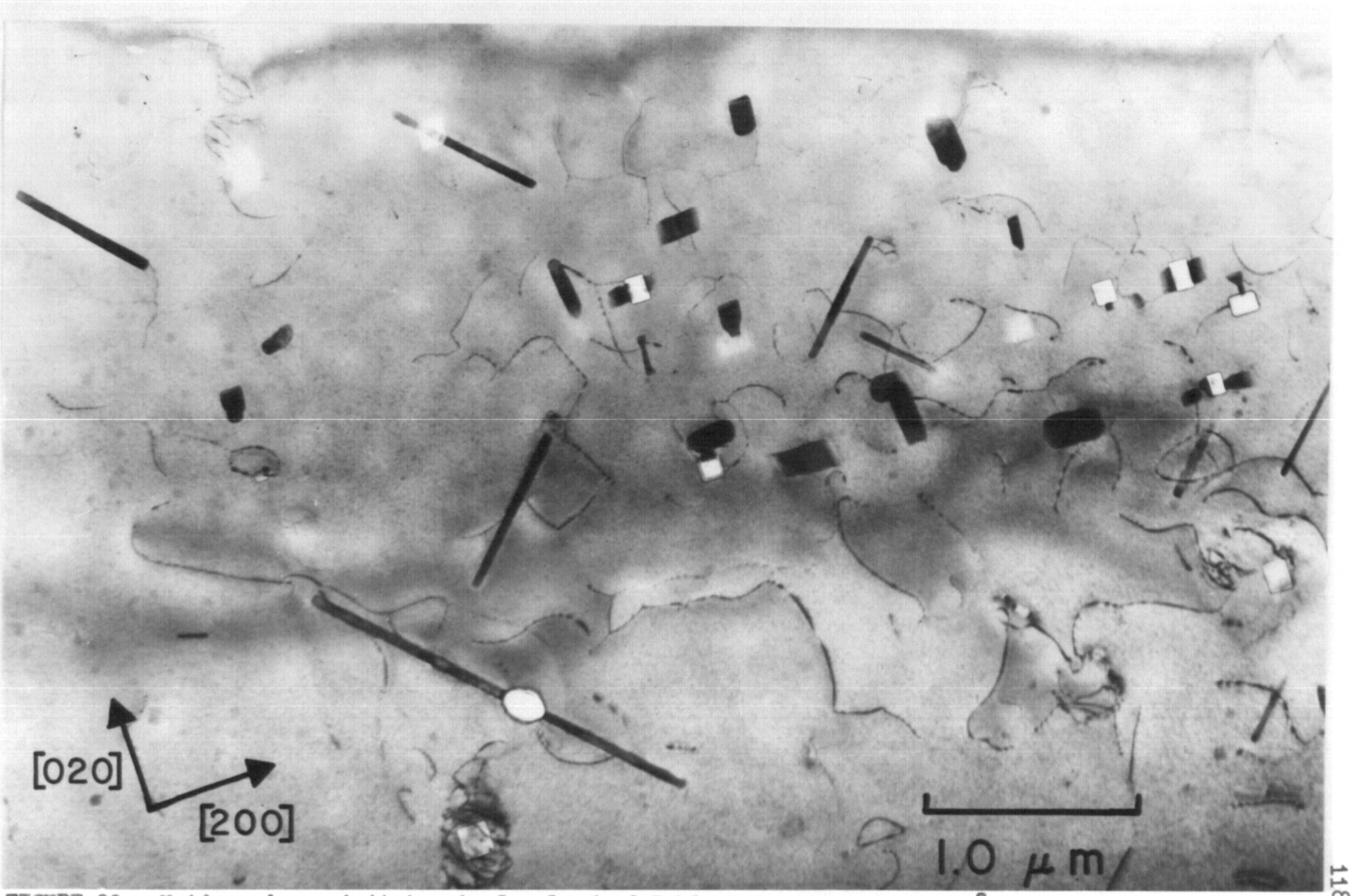

FIGURE 30. Voids and precipitates in Sample 5 of Table 7 irradiated at 700°C to 1 dpa.

precipitates are not the result of carbon, oxygen, or nitrogen contamination.

Electron diffraction analysis of two precipitates in Sample 5, shown in Figure 31a, yielded the precipitate reflections in the diffraction pattern of Figure 31b. The precipitate spots form a well-defined pattern (the secondary precipitate spots in the $[1\bar{1}0]_V$ direction are the result of double diffraction). The precipitate reflections show zero misfit in the $[110]_V$ direction and a misfit of 12% in the $[1\bar{1}0]_V$ direction. The d-spacings associated with the precipitate pattern are 6.24 Å in the $[110]_V$ direction and 4.79 Å in the $[1\bar{1}0]_V$ direction. The integer ratio of precipitate and vanadium d-spacings in the $[110]_V$ direction (no misfit) explains the preferred growth of the precipitates of Figure 31a in the $[110]_V$ direction. This preferred growth of the precipitates in $\langle 110\rangle_V$ directions is also exhibited in Figures 24 and 30. The other precipitate shapes observed in Figure 30 (and 24) are just different orientations of the same type of precipitate. In general the precipitates are slab-like, grow in $\langle 110\rangle_V$ directions, and are bounded in the other two dimensions by $\{001\}_V$ and $\{1\bar{1}0\}_V$ planes. This shape is shown in Figure 32 with the relative directions in the vanadium matrix given. Diffraction patterns at other orientations have not been obtained.

The use of an energy dispersive x-ray analysis system on the JEOL 100B electron microscope has allowed an elemental

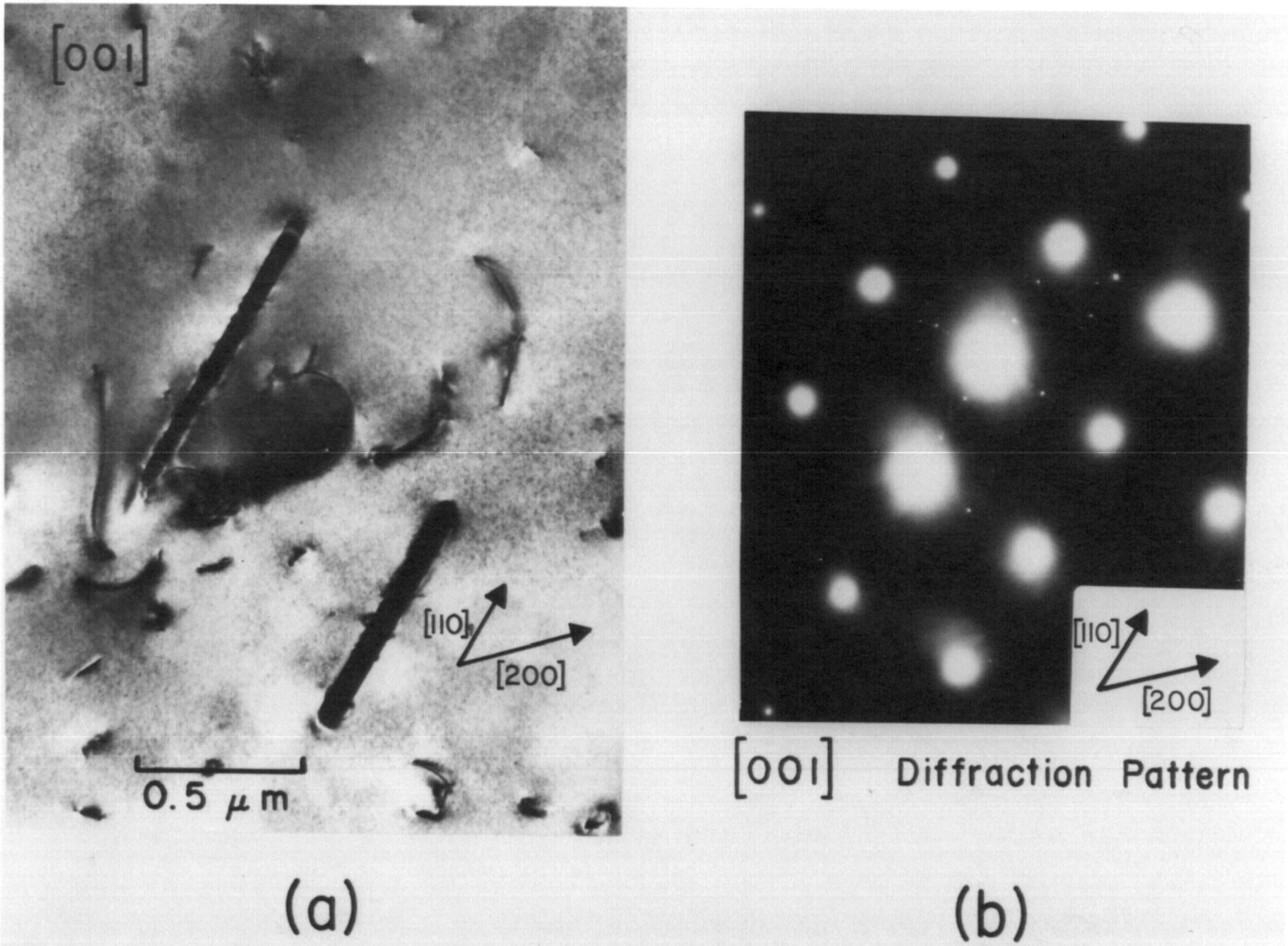

FIGURE 31. Precipitates and their diffraction pattern in Sample 5 of Table 7.

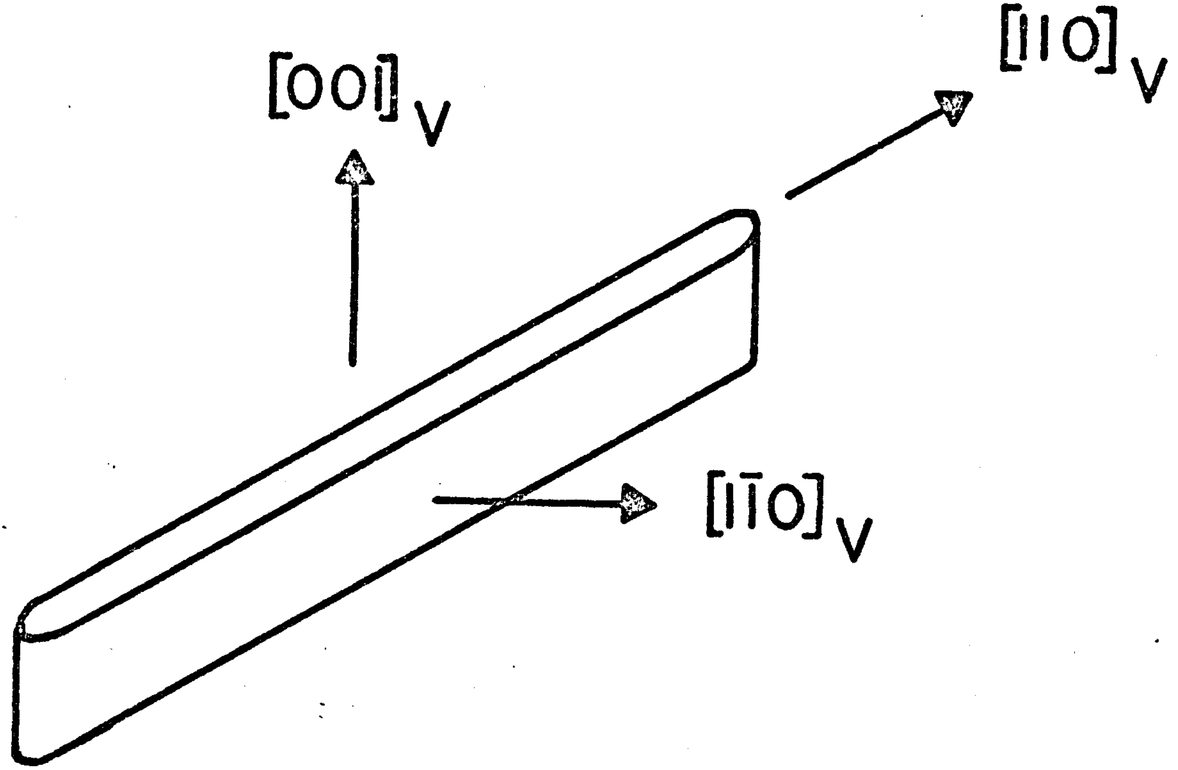

FIGURE 32. The general shape of the large precipitates in the samples of Group I and their orientation relative to the vanadium matrix.

analysis of the precipitates in question. The spectra of Figure 33 are some of the results of that work. The nickel-kα peak in the spectra of Figure 33 is significantly increased when the electron beam is placed on a precipitate and is almost negligible in the matrix. (The copper peaks shown are from the sample holder.) Spectra similar to those in Figure 33 were obtained whenever a comparison between precipitate and matrix were made. The results of Figure 33 clearly indicate that the precipitates contain nickel. A quantitative analysis of the nickel content was not possible due to the presence of the copper peak. (Quantitative analysis would have been possible if a graphite sample holder had been used, but such a holder was not available for use during the course of this investigation.)

The precipitates have, therefore, been identified as nickel bearing, but the exact composition and structure remains unknown since none of the known vanadium-nickel phases has a structure indicated by the diffraction pattern in Figure 31b. The precipitate is undoubtably a unstable phase with a vanadium superlattice structure that forms during irradiation.

Quantitative Results

Quantitative data on the irradiation produced defects were obtained using the procedures described in Chapter V. Errors in the quantitative data arise from several sources. The main sources of error are listed in Table 9. The total error in the

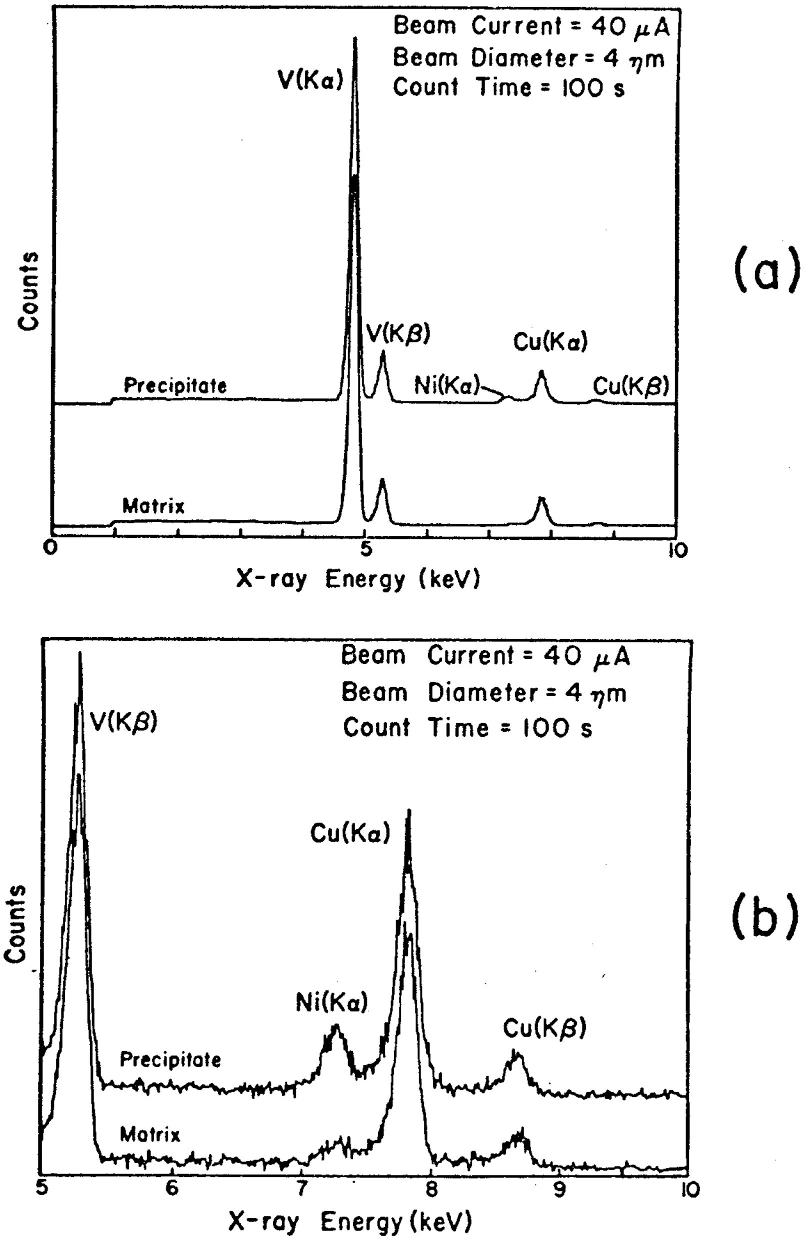

FIGURE 33. Energy dispersive x-ray analysis of a precipitate and an adjacent region of matrix in an irradiated sample of Group I (T-10-00-56).

TABLE 9

SOURCES OF ERROR IN THE QUANTITATIVE DATA

Source	Estimated Error
Magnification (TEM)	± 5%
Foil Thickness	± 10% to ± 15%
Sampling Error	± 5% to ± 10%
Length Measurements (Defect Size)	± 5%
Temperature	± 5°C
dpa (Beam Current)	± 10% to ± 30%
dpa (Step Height Measurement)	± 30% to ± 40%
Total Damage	± 30% to ± 50%

values of number densities is estimated to be ±25% to ±40%, depending on the number of voids counted, and the error in mean defect size is taken to be on the order of ±10%. In addition to the errors in the measurement of the observed defect structures, there are errors (also listed in Table 9) in the damage (dpa) and temperature for each sample; these are estimated to be ±30% to ±50% and ±5°C, respectively.

Quantitative data of the void and precipitate microstructure in the samples of Group I are given in Table 10. The average void size, the void density, and the void swelling are plotted as a function of temperature in Figures 34, 35, and 36, respectively, for the samples of Group I irradiated with 18 MeV copper ions to 1 dpa. The average void size increases and the void density decreases with increasing temperature. In the samples electropolished after annealing,the average void size is reduced and the void density is increased. The effect of electropolishing on the void size distributions is shown in Figure 37. At 650°C the void size distribution is shifted to smaller sizes in the sample which was electropolished after annealing. At 700°C the void size distribution is also shifted to smaller sizes and is much narrower in the electropolished sample. The peak in the void swelling curve occurs at 700°C in both sets of samples (as annealed and electropolished); at the peak swelling temperature the decreases in void size in the electropolished sample is offset by the increase in void

TABLE 10

SUMMARY OF VOID AND PRECIPITATE DATA FOR THE VANADIUM SAMPLES OF GROUP I

Temperature (°C)	dpa	Average Void Size (Å)	Void Density (cm^{-3})	V/V (%)	Average Precipitate Volume (cm^3)	Precipitate Density (cm^{-3})
600	1	140	2×10^{14}	0.1	1×10^{-16}	2×10^{14}
600	1.5	270	7×10^{13}	0.15	4×10^{-17}	3×10^{14}
650	1	370	1×10^{14}	0.5	4×10^{-17}	2×10^{14}
650	2	750	2×10^{13}	1.0	4×10^{-16}	7×10^{13}
650	5	760	5×10^{13}	2.5	4×10^{-16}	8×10^{13}
650	1[a]	160	4×10^{14}	0.2	4×10^{-19}	8×10^{14}
700	1	590	5×10^{13}	1.0	3×10^{-16}	6×10^{13}
700	1	730	2×10^{13}	1.0	1×10^{-15}	2×10^{13}
700	3	850	2×10^{12}	0.1	4×10^{-15}	4×10^{12}
700	1[a]	410	1.3×10^{14}	1.0	1×10^{-18}	3×10^{14}
750	1	980	3×10^{11}	0.03	3×10^{-15}	1×10^{12}
750	1[a]	None Observed				

a) These samples had a 25 micron surface layer removed after annealing.

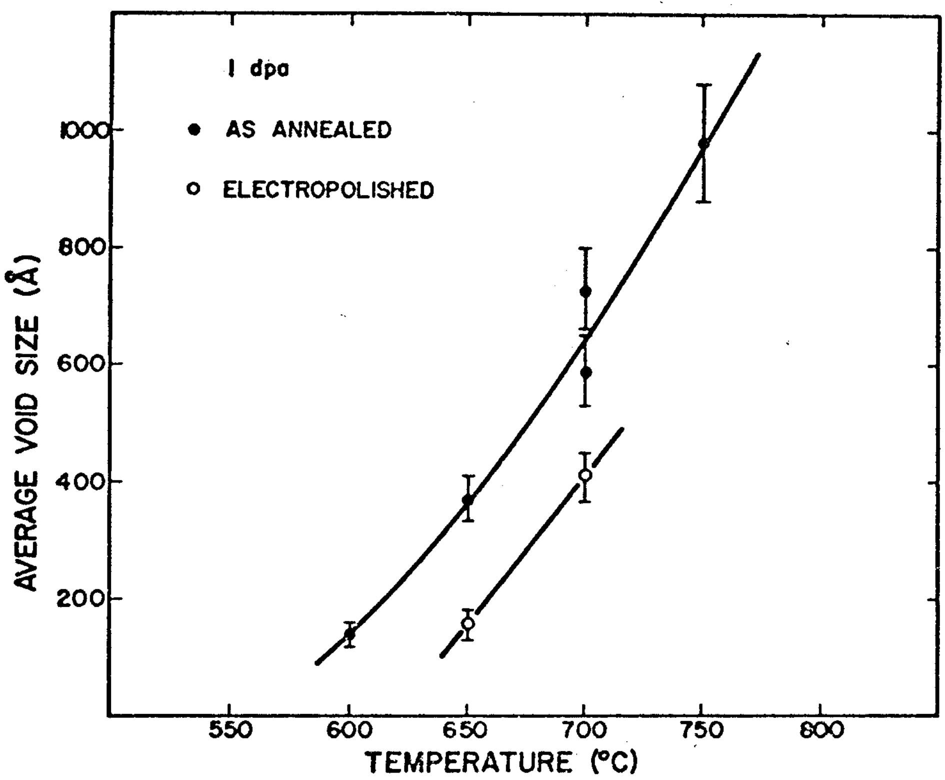

FIGURE 34. Average void size as a function of temperature for the vanadium samples of Group I irradiated to 1 dpa.

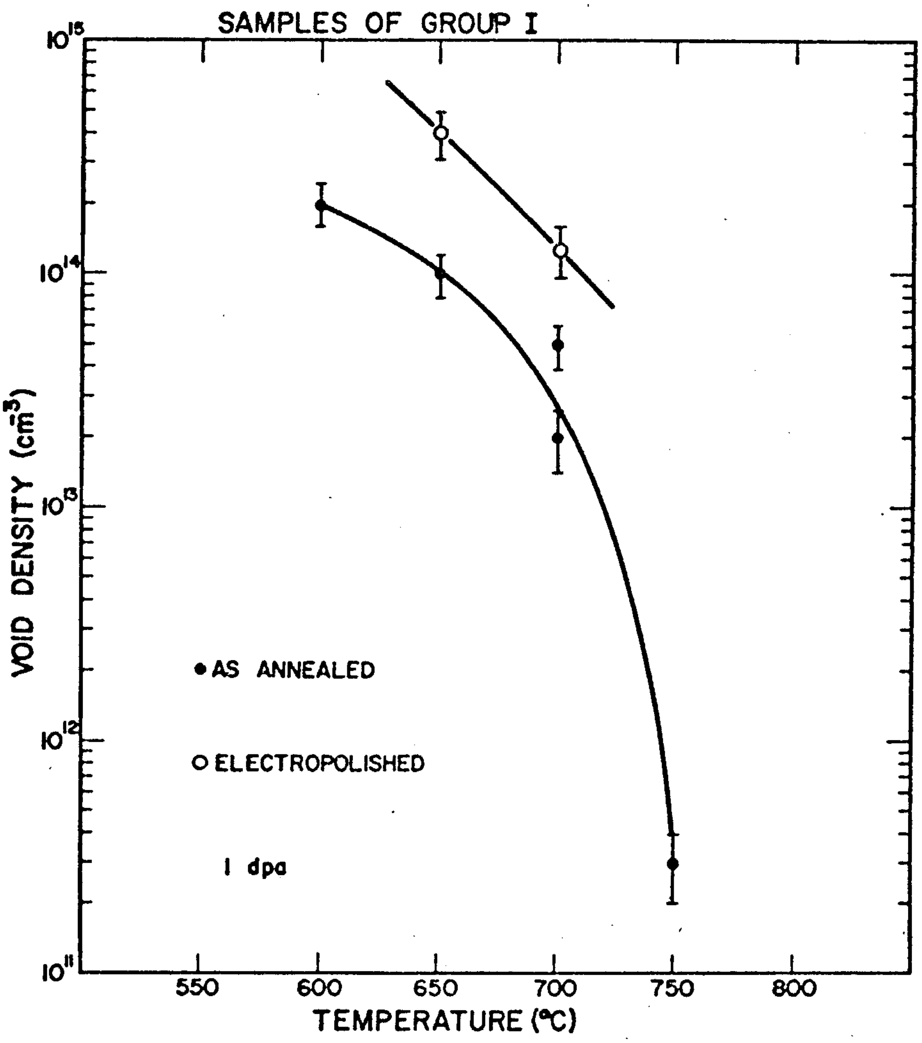

FIGURE 35. Void density as a function of temperature for the vanadium samples of Group I irradiated to 1 dpa.

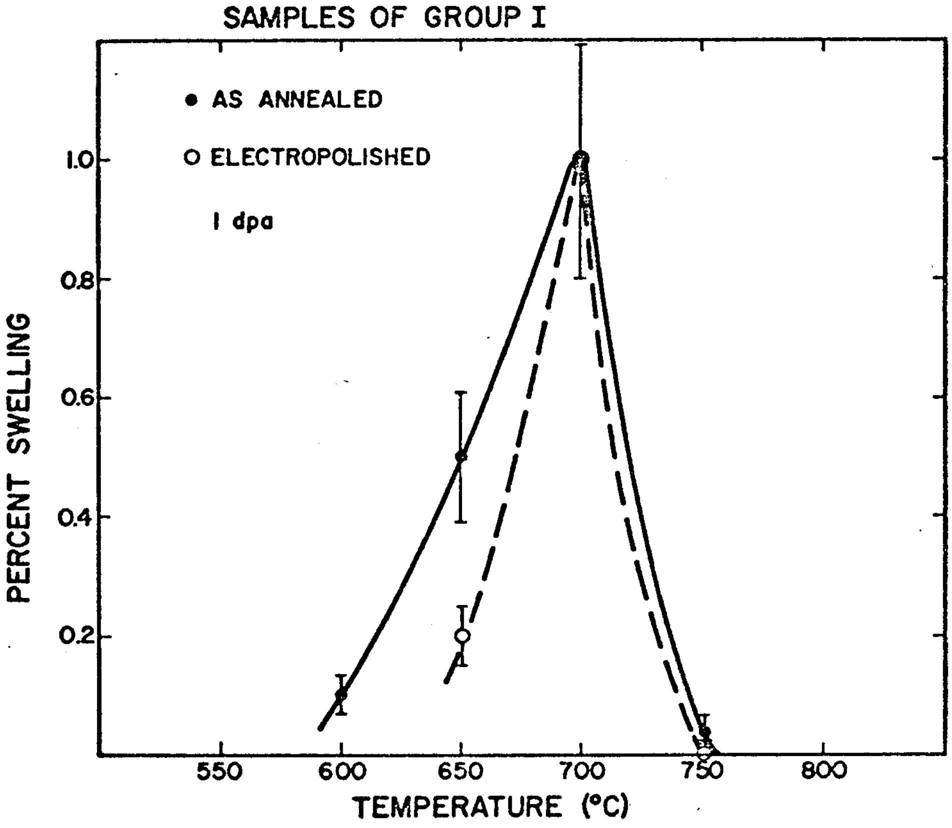

FIGURE 36. Void swelling as a function of temperature for the vanadium samples of Group I irradiated to 1 dpa.

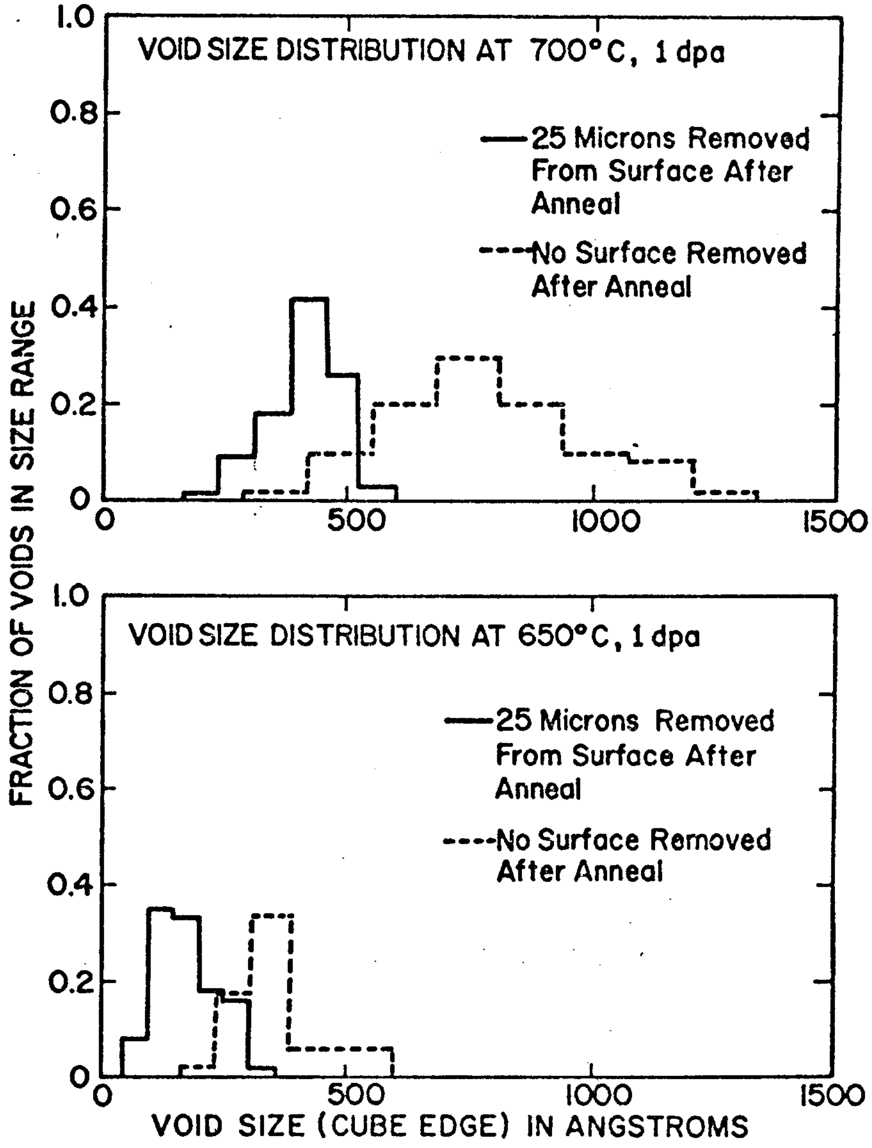

FIGURE 37. Void size distribution in vanadium (Group I) irradiated at 650 and 700°C to 1 dpa after different post-annealing treatments.

density resulting in no net change in swelling. At the other temperatures, the effect of electropolishing is to decrease the observed swelling.

The results of Table 10 show that with increasing temperature the precipitate volume increases and the precipitate density decreases. The effect of electropolishing after annealing and prior to irradiation is to decrease the precipitate size and increase the precipitate density. The overall effect of electropolishing is to significantly decrease the total amount of nickel impurity which precipitates out.

The quantitative data on the dislocation substructure in the samples of Group I are given in Table 11. In general, the dislocation loop diameter increased with temperature; however, the loop density is much less sensitive to changes in temperature. The network dislocation densities are also not affected to any measurable degree by changes in temperature. The higher dislocation densities in the samples irradiated as annealed are the result of dislocations introduced in the lattice by the growing precipitates. These large precipitates punch dislocations into the lattice, and these dislocations form the tangles observed in Figures 28c and 28d. The dislocation densities in these tangles approach $10^{12}/cm^2$ at 700 and 750°C; this high density of dislocations introduced by the precipitates makes it extremely difficult to estimate the true dislocation density as a function of

TABLE 11

SUMMARY OF THE DISLOCATION DATA FOR THE SAMPLES OF GROUP I

Temperature (°C)	dpa	Average Loop Diameter (Å)	Loop Density (cm^{-3})	Network Dislocation Density (cm^{-2})
600	1	150	4×10^{13}	3×10^{9}
600	1.5	200	4×10^{13}	4×10^{9}
650	1	250	2×10^{13}	4×10^{9}
650	2	300	1×10^{13}	3×10^{9}
650	5	350	5×10^{12}	6×10^{9}
650	1[a]	-	$<1 \times 10^{12}$	3×10^{8}
700	1	400	1×10^{13}	4×10^{9}
700	1	400	5×10^{13}	2×10^{9}
700	3	500	5×10^{13}	5×10^{9}
700	1[a]	-	1×10^{12}	7×10^{8}
750	1	500	$<2 \times 10^{13}$	6×10^{9}
750	1[a]	-	-	1×10^{8}

a) These samples had a 25 micron surface layer removed after annealing.

temperature.

Group II

Qualitative Results

The major irradiation-induced change in microstructure observed in the vanadium samples of Group II was the formation of voids from 200 to 700°C. The large precipitates which were found in the samples of Group I are absent in the samples of Group II. The formation of voids in the precipitate-free matrix of the Group II samples is clearly shown in the micrograph of Figure 38. Although none of the nickel bearing precipitates (identified in the samples of Group I) were found in the samples of Group II, there were some fine rod-shaped precipitates in several samples irradiated in a narrow temperature range (500 to 600°C). These fine precipitates and their effects will be described in more detail below.

In the first series of irradiations (Runs 10 and 11 in Table 6), two sets of samples were irradiated at 600, 650, 700, and 750°C with 18 MeV copper ions and examined at a depth corresponding to 2 dpa. One set of samples was irradiated as annealed; the other set was electropolished after annealing, then degassed in the tandem target chamber at 750°C before irradiation. No voids were observed in either set of samples irradiated at 750°C. At 600°C the void distribution was very inhomogeneous as shown in

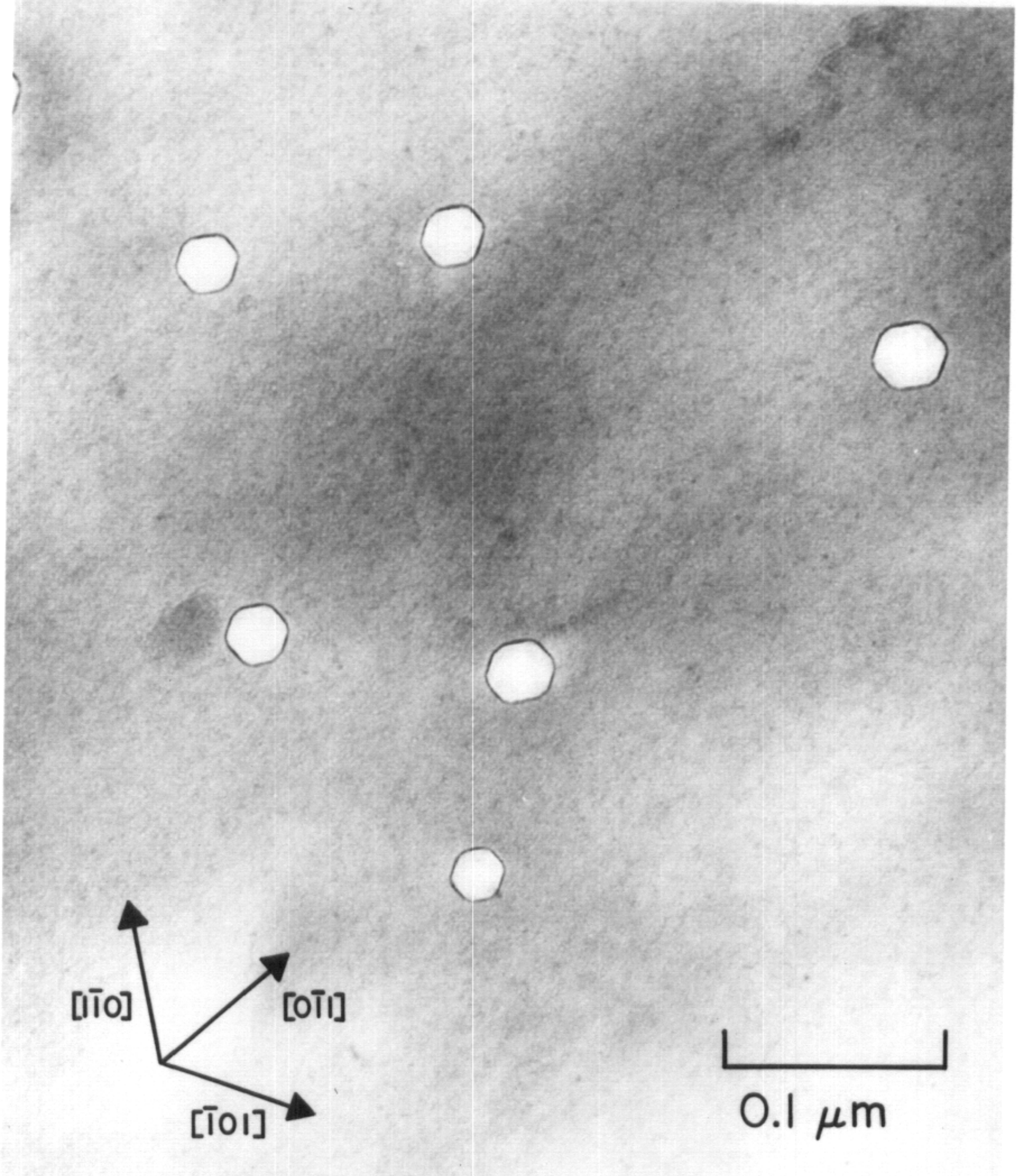

FIGURE 38. Voids in the precipitate-free matrix of a sample in Group II irradiated with 18 MeV Cu ions to 2 dpa.

Figures 39 and 40. In Figure 39 the sample was irradiated as annealed; the void density was extremely low (less than 10^{12} voids/cm^3) in over 99% of the thin area and much higher (about 10^{14} voids/cm^3) in less than 1% of the thin area. Even within the region of high void density at 600°C (Figure 39b) the void distribution is noticeably inhomogeneous with short void strings visible. The sample in Figure 40 was electropolished after annealing, outgassed at 750°C, and irradiated at 600°C. The void density in this latter sample was very low (10^{12} voids/cm^3) and inhomogeneous throughout the grain interiors (Figure 40a) but was much higher (10^{14} voids/cm^3) and more homogeneously distributed along the grain boundaries (Figure 40b). In both samples irradiated at 600°C a low density of fine rod-shaped precipitates was observed. The void structure in the sample which was electropolished after annealing, outgassed at 750°C, then irradiated at 650°C is shown in Figure 41. The void density in this sample irradiated at 650°C is also inhomogeneous, but not to the same extent as at 600°C. As in Figure 40, the void density at 650°C was much higher along the grain boundaries (Figure 41b). No precipitates were observed in the sample irradiated at 650°C. (The sample irradiated as annealed at 650°C was not successfully prepared for TEM). At 700°C the voids were more uniformly distributed throughout the grain interiors. The void structure in the two samples irradiated at 700°C is shown in Figure 42. The sample shown in Figure 42a was

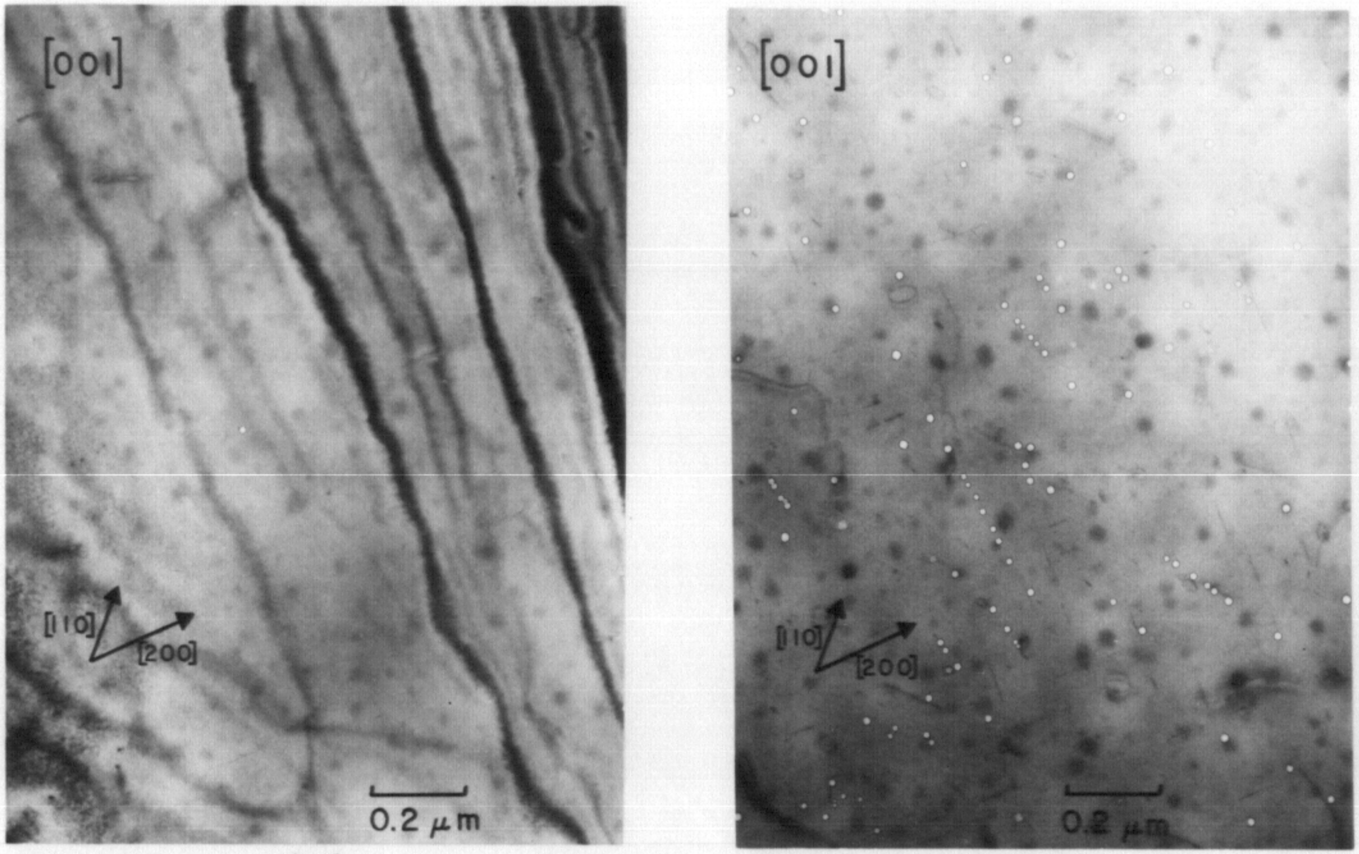

(a) Typical Of ~ 99 % Of Total Thin Area

(b) Typical Of ~ 1% Of Total Thin Area

FIGURE 39. Group II vanadium sample irradiated (as annealed) at 600°C to 2 dpa with 18 MeV copper ions.

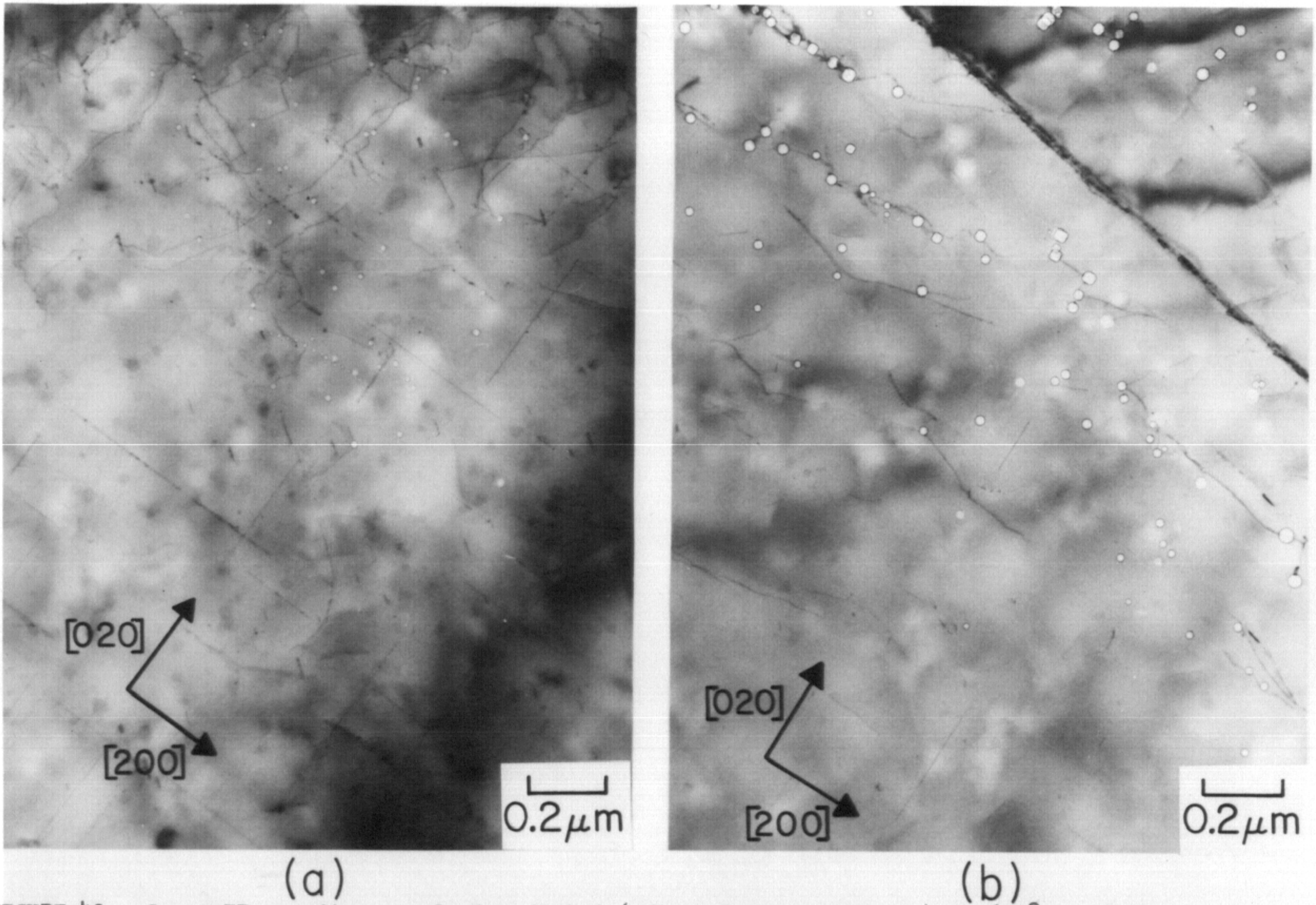

FIGURE 40. Group II vanadium sample irradiated (after electropolishing) at 600°C to 2 dpa.

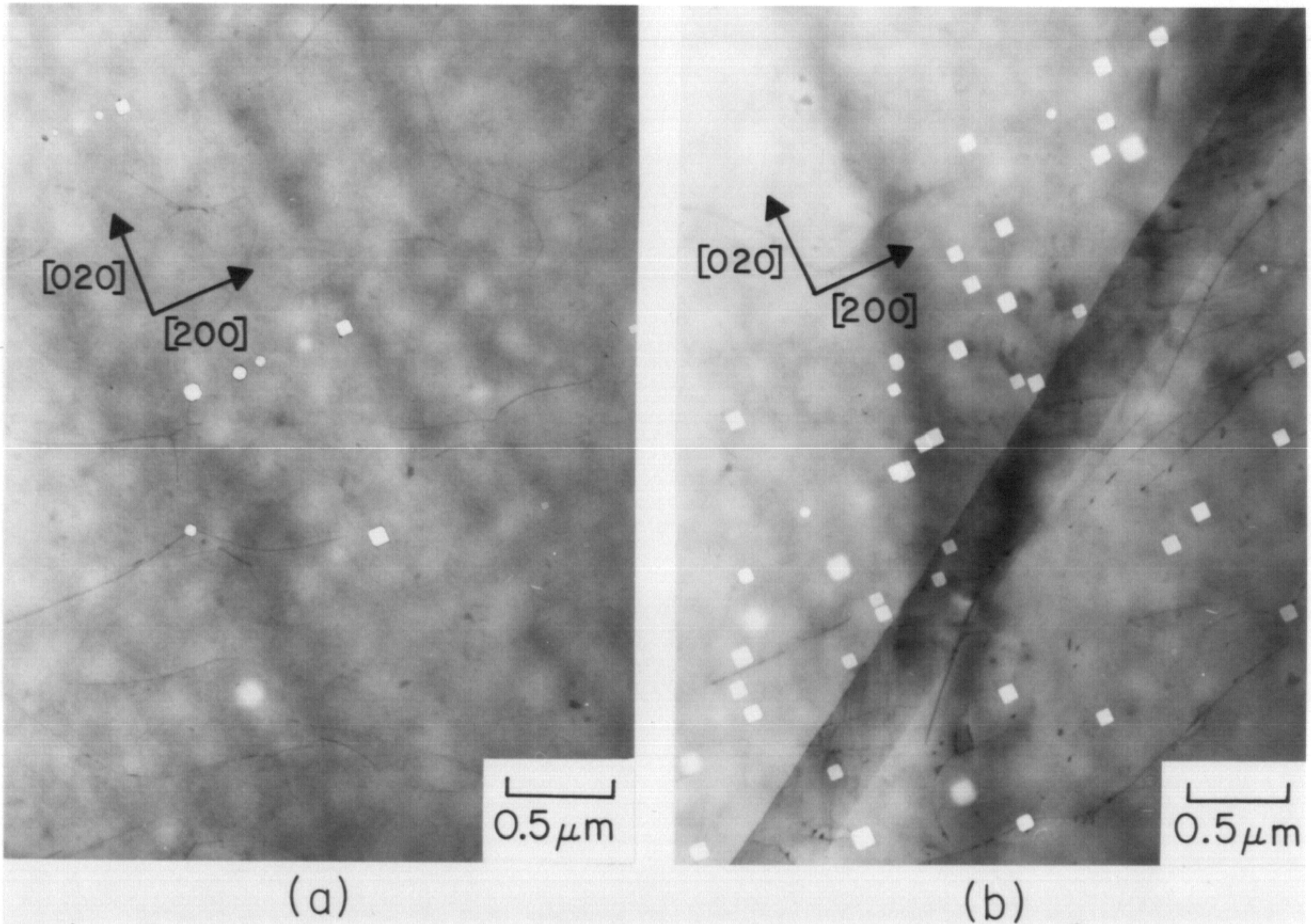

FIGURE 41. Vanadium sample of Group II irradiated, after electropolishing, at 650°C with 18 MeV copper ions to 2 dpa.

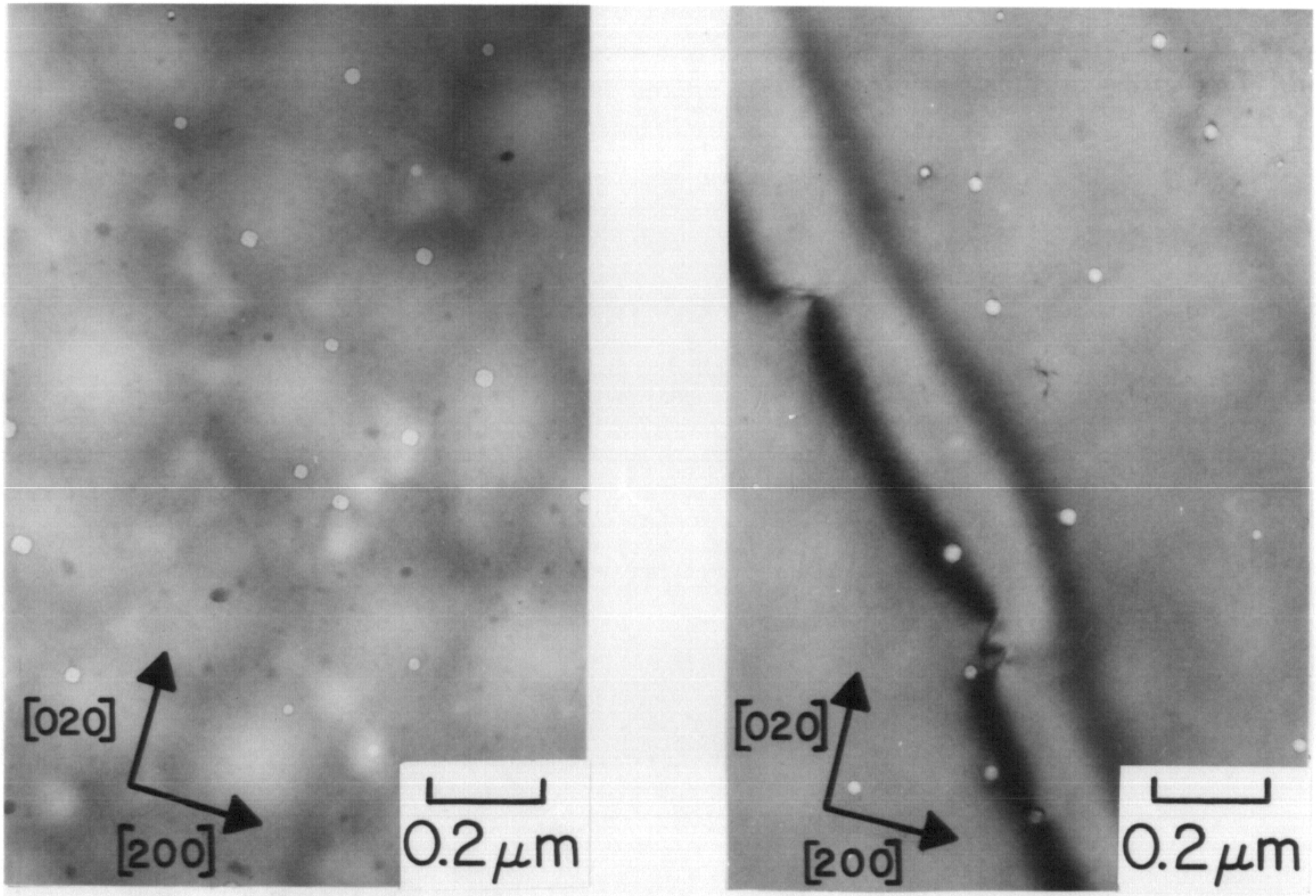

AS ANNEALED
(a)

ELECTROPOLISHED
(b)

FIGURE 42. Vanadium samples of Group II irradiated at 700°C with 18 MeV copper ions to 2 dpa.

irradiated as annealed; the sample of Figure 42b was irradiated after electropolishing. There was no significant difference observed in the microstructure of the two samples, thus indicating that no surface contamination is occurring during annealing and apparently no hydrogen (introduced by electropolishing) is retained after outgassing (in vacuum) to 750°C. No precipitates were observed in the samples irradiated at 700°C.

The void size in the above samples peaked at 650°C; however, the void size at 700°C was larger than at 600°C. The void density in the grain interiors increased with temperature. This is contrary to normal behavior where the void density usually decreases with temperature. This may indicate that nucleation has not been completed at these temperatures and damage level.

The dislocation structure observed in both samples irradiated at 600°C is similar. The dislocation structure at 600°C consisted mainly of a high density of dislocation loops. The typical loop structure observed at 600°C is shown in Figure 43. Fewer loops were observed at 650 and 700°C than at 600°C, and the loop size decreased at the higher temperature. The dislocation structure at 650°C is shown in Figure 44a; the dislocation structure typical of the samples irradiated at 700°C is shown in Figure 44b. Only in the samples irradiated at 600°C were the loops large enough and of sufficient density to analyze. This loop analysis will be discussed further in the following section.

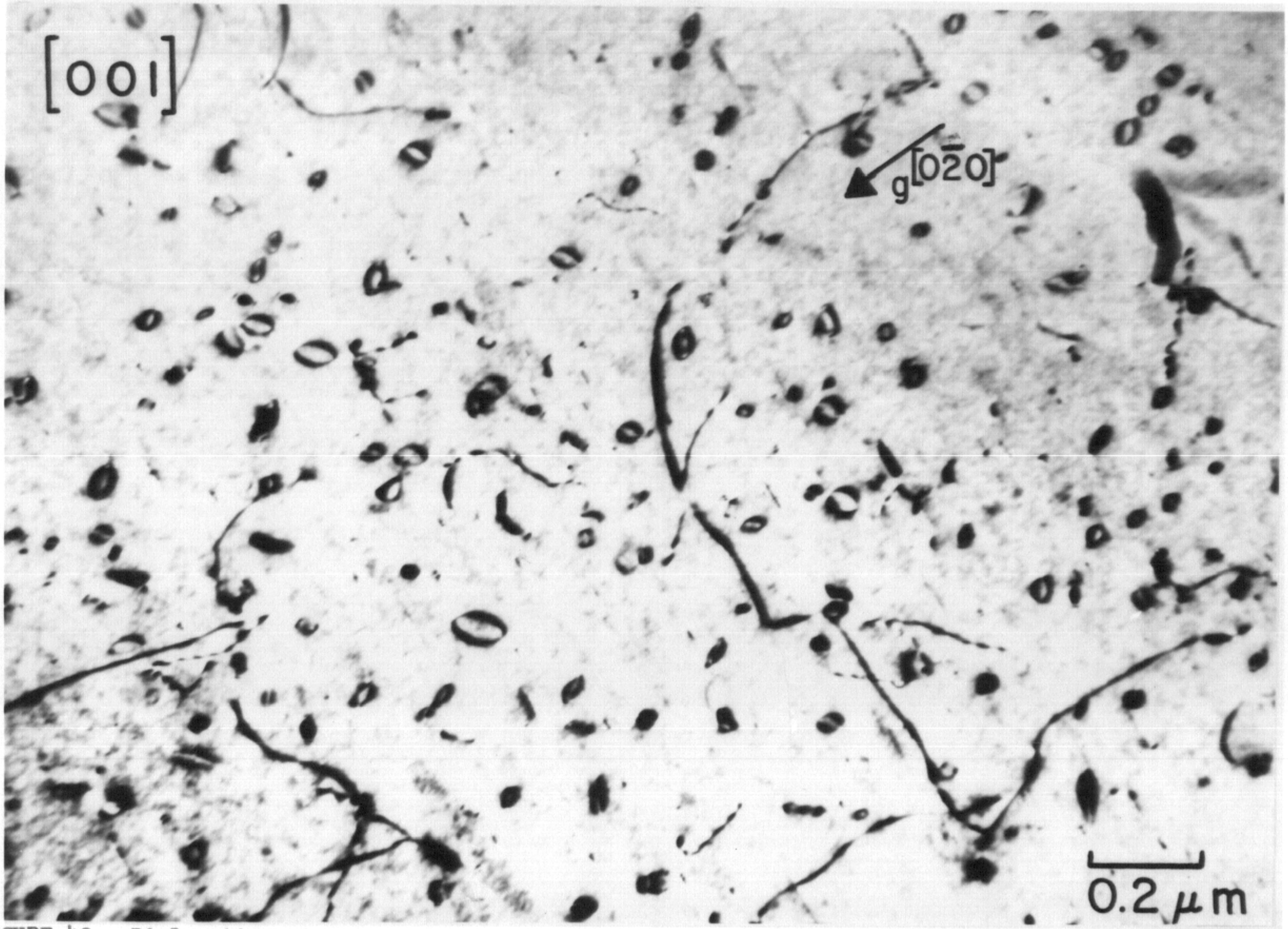

FIGURE 43. Dislocation structure in the vanadium sample of Group II irradiated at 600°C to 2 dpa.

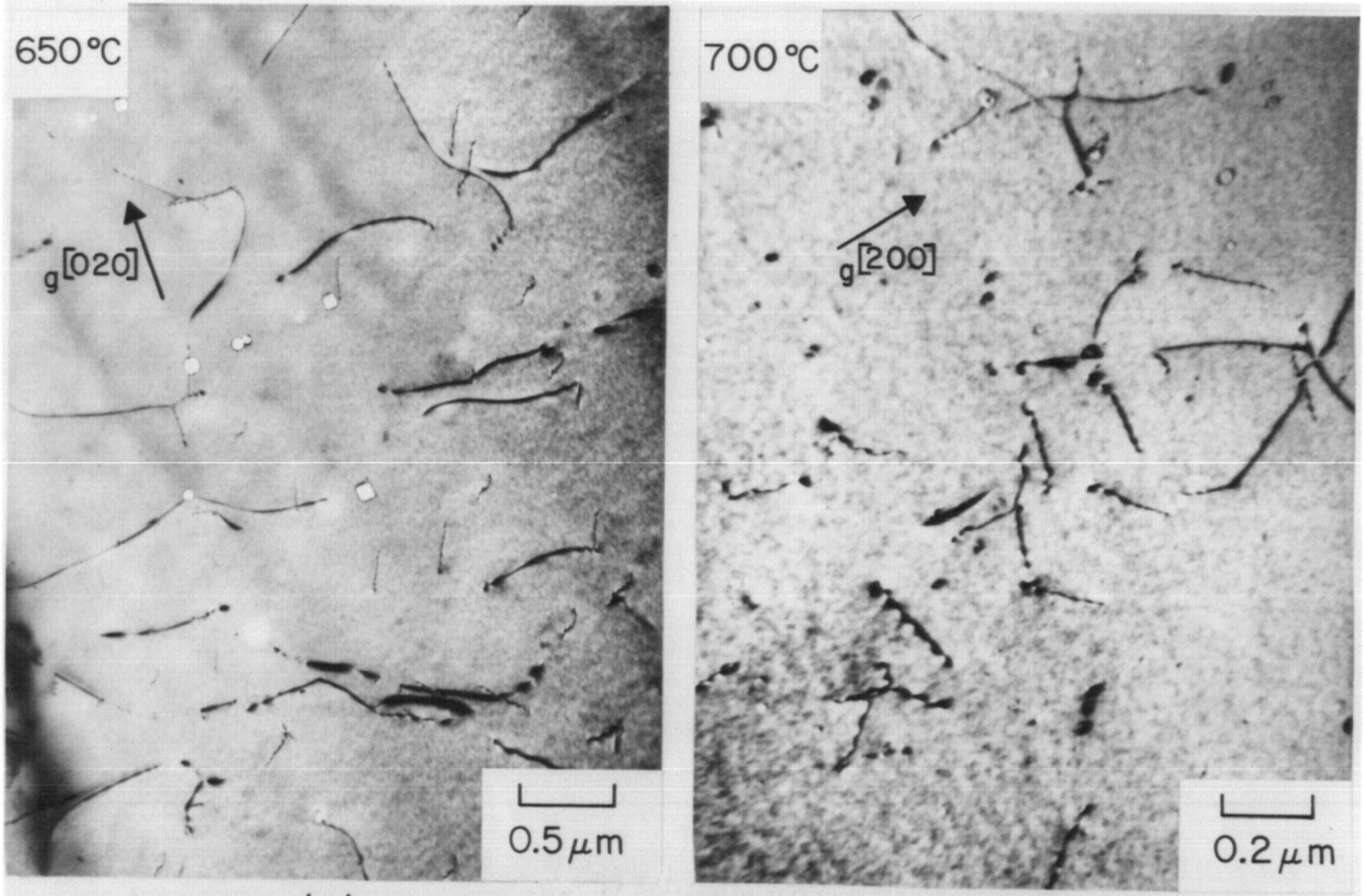

(a) (b)

FIGURE 44. Dislocations in vanadium samples of Group II irradiated at 650 and 700°C to 2 dpa.

In another series of irradiations (Runs 13 and 14) the vanadium samples were irradiated with 14 MeV copper ions over the temperature range from 150 to 850°C, and the damage was analyzed at a depth that corresponds to 1 dpa (4 dpa at 800 and 850°C). Although the samples of one irradiation (Run 13) were electropolished after annealing, they were degassed at 850°C to remove any hydrogen which may have been introduced by electropolishing; thus, the pre-irradiation state of the vanadium samples in Runs 13 and 14 should be identical. Black spot damage in the sample irradiated at 150°C and the void microstructure which develops at 200 and 350°C are shown in Figure 45. In the sample irradiated at 150°C (Figure 45a) it was not possible to determine, because of the very small size of the defect clusters, if the damage consisted of voids and loops or just loops. The void microstructure in the samples irradiated at 500, 600, 650, and 700°C is shown in Figure 46. No voids were observed at 800 and 850°C.

The voids in the above samples were found in large numbers throughout the grain interiors; however, in a sample irradiated at 550°C, voids in significant numbers were found only within about 1 micron of the grain boundaries. Some voids were observed in the grain interiors, but the number density was almost negligible. The microstructure in the sample irradiated at 550°C is shown in Figure 47. Besides the high density of voids observed along the grain boundaries, the microstructure in the sample irradiated at

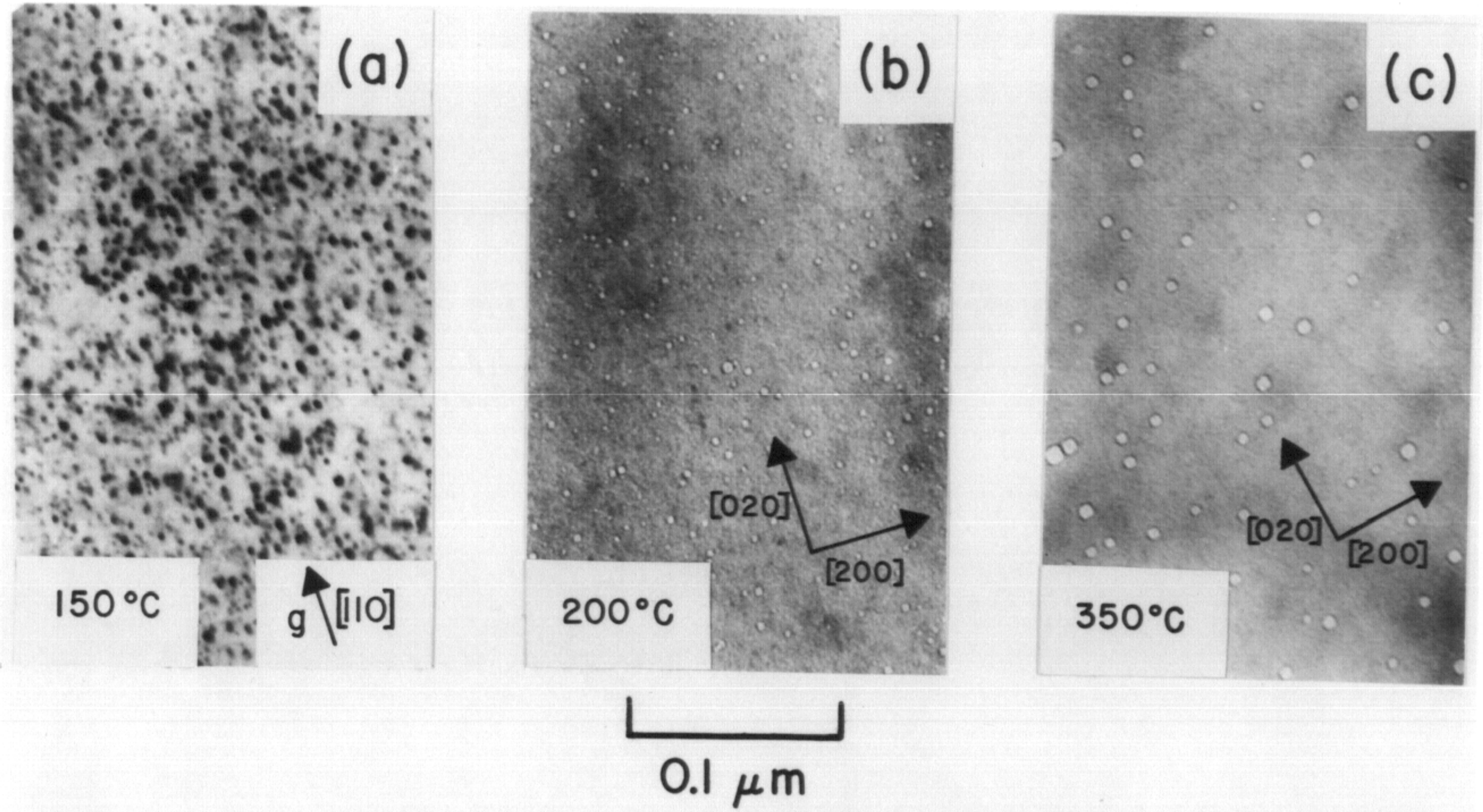

FIGURE 45. Black spot damage and voids in vanadium samples of Group II irradiated with 14 MeV copper ions to 1 dpa.

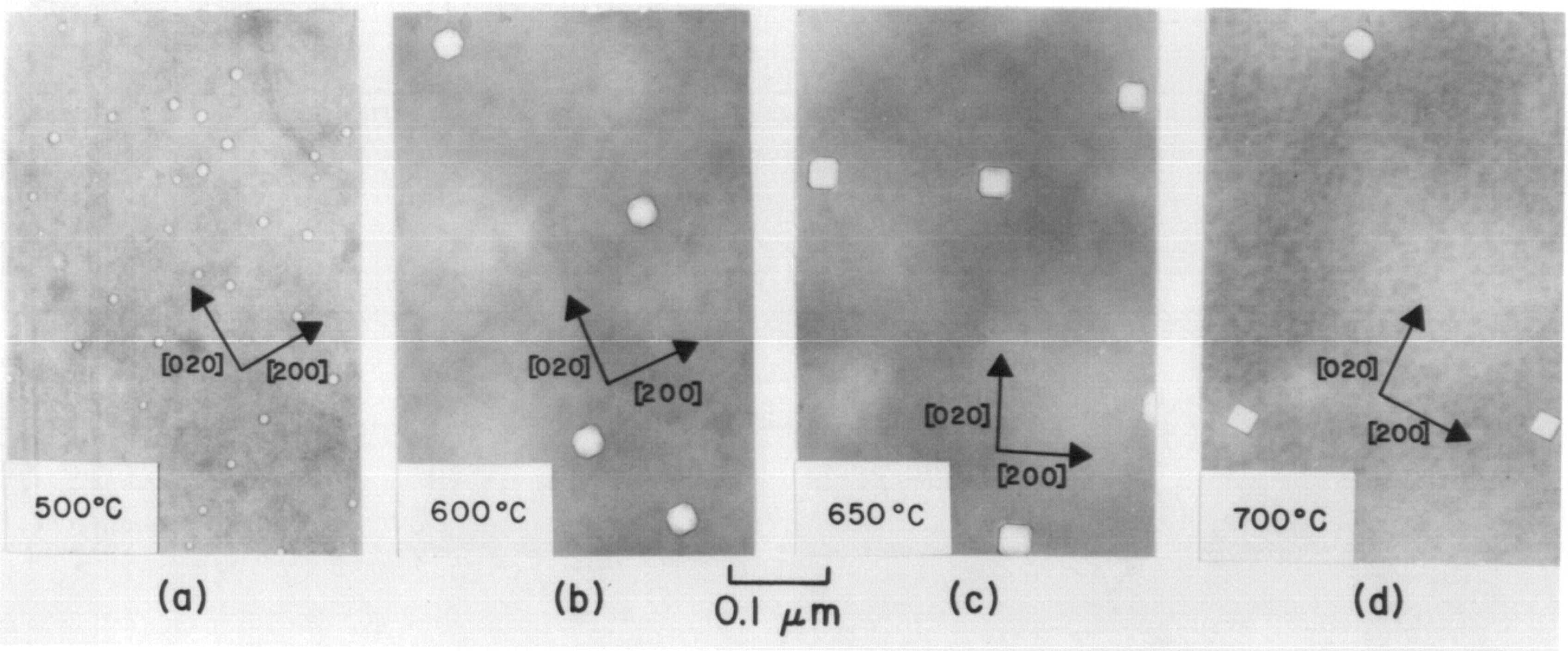

FIGURE 46. Voids in the vanadium samples of Group II irradiated with 14 MeV copper ions to 1 dpa.

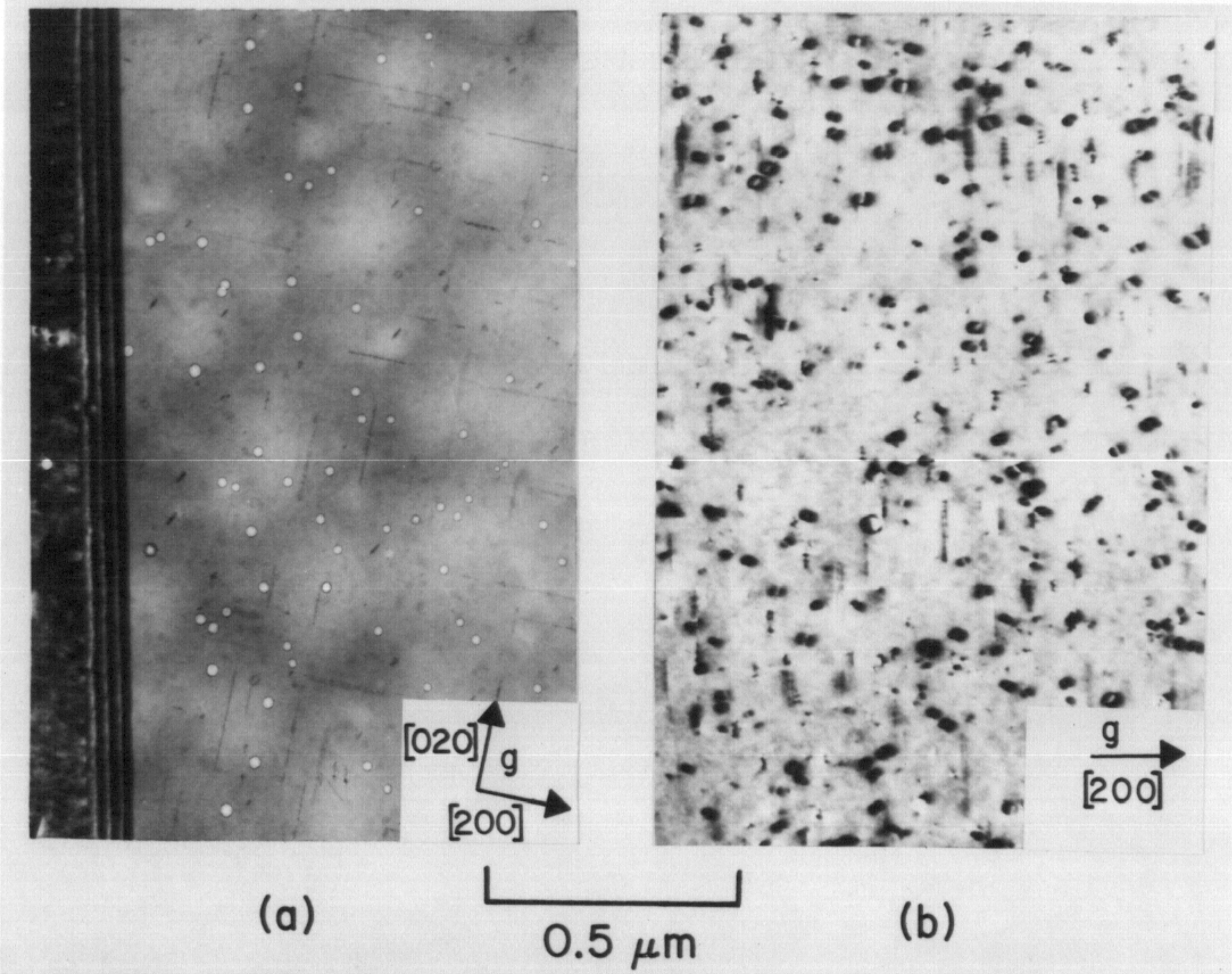

FIGURE 47. Microstructure in the vanadium sample of Group II irradiated at 550°C with 14 MeV Cu ions to 1 dpa. (a) **Voids near the grain boundaries**; (b) Loops and precipitates throughout the grains.

550°C also consisted of a high density of dislocation loops and rod-shaped precipitates throughout the grains (Figure 47b). The loop and precipitate densities were found to decrease near the grain boundaries where the voids were found.

A low density of rod-shaped precipitates was also found in the sample irradiated at 500°C. No precipitates were observed in any of the other irradiated samples of this set.

The void size increased with temperature, peaked at 650°C, and then decreased slightly at 700°C. The void density decreased with temperature over the entire temperature range from 200 to 700°C. The void size was always observed to increase near grain boundaries (if grain boundaries were present in the thin area); the void density usually decreased slightly near the grain boundaries. This effect of grain boundaries is well illustrated in Figure 48 for the vanadium sample irradiated at 500°C.

In the above samples irradiated at 600, 650, and 700°C, no measurable density of loops was found, and the dislocation density was very low (less than $2 \times 10^8/\mathrm{cm}^2$). The dislocation structure at 550°C has already been shown in Figure 47b and consisted of a high density of loops and a low density of network dislocations. The dislocation structure at 500°C contained a low density of loops and a low density of network dislocations; this dislocation structure at 500°C is shown in Figure 49. The dislocation structure at 200 and 350°C is shown in Figure 50; in these samples the

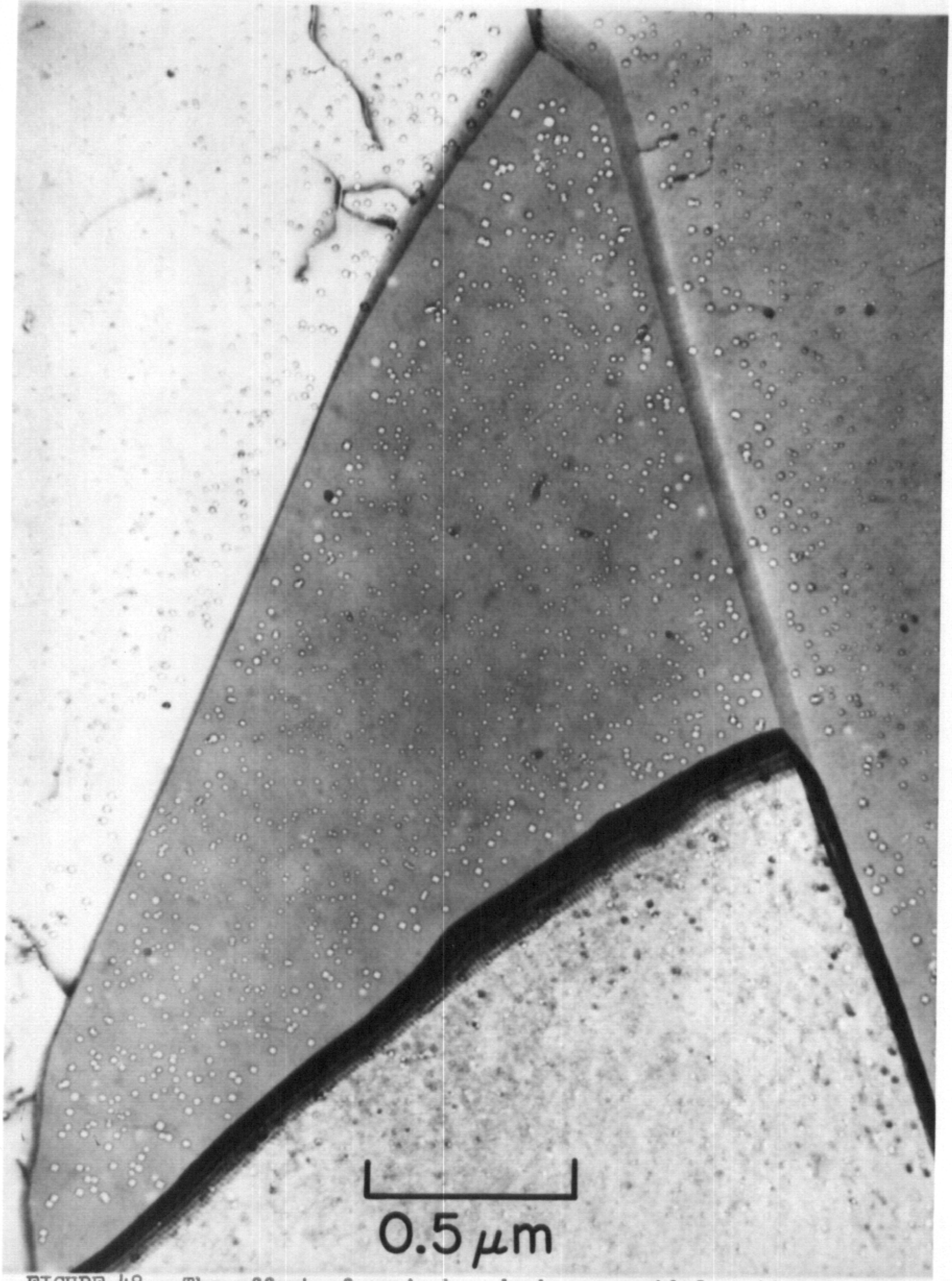

FIGURE 48. The effect of grain boundaries on void formation in the vanadium sample of Group II irradiated at 500°C to 1 dpa.

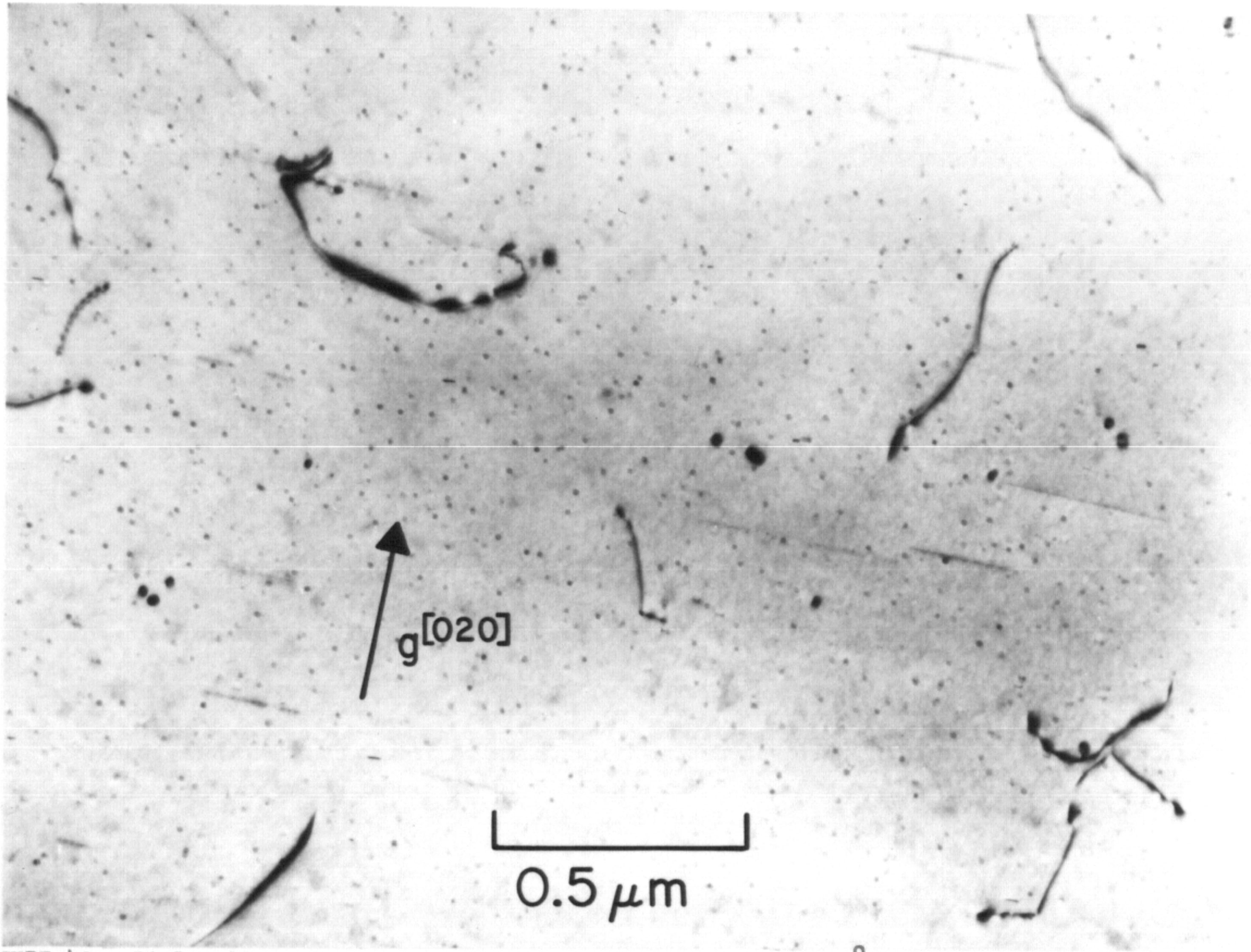

FIGURE 49. Dislocations in the vanadium sample irradiated at 500°C with 14 MeV Cu ions to 1 dpa.

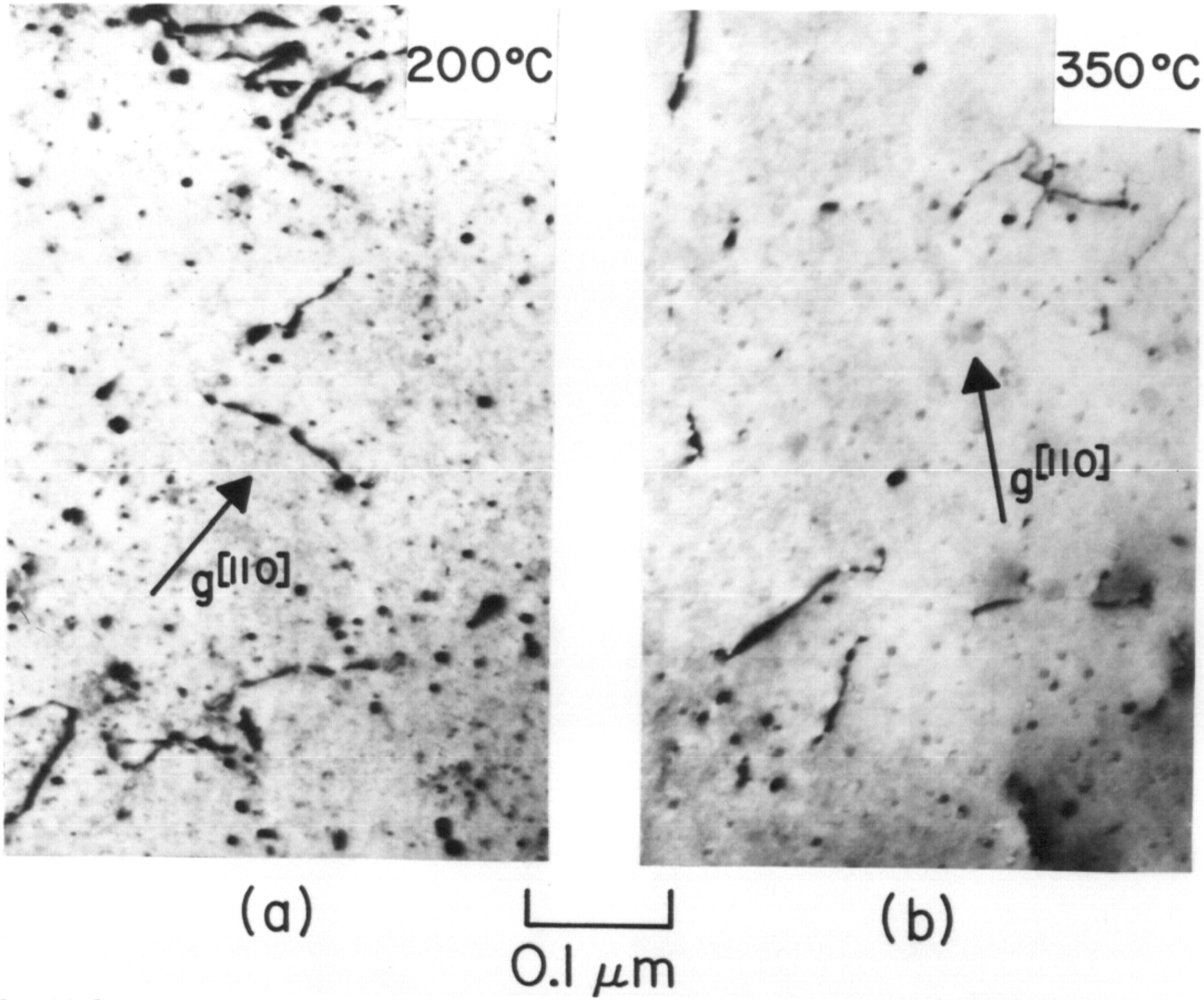

FIGURE 50. Dislocations in the vanadium samples of Group II irradiated with 14 MeV Cu ions to 1 dpa.

network dislocation density and the loop density were high ($10^{10}/cm^2$ and $10^{15}/cm^3$, respectively). The dislocation density at 150°C was very high and the loop density is assumed to be high (only a few of the black spots were resolvable as loops). The black spot damage at 150°C has already been shown in Figure 45a. In all the samples showing loops, the loops were too small (and in some cases too low in density) to analyze, with the exception that at 550°C a few of the larger loops were analyzed. (This analysis will be discussed in the following section on Geometrical Analysis.)

In addition to the above samples irradiated with 14 MeV copper ions to 1 dpa, one sample was also irradiated with 14 MeV copper ions at 700°C and examined in TEM at a depth corresponding to 0.2 dpa. No voids or loops were observed in this sample.

One final set of samples needs to be discussed. These samples (Run 12) were irradiated with 18 MeV copper ions at 500, 550, 600, 650°C and examined in TEM at a depth corresponding to 2 dpa. These samples were electropolished after annealing and outgassed in the tandem target chamber to 650°C before irradiation. This outgassing treatment was not sufficient to remove the hydrogen introduced by electropolishing. (This has recently been verified by Lott(144).) Thus, these particular samples contained an unknown amount of hydrogen. The void microstructure in these samples is shown in Figure 51. The void size increased with

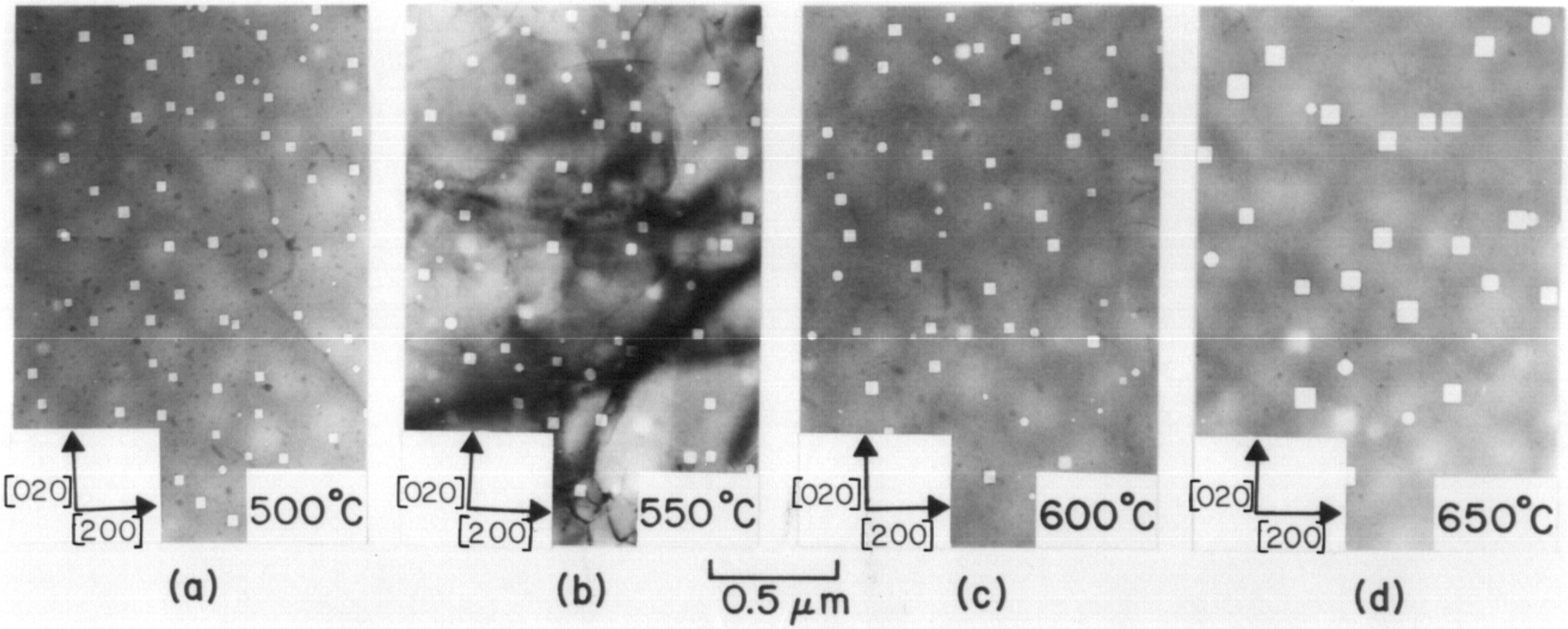

FIGURE 51. Voids in the vanadium samples of Group II containing hydrogen and irradiated with 18 MeV copper ions to 2 dpa.

temperature and the void density decreased. No measurable change in void size and density was observed near the grain boundaries in these samples; there was, as expected, a void denuded region immediately adjacent to the grain boundaries.

No precipitates were observed in these samples containing hydrogen. The network dislocation densities in all of these samples were very low (less than $5 \times 10^8/\mathrm{cm}^2$) and no measurable densities of dislocation loops were found.

Geometrical Analysis

The geometrical analysis of the irradiation produced defects is limited to the Group II samples since the double-tilt stage for the JEOL 100B electron microscope was not available during the analysis of the Group I samples. The geometrical analysis of the voids, dislocation loops, and the precipitates observed at 500, 550, and 600°C will now be presented.

The void images were examined in order to reach some conclusions regarding their shape. It was difficult to resolve faceting on the smallest voids, but as their diameter increased (greater than 60 Å) most voids were observed to exhibit some faceting and the larger voids (diameters greater than 150 Å) were distinctly faceted. The large voids were imaged at different crystallographic beam directions, such as in Figure 53; these images showed that the void faces formed on {100} and {110} planes (a small amount of faceting on {111} planes was also observed). The

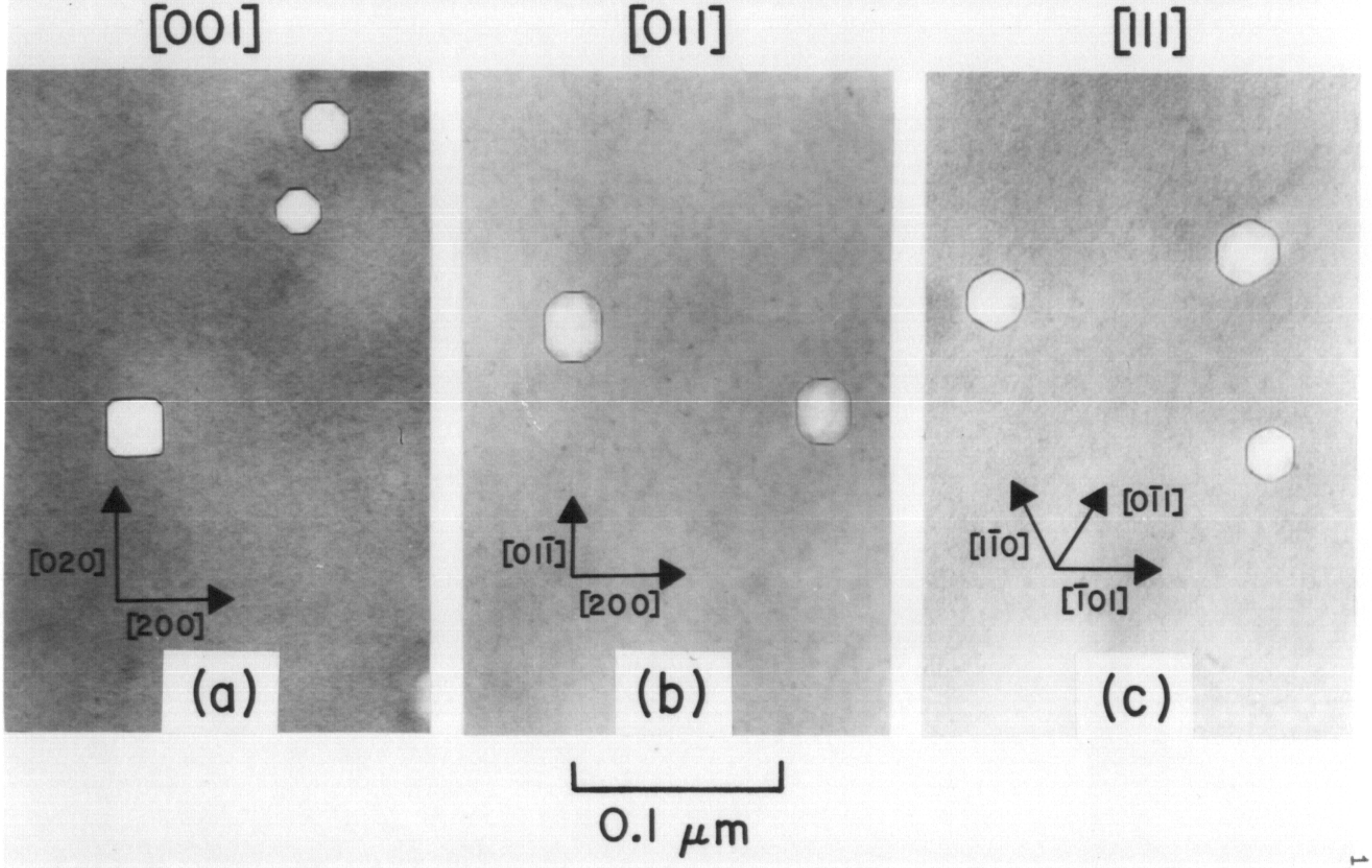

FIGURE 52. Void shapes in vanadium sample of Group II irradiated at 700°C to 2 dpa.

proportion of each type of face varied at all temperatures so that void shapes ranged from perfect {100} cubes to dodecahedra with {110} faces. At the larger void sizes the predominant void shape was the {100} cube truncated to different extents on {110} and {111} planes; however, a cube extensively truncated on {110} planes was indistinguishable from a dodecaedron truncated on {100} planes. Figure 53 illustrates some of these void shapes. It was not always possible to index the faces of the smaller voids, but in general the smaller voids also exhibited faceting on {100} and {110} planes.

The nature of large resolvable dislocation loops was determined using the procedure outlined in Chapter V. Only the samples irradiated at 600°C with 18 MeV copper ions to 2 dpa and the sample irradiated at 550°C with 14 MeV copper ions to 1 dpa met the criteria for loop analysis: flat foils and a high density of large loops. Several analyses were carried out in each sample. Micrographs selected from one such analysis in one sample irradiated at 600°C are shown in Figure 54. (It should be pointed out that micrographs were obtained with both + $\underline{g}$ and - $\underline{g}$ for all diffracting conditions; this served to check the self consistant nature of the loops.) The results of the contrast behavior of the 6 loops labeled in Figure 54 are summarized in Table 12.

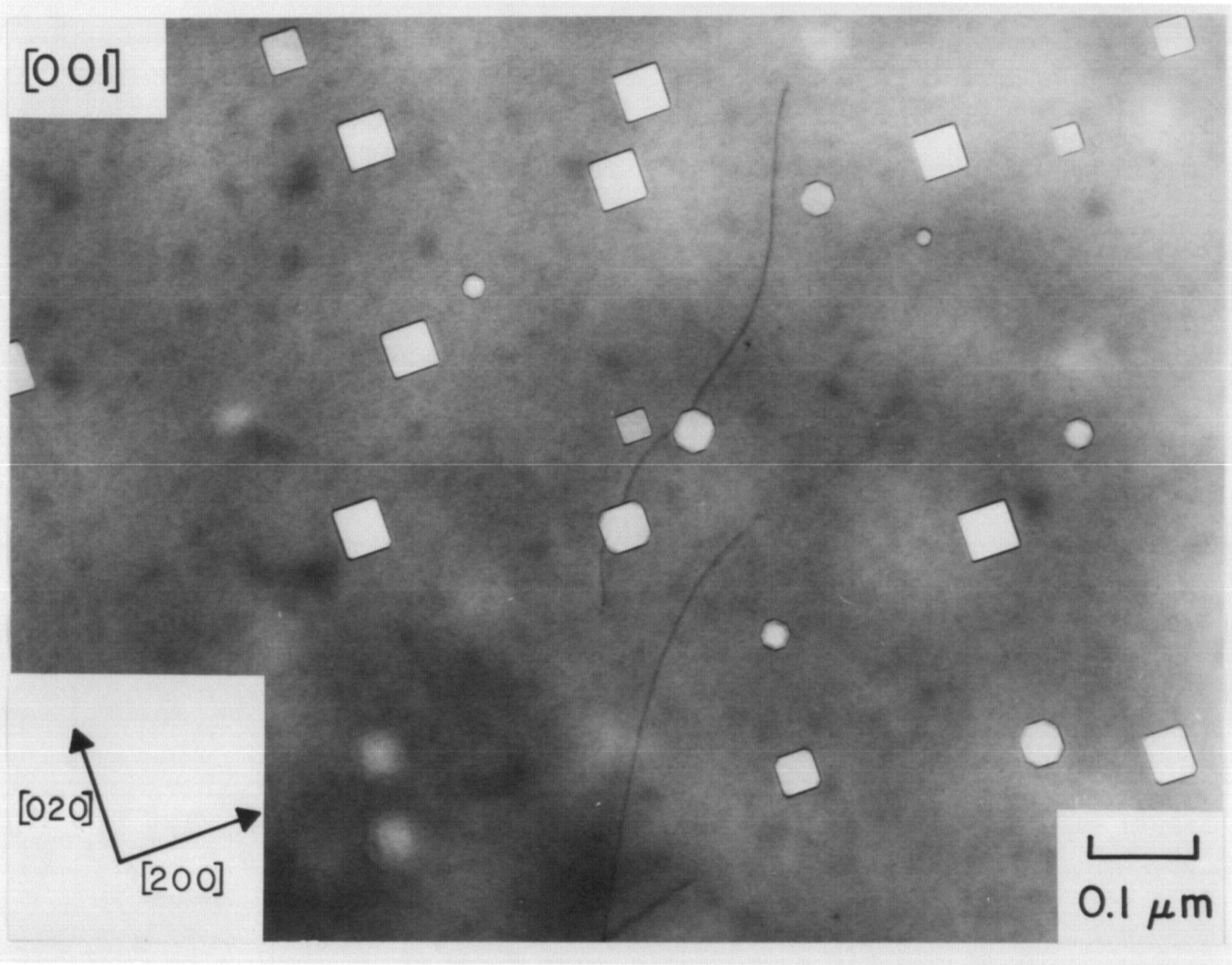

FIGURE 53. Void shapes in vanadium sample of Group II irradiated at 650°C to 2 dpa.

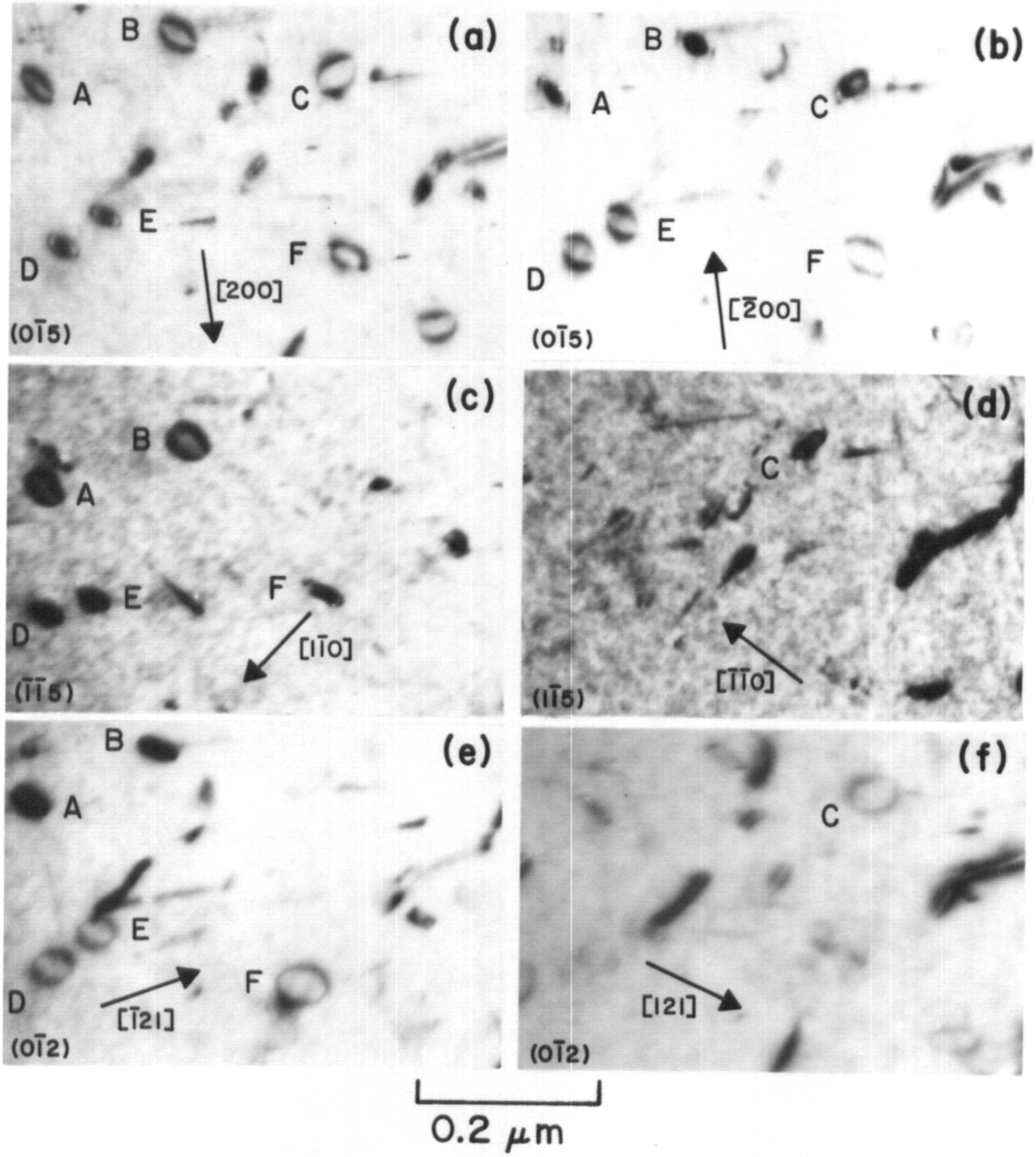

FIGURE 54. Dislocation loop analysis in vanadium irradiated at 600°C to 2 dpa. Summary of analysis is given in Table 12.

TABLE 12

SUMMARY OF CONTRAST BEHAVIOR OF LOOPS LABELED IN FIGURE 54

Loop $\underline{g}$	A and B	C	D, E, and F
200	outside	outside	inside
$\bar{2}00$	inside	inside	outside
$1\bar{1}0$	visible	residual	visible
$\bar{1}\bar{1}0$	residual	visible	residual
$\bar{1}21$	visible	residual	visible
121	residual	visible	residual
$\underline{b}$	a/2 $[1\bar{1}1]$	a/2 $[11\bar{1}]$	a/2 $[\bar{1}1\bar{1}]$
nature	interstitial	vacancy	vacancy

Both vacancy loops and interstitial loops were found at 550 and 600°C. At 600°C, the loop population was about equally divided between vacancy and interstitial loops. At 550°C only a small fraction of the loops were large enough to be analyzed; of the loops analyzed, about an equal number of vacancy and interstitial loops were identified. The statistics regarding the fraction of loops which were vacancy (or interstitial) in nature are very poor due to the low number of total loops analyzed (only a small region in each foil would meet the ideal conditions necessary for loop analysis). The results, however, do show that a large percentage of the loops are vacancy in nature.

The analyzed loops were found to lie on {110} planes and have Burgers vectors of a/2 ⟨111⟩ . The Burgers vectors of the dislocation line segments which form the network dislocations were also found to be mostly a/2 ⟨111⟩ (a few were found to be ⟨100⟩ types).

The rod-shaped precipitates were only observed at 500 and 550°C, in the samples irradiated with 14 MeV copper ions, and at 600°C in the samples (without hydrogen) irradiated with 18 MeV copper ions. The precipitates were found to be rods with their axis along one of the ⟨100⟩ directions. This is illustrated in the two micrographs of Figure 55. In the [001] orientation of Figure 55a the precipitates are only observed along the [020] and [200] directions; in the [111] orientation of Figure 55b, the rods

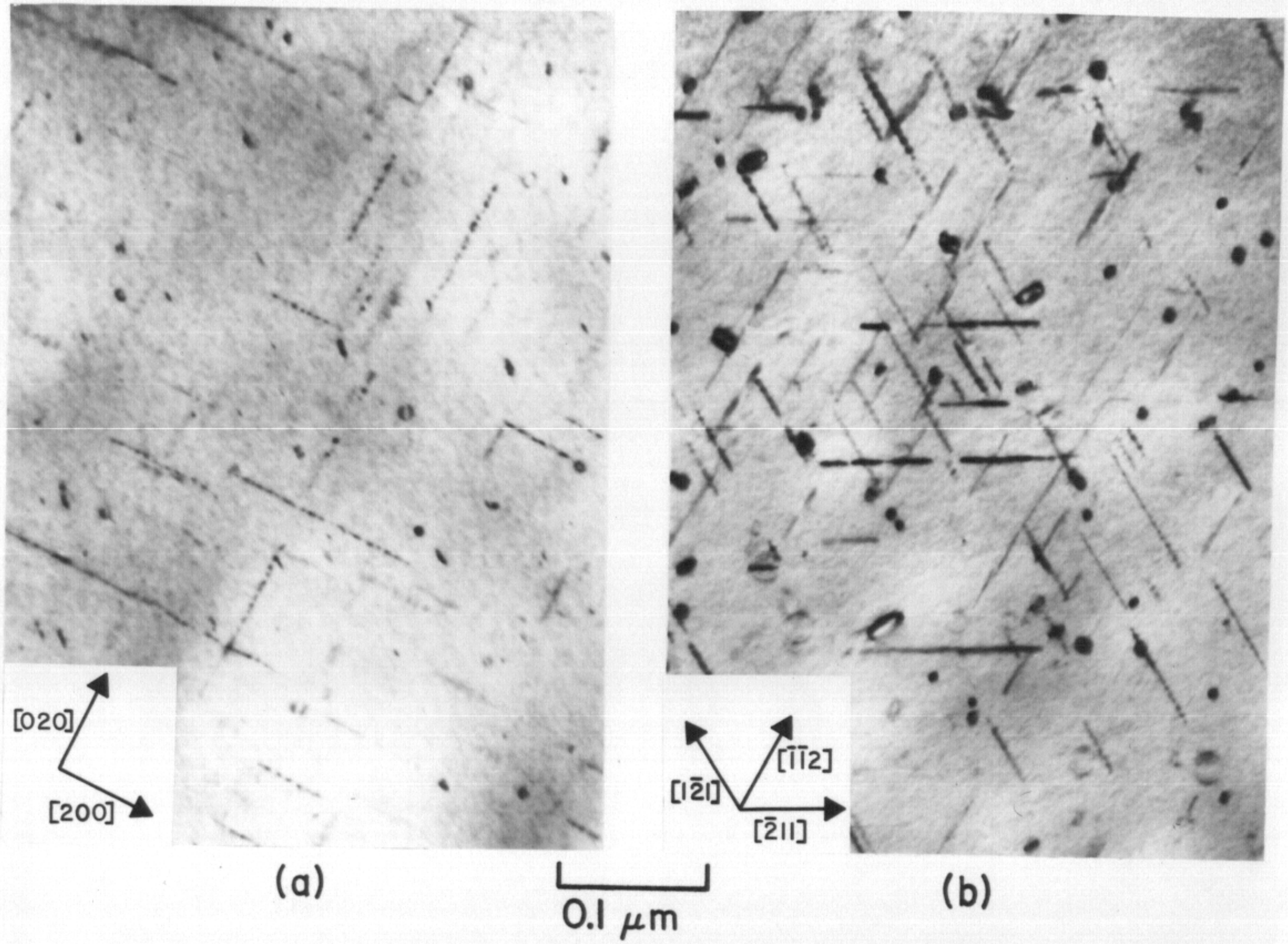

FIGURE 55. Precipitates along <100> directions in the vanadium sample of Group II irradiated at 550°C to 1 dpa.

are observed along the three <121> directions (the projections of <001> directions are along <121> in a [111] orientation). The nature and crystal structure of these precipitates has not been determined.

Quantitative Results

The quantitative data of the void microstructure in the vanadium samples of Group II are given in Table 13, for the samples irradiated with 18 MeV copper ions, and in Table 14, for the samples irradiated with 14 MeV copper ions. The average void size as a function of temperature is plotted in Figure 56. The average void size peaks at 650°C in all three sets of data plotted in Figure 56; at this peak (650°C) the void size increases with dose. The void size is also increased in those samples which contain hydrogen (introduced during electropolishing after annealing). In Figure 57 the void density is plotted as a function of temperature for those sets of samples which showed an uniform distribution of voids in the grain interiors (even if the density was very low). In general, the void density decreases with temperature; however, at temperatures between 500°C and 600°C the void density is suppressed in the vanadium samples irradiated with 14 MeV copper ions to 1 dpa. This decrease in the void density curve occurs in the same temperature region as the rod-shaped precipitation. In the samples containing hydrogen the void density is increased, and there appears to be no significant decrease in void density between

TABLE 13

SUMMARY OF VOID DATA FOR THE VANADIUM SAMPLES OF GROUP II IRRADIATED WITH 18 MeV COPPER IONS TO 2 dpa

Temperature	In the Grain Interiors				Adjacent to Grain Boundaries	
(^{o}C)	Average Void Size[a] (Å)	Volume Averaged Void Size[a] (Å)	Void Density (cm^{-3})	ΔV/V (%)	Average Void Size[a] (Å)	Void Density (cm^{-3})
600	106	112	10^{12} to 10^{14}	<0.01	-	-
600[b]	102	106	10^{12} to 10^{14}	<0.01	220	1.5×10^{14}
650[b]	600	653	9.0×10^{12}	0.24	925	1.6×10^{13}
700	201	218	5.4×10^{13}	0.04	302	6.0×10^{13}
700[b]	155	170	1.7×10^{14}	0.06	-	-
750	None Observed					
750[b]	None Observed					
500[c]	300	320	1.9×10^{14}	0.6	300	1.9×10^{14}
550[c]	315	345	1.7×10^{14}	0.7	315	1.7×10^{14}
600[c]	340	365	8.7×10^{13}	0.4	340	8.7×10^{13}
650[c]	678	705	4.1×10^{13}	1.44	-	-

a) Cube Edge
b) These samples were electropolished after annealing and then outgassed at 750°C in high vacuum.
c) These samples were electropolished after annealing and then outgassed at 650°C in high vacuum.

TABLE 14

SUMMARY OF VOID DATA FOR THE VANADIUM SAMPLES OF GROUP II IRRADIATED WITH 14 MeV COPPER IONS

Temperature (^{o}C)	dpa	In the Grain Interiors: Average Void Size (Å)	In the Grain Interiors: Volume Averaged Void Size (Å)	In the Grain Interiors: Void Density (cm^{-3})	In the Grain Interiors: $\Delta V/V$ (%)	Adjacent to Grain Boundaries: Average Void Size (Å)	Adjacent to Grain Boundaries: Void Density (cm^{-3})
150	1	Black Spot Damage ($2 \times 10^{17}/cm^{3}$)					
200	1	22[a]	23	5.0×10^{16}	0.03	-	-
350	1	32[a]	35	1.6×10^{16}	0.04	54	8.3×10^{15}
500	1	72[a]	76	1.4×10^{15}	0.03	137	1.0×10^{15}
550	1	100[a]	100	5.0×10^{12}	< 0.001	163	2.6×10^{14}
600	1	186[b]	187	5.9×10^{13}	0.02	328	2.8×10^{13}
650	1	332[b]	337	2.1×10^{13}	0.07	416	1.5×10^{13}
700	0.2	None Observed					
700	1	187[b]	201	1.5×10^{13}	0.01	476	2.1×10^{13}
800	4	None Observed					
850	4	None Observed					

a) Void Diameter.

b) Void Cube edge.

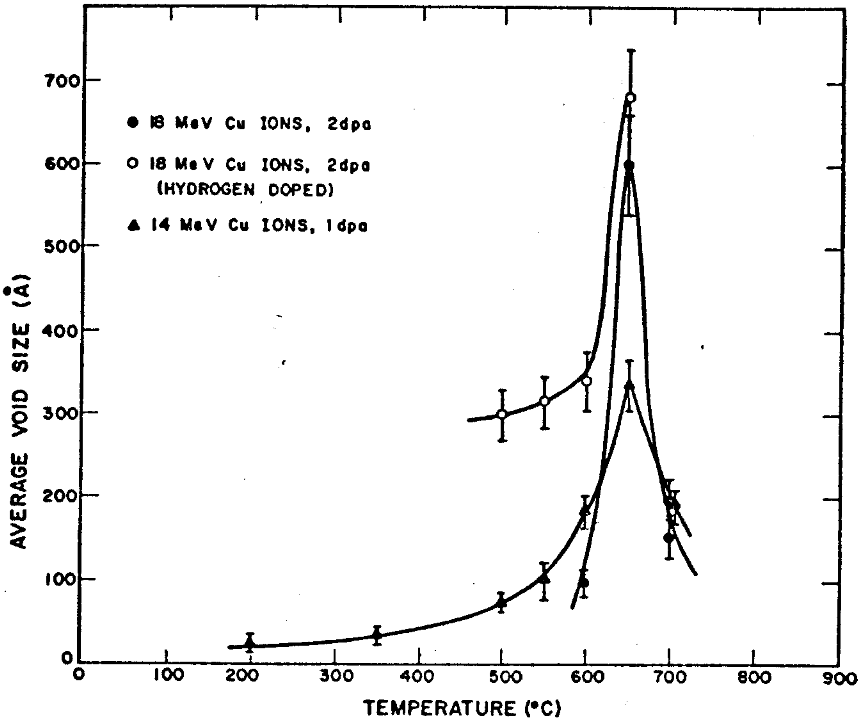

FIGURE 56. Average void size as a function of temperature for the vanadium samples of Group II.

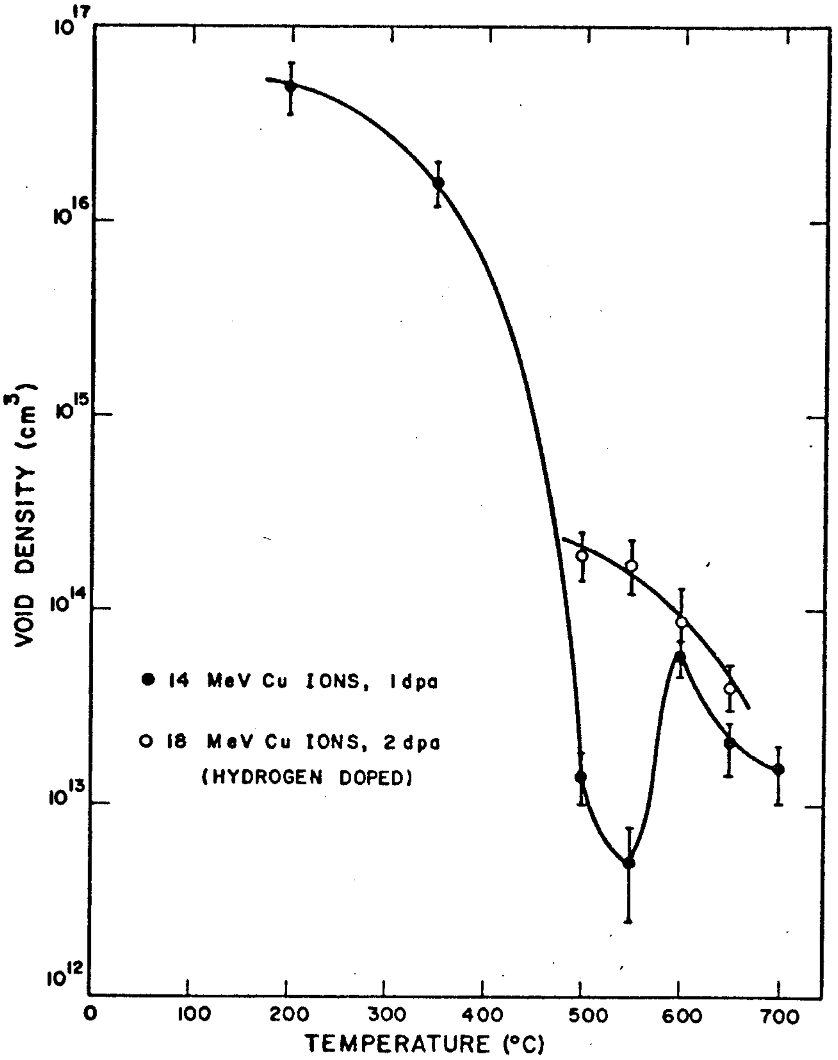

FIGURE 57. Void density as a function of temperature for the vanadium samples of Group II.

500°C and 600°C, as is observed in the samples that had been thoroughly outgassed (do not contain hydrogen). The void swelling as a function of temperature is shown in Figure 58, for the samples irradiated with 18 MeV copper ions to 2 dpa, and in Figure 59, for the samples irradiated with 14 MeV copper ions to 1 dpa. The maximum in the void swelling occurs at 650°C in both Figure 58 and Figure 59. As shown in Figure 58, the void swelling is dramatically increased in the samples containing hydrogen. The void swelling data in Figure 59 shows that, in addition to the swelling peak at 650°C, there is a broad low temperature peak between 200°C and 500°C. The minimum in the swelling curve, at 550°C, in Figure 59 occurs at the same temperature as the extensive rod-shaped precipitation.

The quantitative data of the dislocation structures in the samples of Group II are listed in Tables 15 and 16. In the samples irradiated with 18 MeV copper ions (Table 15), the average loop diameter and the loop density both decrease with temperature. In the samples irradiated with 14 MeV copper ions (Table 16), the average loop diameter increases with temperature and the loop density decreases with temperature. In Table 15 the network dislocation density is insensitive to temperature; in Table 16 the network dislocation density decreases with temperature to 600°C and increases slightly at 650 and 700°C.

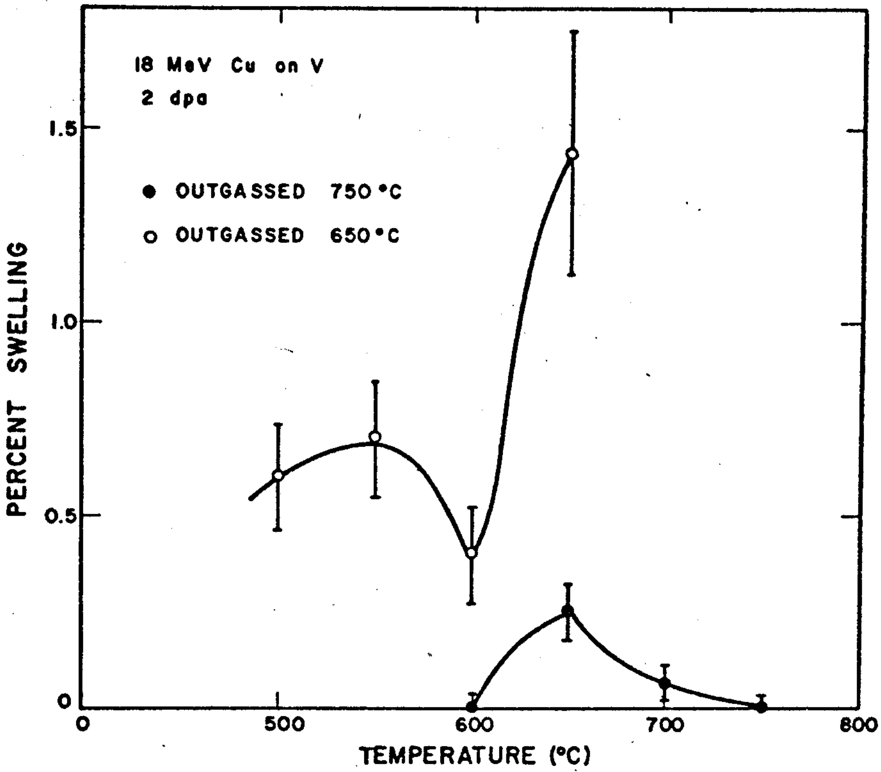

FIGURE 58. Void swelling as a function of temperature in the vanadium samples of Group II irradiated to 2 dpa. The samples outgassed to only 650°C contain hydrogen introduced during electropolishing.

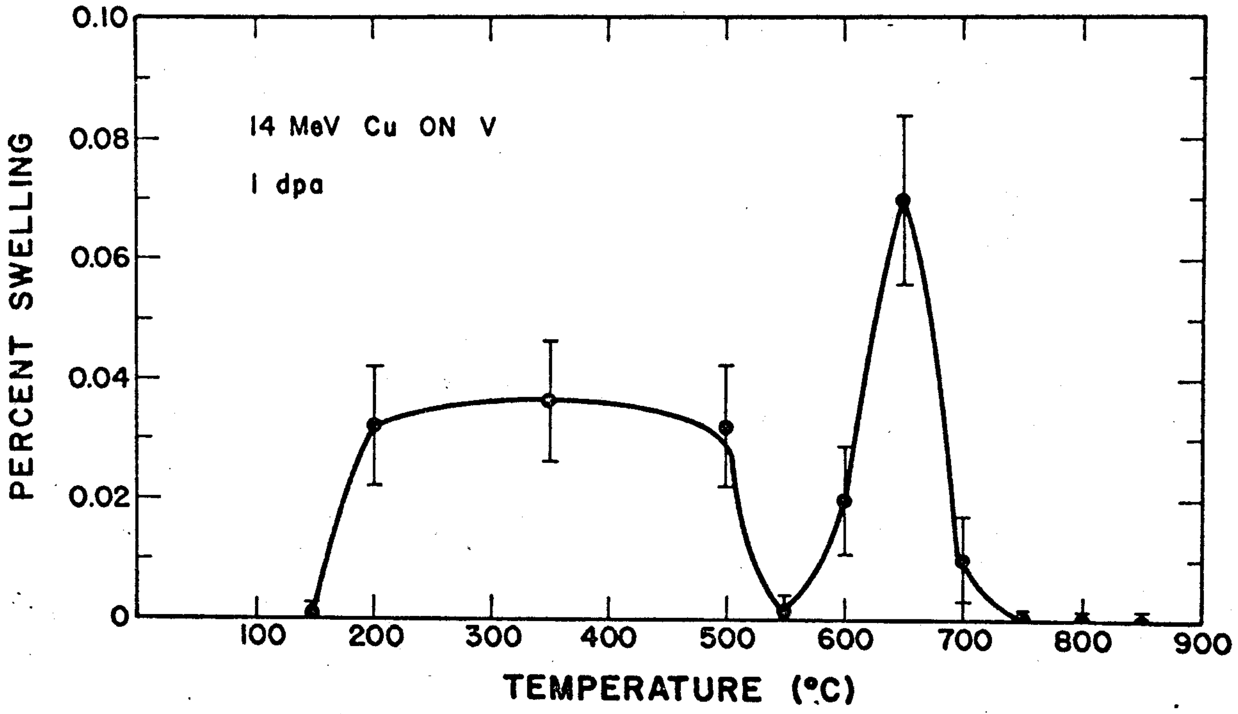

FIGURE 59. Void swelling as a function of temperature in the vanadium samples of Group II irradiated to 1 dpa. The samples were outgassed to temperatures $\geq 850^{\circ}$C before irradiation.

TABLE 15

SUMMARY OF THE DISLOCATION DATA FOR THE VANADIUM SAMPLES OF GROUP II IRRADIATED WITH 18 MeV COPPER IONS TO 2 dpa

Temperature (°C)	Average Loop Diameter (Å)	Loop Density (cm^{-3})	Network Dislocation Density (cm^{-2})
600	470	1.5×10^{14}	9×10^{8}
600[a]	430	1.0×10^{14}	7×10^{8}
650[a]	500	5.2×10^{13}	2×10^{9}
700	300	1.0×10^{13}	6×10^{8}
700[a]	290	2.7×10^{13}	8×10^{8}
750	None Observed		2×10^{8}
750[a]	None Observed		1×10^{8}
500[b]	None Observed		5×10^{8}
550[b]	None Observed		2×10^{8}
600[b]	None Observed		3×10^{8}
650[b]	None Observed		2×10^{8}

a) Electropolished after annealing, outgassed at 750°C.

b) Electropolished after annealing, outgassed at 650°C.

TABLE 16

SUMMARY OF THE DISLOCATION DATA FOR THE VANADIUM SAMPLES OF GROUP II IRRADIATED WITH 14 MeV COPPER IONS TO 1 dpa

Temperature (^oC)	Average Loop Diameter (Å)	Loop Density (cm^{-3})	Network Dislocation Density (cm^{-2})
150	Black Spot Damage ($2 \times 10^{17}/cm^3$)		
200	80	6×10^{15}	1×10^{10}
350	80	1×10^{15}	2×10^{10}
500	150	2×10^{13}	2×10^{8}
550	163	4×10^{14}	9×10^{7}
600	None Observed		7×10^{7}
650	None Observed		2×10^{8}
700	None Observed		3×10^{8}

The quantitative data for the rod-shaped precipitates found in the Group II samples are listed in Table 17. The average precipitate length increases with temperature and the precipitate density peaks at 550°C. (No precipitates were observed in the samples containing hydrogen).

TABLE 17

SUMMARY OF THE DATA FOR THE ROD-SHAPED PRECIPITATES IN THE VANADIUM SAMPLES OF GROUP II

Temperature (°C)	dpa	Damage Rate (dpa/sec)	Precipitate Density (cm^{-3})	Average Precipitate Length (Å)
500[a]	1	2×10^{-4}	4×10^{13}	1000
550[a]	1	2×10^{-4}	8×10^{14}	2000
600[b]	2	1×10^{-4}	8×10^{13}	5000
600[b]	2	1×10^{-4}	1×10^{14}	5000

a) Irradiated with 14 MeV copper ions (thoroughly outgassed).

b) Irradiated with 18 MeV copper ions (thoroughly outgassed).

CHAPTER VII

DISCUSSION

Introduction

In this chapter the results presented in Chapter VI will be discussed. It would be difficult to give a fully comprehensive account of the complex behavior observed in the damage structures; therefore, only those aspects which are considered to be significant will be discussed. Due to the role precipitation has on the void and dislocation substructures, the precipitates observed in the samples of Group I and Group II will be discussed first. In the second section the void microstructures observed in the irradiated vanadium will be discussed. In the final section the dislocation substructures will be considered.

Precipitate Structures

Group I

The most significant feature observed in the samples of Group I was the presence of a high density of large precipitates. The results presented in Chapter VI indicate that the precipitation was due to contamination of the vanadium during the high temperature anneals in the tandem target chamber. The results also indicate that the precipitation was not due to interstitial impurities (carbon, oxygen, or nitrogen), but was the result of nickel contamination. The most likely source of the nickel, in the target chamber used in this study, is the chromel-alumel (nickel-based) thermocouples used to monitor the temperature of the samples. The high vapor pressure of nickel, 1.2 x 10^{-6} Torr at 1000°C(145), supports this view; however, the vapor pressure of nickel in chromel or alumel may not necessarily be exactly this value. Although the large precipitates of the Group I samples are known to contain nickel, the exact composition of the precipitates remains unknown. The phase diagram of the vanadium nickel system(146,147) indicates that the equilibrium solubility limit for nickel in vanadium is approximately 5% at temperatures below 750°C. Above the solubility limit the Beta phase, V_3Ni, forms; and at nickel concentrations exceeding about 27%, the Sigma phase, VNi, forms. Neither of these phases match the crystal structure suggested by the diffraction pattern in Figure 31b, and it is hard to imagine the average nickel concentration exceeding more than a few percent in the damage region, even though irradiation induced segregation could result in locally high nickel concentrations. Therefore, based on the electron diffraction data and the V-Ni equilibrium phase diagram, the large precipitates observed in the vanadium samples of Group I must be a metastable phase in the V-Ni system which forms a partially coherent structure under irradiation.

Two other types of precipitates were observed in the samples of Group I. In the samples electropolished after annealing a high density of smaller precipitates was found. It was not possible to obtain crystallographic information or energy dispersive x-rays analysis of this type of precipitate; however, this precipitate type formed at the same temperature as did the larger nickel-bearing precipitates and was not observed in the samples of Group II, thus, indicating that it may also be due to the same nickel contamination. These small precipitates were associated with the void microstructure, as shown in Figure 25 where a precipitate is observed on or near most voids. It is almost impossible to say which came first, the voids or the precipitates; however, the presence of a single precipitate at only one end of the elongated voids (see Figure 25b) suggests that perhaps the voids nucleated on the precipitates. If, on the other hand, the precipitates had nucleated on the ends of such elongated voids, one might expect precipitates to be found at both ends. This was not observed; in fact every elongated void observed had only one precipitate associated with it.

The third type of precipitate found in the samples of Group I is the ⟨100⟩ rod-shaped precipitate observed in the samples irradiated at 600°C. These rod-shaped precipitates were also too small for crystallographic analysis, using TEM, or for energy dispersive x-ray analysis. This precipitate type is similar in geometry and forms in the same temperature range as the precipitates observed in the samples of Group II which are discussed next.

Group II

The large nickel-bearing precipitates and the smaller void-associated precipitates discussed above were not found in the samples of Group II, thus, indicating a significant reduction or elimination of the nickel contamination through use of the new high vacuum annealing furnace. In this new furnace the samples were exposed to a high temperature environment for only a short period of time (about 1 hour) as compared to the long exposure times (about 96 hours) required in the tandem target chamber. In addition, the chromel-alumel thermocouples (a possible source of the nickel) were less likely to contaminate the vanadium in the new furnace, since the thermocouples were no longer in direct contact with the vanadium samples and any nickel from the thermocouples would more likely to condense on the cooler surfaces surrounding the samples (in the tandem target chamber heater, the samples were the coolest surface near the thermocouples). As a result of this study, the chromel-alumel thermocouples have been removed from the annealing furnace to prevent any possibility of nickel contamination in future studies.

The only precipitates found in the samples of Group II were rod-shaped precipitates, with their axis along one of the $\langle 100 \rangle$ directions. These precipitates were observed in several samples of Group II irradiated at 500, 550, and 600°C and are similar to the rod-shaped precipitates observed in the samples of Group I irradiated at 600^{o}C. However, this precipitate type was not found in those samples of Group II which contained hydrogen and which were irradiated under similar conditions. As already mentioned above these precipitates were too small for crystallographic or compositional analysis.

These rod-shaped precipitates may be the result of interstitial impurities (C, O, or N) segregating and precipitating during irradiation. Although the precipitate density is fairly high, the average volume of a rod-shaped precipitate is small; furthermore, if the precipitate phase is a vanadium rich phase, the total amount of impurities contained in the precipitates could be accounted for by a small impurity concentration, on the order of 100 wt-ppm (the amount of interstitial impurities present in the as-received material). Agarwal et al.(109,110) have found that a metastable vanadium-carbide precipitate (plate-like) forms in their high purity vanadium during irradiation (see discussion in Chapter IV). They observed this behavior only in samples irradiated at temperatures between 550 and 700^{o}C. They also observed that the precipitation increases with dose, suggesting that further contamination from the residual gas may be occurring during irradiation and/or that further irradiation results in the segregation of the impurities, still in solution, to the precipitates. It is not proposed, because of the difference in morphology, that the rod-shaped precipitates of this study are the same phase as those observed by

Agarwal et al. (It may not even be a carbide); however, there are interesting similarities in the temperature range over which the precipitates form. The fact that the damage rate is an order of magnitude higher in the irradiations of Agarwal et al. than in the irradiations of this study may also have some bearing on the precipitate phase which forms. This is an area that needs further investigation in the future.

Another aspect of the rod-shaped precipitation that needs to be considered is the absence of such precipitation in those samples which are believed to contain hydrogen introduced by electropolishing (discussed in the following section). These samples were irradiated under similar conditions and at the same temperatures as those samples in which precipitation did occur. One possible explanation for this behavior is that hydrogen enhances the void nucleation rate (discussed in the following section), thus allowing a high density of voids, which were observed, to form. The high density of voids resulted in a significant change in the defect sink structure and strength; as a result, the impurities probably segregated to the voids. Therefore, instead of forming precipitates, the impurities were distributed among a high density of voids, effectively reducing the impurity concentration in the matrix below the "solubility" limit. Another explanation for the absence of the rod-shaped precipitates in these samples is that the hydrogen is trapped at the impurities, thereby effectively pinning the impurities and inhibiting the precipitation reaction. This is an area that needs further investigation to clearly define the role of hydrogen in both void formation and precipitation.

Void Microstructures

The void microstructure observed in the vanadium samples of this study are a complex function of temperature, impurity concentrations (which varied with preparation techniques), and the precipitate structure which sometimes developed as a result of sample contamination. This complex behavior of the void microstructure can be explained in a qualitative sense using the ideas and theories presented in Chapter III; however, detailed quantitative analysis of the observed void microstructures is not possible, within the framework of existing theories, at this time.

Before proceeding on to the discussion of the void microstructures in the samples of Group I and Group II, it is important to emphasize that the data from this study does not fall into a clearly defined nucleation or growth regime. As mentioned in Chapter II, most theories and equations governing void formation have assumed that nucleation is a separate process that precedes void growth. The low doses used in this study places this data in that regime where nucleation of new voids may still be occurring in parallel with the growth of existing voids; this will have some bearing on the interpretation of the results discussed below.

Group I

The void microstructures which formed in the irradiated samples of Group I were generally a simple function of temperature. As expected, the void size increased with temperature (Figure 34) and the void density decreased with temperature (Figure 35). The void size and void density were also affected by the electropolishing of the samples after annealing and prior to irradiation. The effect of the electropolishing was to decrease the void size and increase the void density. This effect could be the result of hydrogen introduced during electropolishing, the change in nickel content (introduced during annealing) by the electropolishing, or the change in the precipitate structure (one result of the reduced nickel content). The first possibility is not very likely based on the results for the samples of Group II which showed that hydrogen introduced during electropolishing has little effect, if any, on the void microstructure if the samples are outgassed at temperatures of 750°C or more (this will be discussed more fully below). The second and third possibilities are directly related, and one or both are the most likely reason for the observed changes in the void microstructure. The void nucleation rate may be increased as a result of the reduced impurity content because of an increase in vacancy supersaturation due to the absence of the impurities which act as trapping sites. The change in the precipitate structure may also increase the vacancy supersaturation (and hence nucleation rate) by the absence of the large precipitates which act as trapping sites; the change in the precipitate structure to a high density of smaller precipitates may also serve to increase the number of heterogeneous nucleation sites. Since the voids in the electropolished samples were clearly associated with the small precipitates, the latter possibility, an increase in the number of heterogeneous nucleation sites, is probably the dominant mechanism for the increase in the void density. The increase in void density results in a decrease in void growth rate which accounts for the observed decrease in void size.

Another void microstructural feature observed in the samples of Group I are the void walls, such as the one shown in Figure 27, observed in several samples of Group I. The void walls are similar to void walls observed by Stiegler et al.[148,149] in neutron irradiated aluminum. They accounted for this by postulating that the wall of voids mark the position of a prior grain boundary that had been swept away during annealing and that the voids then nucleate on impurities that remain. There was some evidence for grain boundary migration in the vanadium samples of Group I to support this hypothesis.

Group II

The void microstructure which developed in the vanadium samples of Group II is somewhat different from that observed in the samples of Group I. No void walls or rod-shaped voids were found;

and, in general, the voids are smaller than in the samples of Group I. The void behavior is a rather complex function of temperature in the samples of Group II. The void size is an increasing function of temperature until it peaks at 650°C. This abnormal behavior has also been observed in vanadium by Agarwal et al.(109). The most complex behavior is the sharp decrease in void density and the minimum in the swelling curve which both occur in the same temperature range where the rod-shaped precipitates are found.

The minimum in the swelling curve is a direct result of the decrease in void density. The shape of the high temperature peak in the swelling curves of Group II are similar to the swelling curve determined by the group at Argonne(109). Their normalized results are shown in Figure 60 along with the normalized swelling curve of Figure 59. In both curves there is a sharp decrease in the swelling on the low temperature side of the peak. It is important to point out that precipitation was observed at temperatures below the peak swelling temperature in both sets of samples represented in Figure 60. In Figure 61 the amount of precipitation and the swelling as a function of temperature for the samples of Group II is shown. Clearly, the precipitation is directly responsible for the complex behavior observed in these results. There are two possible mechanisms for the observed decrease in void density and the resulting decrease in swelling. They are:

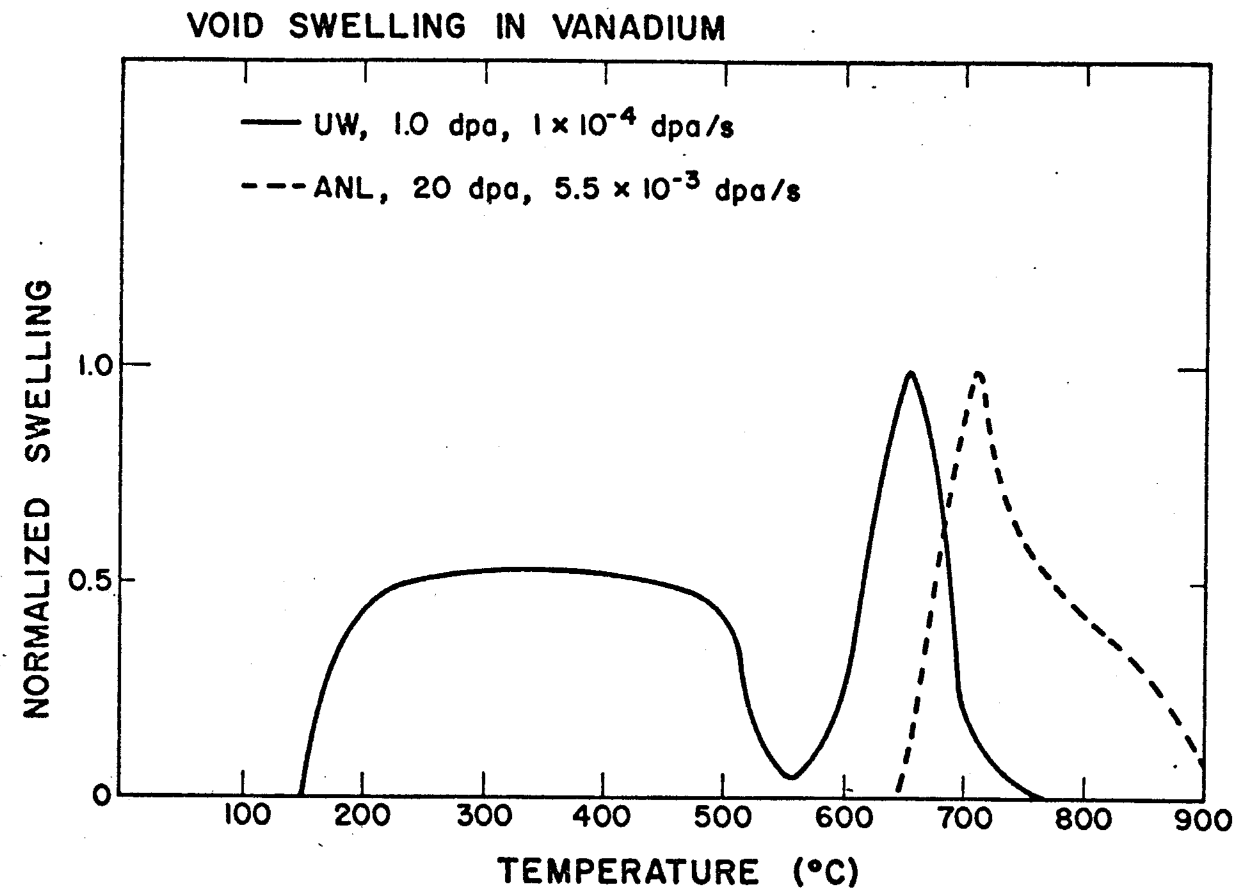

FIGURE 60. A comparison of the void swelling results from this study with the results obtained by Agarwal et al.(109) at Argonne National Laboratory (ANL).

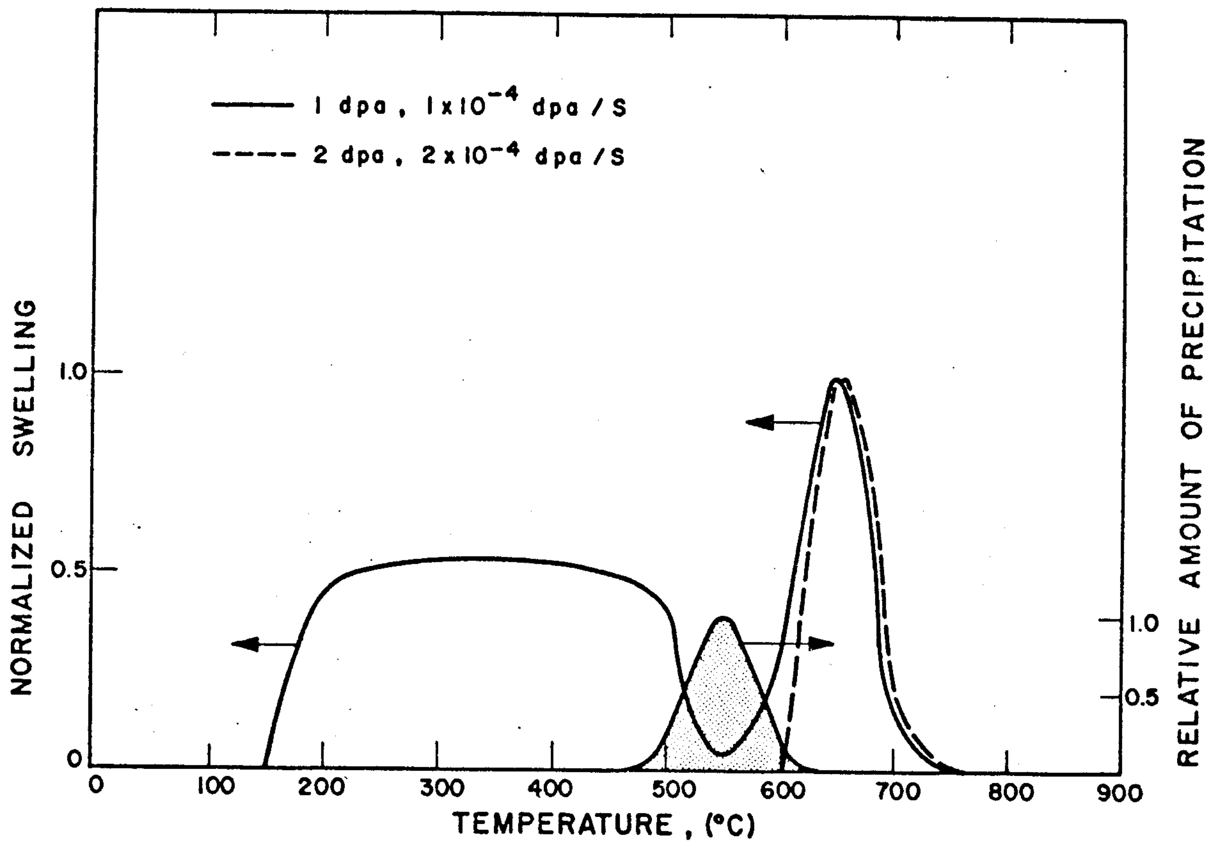

FIGURE 61. Void swelling and relative amount of precipitation as a function of temperature in the vanadium samples of Group II. The curve for the relative precipitation is purely qualitative.

1) The removal, through irradiation induced precipitation, of surface active impurities necessary for void stability.
2) A significant reduction in the void nucleation rate as a result of the precipitates which change the effective sink strengths and/or act as defect trapping sites.

The fact that large vacancy loops are observed in this temperature region suggests that the removal of necessary impurities from solution is the controlling mechanism. However, since these irradiations have been carried out at low doses, higher dose irradiations may result in significantly increased void densities. If this occurred, it would suggest that the nucleation rate had been reduced by the precipitation. Clearly this is an area that needs further investigation.

The voids in the vanadium samples of Group II occur over a wide temperature range, from 200°C (0.22 T_m) to 700°C (0.45 T_m). This is the first study to observe voids in heavy-ion irradiated vanadium at temperatures as low as 200°C and is in agreement with the work of Elen(88) who reported voids in vanadium irradiated at 150°C with neutrons. The high temperature cutoff in these samples may be misleading due to the low dose these samples received. Much higher doses may be necessary to nucleate an observerable density of voids, since nucleation rate is a decreasing function of temperature.

Samples of Group II which were electropolished after annealing and then outgassed at temperatures exceeding 750°C had void microstructures similar in nature to the void microstructures observed in samples which had not been electropolished. On the other hand, the void density and void size was significantly higher in those samples of Group II which were only outgassed to 650°C after electropolishing. This behavior is easily explained by the presence of hydrogen (introduced during electropolishing) in those samples outgassed at 650°C, and no hydrogen (or greatly reduced concentrations of hydrogen) in those samples outgassed at temperatures exceeding 750°C.

Hydrogen is known to diffuse into most metals during electropolishing, the induced hydrogen concentration being dependent on temperature and the particular solution used. In this study hydrogen diffuses into vanadium during electropolishing (at -20°C) in a solution of 20% H_2SO_4 and 80% methyl alcohol. If the temperature of the electropolished samples is increased the hydrogen concentration will be reduced as the hydrogen diffuse out of the samples. The results of this study show that outgassing at 650°C is insufficient to remove all the hydrogen; however, if the samples are outgassed at temperatures exceeding 750°C, the effects of induced hydrogen are eliminated or significantly reduced.

In the samples outgassed at 650°C prior to irradiation, the hydrogen which remained in the samples enhanced the void nucleation. (Hydrogen, introduced by electropolishing, has also been observed to enhance void nucleation in HVEM irradiated nickel-based alloys(150).) Hydrogen may enhance void nucleation by acting as a surface active solute to reduce the surface energy. Hydrogen may also form H_2 or H_2O gas molecules within the voids and, thus, further reducing the free energy of the voids.

Dislocation Substructure

Group I

The behavior of the dislocation substructures in the samples of Group I are very complex. The large precipitates which formed in the samples of Group I, irradiated as annealed, are responsible for the majority of the dislocation damage observed. It is not possible to distinguish between dislocations introduced by the precipitates and dislocations which formed as loops from the condensation of interstitials and vacancies.

Group II

The dislocation substructures in the samples of Group II also show a complex behavior. In general, the dislocation loop density decreases with temperature as expected. The temperature dependence of the loop diameter is not clear. At the lower temperatures the loop diameter increases with temperature, but at temperatures of 600°C or higher the loop diameter is either not a simple function of temperature or the loop population is simply nonexistent. The network dislocation density, which is not easily measured, also shows little temperature dependence. An interesting feature of the dislocation loop structure found in the samples of Group II is the identification of vacancy loops in several samples.

The loop nature was only determined at two temperatures and in samples which also showed extensive precipitation. The loop population in these samples was found to consist of about equal numbers of vacancy and interstitial loops. The presence of the vacancy loops is surprising in view of present theories on loop growth which show that if vacancy loops do nucleate they must shrink because of the preferential attraction of all dislocations for interstitials. In view of the fact that vacancy loops of large diameter were found in this investigation, the vacancy loops observed either grew from small vacancy loops or formed from the collapse of unstable voids. The latter conclusion is very unlikely (voids must overcome an energy barrier in order to collapse); therefore, the vacancy loops must have been nucleated (or formed during cascade collapse) and their growth favored by the presence of the precipitates or impurities in the vanadium. The precipitates could have an exceedingly high bias for interstitials which would leave a large excess of vacancies for vacancy loop growth, particularly since voids are present in extremely low numbers. The other possibility is that impurities in the vanadium reduce the bias of the vacancy loops for interstitials (by relieving the stress field of a vacancy loop) and allow the vacancy loops to grow.

There is insufficient data from this study to draw a firm conclusion about the effect of impurities on vacancy loop formation.

CHAPTER VIII

CONCLUSIONS

The results of this investigation lead to the following conclusions:

1) Voids form from 200°C to 700°C in high purity vanadium irradiated to 1 and 2 dpa at 1×10^{-4} dpa/s. Black spot damage was found at 150°C and no voids were observed in samples irradiated at 750, 800, and 850°C.

2) The temperature dependent void swelling curve exhibits a double peak for high purity vanadium irradiated to 1 dpa at 10^{-4} dpa/s. The maximum in the void swelling occurs at 650°C and a broad low temperature peak occurs between 200 and 500°C. The minimum between the swelling peaks occurs at 550°C.

3) At the minimum between the swelling peaks, a high density of dislocation loops and rod-shaped precipitates form in the absence of voids, which are found in significant numbers only near grain boundaries. The dislocation loop population consists of about an equal number of vacancy and interstitial loops

which lie on {110} planes and have a Burgers vector of a/2 <111> . The rod-shaped precipitates, with their axis along one of the <100> directions, are believed to be responsible for suppressing void formation.

4) Hydrogen, which may be introduced into high purity vanadium by electropolishing after annealing and before irradiation, enhances void nucleation; however, the hydrogen is effectively removed if the samples are outgassed in a vacuum at temperatures exceeding 750°C.

5) The surfaces of high purity vanadium, which is annealed under high vacuum ($<5 \times 10^{-8}$ Torr) at 1050°C in the presence of chromel-alumel thermocouples, may become contaminated with nickel.

6) In vanadium samples contaminated with nickel, a metastable, partially coherent phase of the V-Ni system forms during irradiation. The nickel impurities and possibly the precipitates enhance void swelling in these contaminated samples. The average void size in these samples increased with temperature and the void density decreased with

temperature. The maximum swelling occurred at $700^{o}C$ for 3×10^{-4} dpa/s.

7) Future studies should:
   a) Irradiate vanadium to higher damage levels in order to further study void growth kinetics and insure that void nucleation has ceased.
   b) Use electropolishing to dope vanadium with a known concentration of hydrogen and study in detail the effects of hydrogen on void nucleation.
   c) Examine the damage structures in vanadium as a function of depth from the irradiated surface in order to investigate the effects of PKA spectra, free surface, deposited ions, damage rate, and irradiation enhanced diffusion on those damage structures.
   d) Investigate in more detail the temperature region from 500 to $600^{o}C$ to determine the mechanism of vacancy loop formation and growth, the nature of the rod-shaped precipitates, and their role in suppressing void formation.
   e) Irradiate vanadium with high energy vanadium ions to eliminate any possible impurity effects from the bombarding ion species.

APPENDIX A

THE NUMBER OF DISPLACEMENT PER PKA

Probably the most widely known model for determining the number of displacement, $\nu(T)$, produced by a PKA of energy T is the Kinchin and Pease model(151). Their results are

$$
\begin{aligned}
\nu(T) &= 0 && \text{for } T < E_d \\
\nu(T) &= 1 && \text{for } E_d \leq T \leq 2E_d \\
\nu(T) &= T/2E_d && \text{for } 2E_d \leq T \leq E_c \\
\nu(T) &= E_c/2E_d && \text{for } T \geq E_c
\end{aligned}
\qquad \text{(A-1)}
$$

where E_d is the displacement energy (defined in Chapter II) and E_c is the critical energy above which all energy is lost by electronic excitation and below which all energy is lost in collisions producing displacements. This model ignores the possibility of replacement collisions and does not take into account the energy E_d lost each time a displacement is produced. The treatments of Seitz and Harrison(152) and Synder and Neufeld(153) account for this energy loss, and another model of Neufeld and Snyder(154) considers the effect of replacement collisions. The overall results, however, do not differ substantially from the Kinchin and Pease model and will not be discussed further.

The models discussed above assume that electronic losses occur only above E_c and nuclear losses occur only below E_c. This assumption of a sharp cutoff for electronic and nuclear losses is not realistic, particularly when working in the intermediate energy range of radiation damage where electronic and nuclear losses are of comparable magnitude. In light of these considerations, a task force(155) recommended the following expressions for $\nu(T)$:

$$\begin{aligned} \nu(T) &= 0 && \text{for } T < E_d \\ \nu(T) &= 1 && \text{for } E_d \leq T \leq 2E_d \\ \nu(T) &= \beta(T-E_e)/2E_d && \text{for } T > 2E_d \end{aligned} \qquad \text{(A-2)}$$

where E_e is the energy eventually dissipated by electronic collisions and β is a constant that is believed to slowly decrease with increasing T. Torrens and Robinson(156) have found β to be approximately 0.8.

Lindhard and coworkers(157) have derived an approximate expression for the fraction of the total energy dissipated which is given to recoiling atoms. This fraction is often referred to as the damage efficiency, and the result may be expressed as follows:

$$\frac{(T - E_e)}{T} = \frac{1}{1 + kg(\varepsilon)} \qquad \text{(A-3)}$$

where k is a constant in the Lindhard theory, ε is Lindhard's dimensionless measure of energy, and $g(\varepsilon)$ is a function numerically calculated by Lindhard. Robinson(158) has derived the following approximate expression for $g(\varepsilon)$:

$$g(\varepsilon) = 3.4008\varepsilon^{1/6} + 0.40244\varepsilon^{3/4} + \varepsilon \qquad \text{(A-4)}$$

Using the above results one arrives at the following useful expressions for $\nu(T)$:

$$\begin{aligned} \nu(T) &= 0 && \text{for } T < E_d \\ \nu(T) &= 1 && \text{for } E_d \leq T \leq 2E_d \qquad \text{(A-5)} \\ \nu(T) &= \beta\, \omega_D(\varepsilon)T/2E_d && \text{for } T > 2E_d \end{aligned}$$

where $\omega_D(\varepsilon)$ is the damage efficiency given by

$$\omega_D(\varepsilon) = \frac{1}{1 + kg\ (\varepsilon)} \qquad \text{(A-6)}$$

and $\beta = 0.8$. Equations A-5 are the most frequently used expressions for $\nu(T)$.

Before the above equations can be applied, a suitable value for the displacement energy, E_d, is needed. Doran et al.(159) suggested that the effective displacement energy in iron might be taken as 1.67 times the threshold value. For lack of a more definite model, E_d is generally taken to be:

$$E_d = 5/3\ E_d^{th} \qquad \text{(A-7)}$$

where E_d^{th} is the displacement threshold. For the case of vanadium E_d^{th} has been measured and is given as 26eV$^{(114)}$ (also see Chapter IV, section on Electron Irradiated Vanadium). This value for E_d^{th} results in $E_d = 43$ eV in vanadium; this is the value of E_d used throughout this dissertation.

REFERENCES

1. C. Cawthorne and E.J. Fulton, 1966 Harwell Symposium on The Nature of Small Defect Clusters, ed. J.M. Makin (1969), p. 446.

2. C. Cawthorne and E.J. Fulton, Nature, 216, 575 (1967).

3. G.W. Greenwood, A.J.E. Foreman, and D.E.Rimmer, J. Nucl. Mater., 1, 305 (1959).

4. J.L. Brimhall and B. Mastel, J. Nucl. Mater., 28, 115 (1968).

5. Proceedings of BNES European Conf. on Voids Formed By Irradiation of Reactor Materials, ed. S.F. Pugh, N.H. Loretto, and D.I.R. Norris, Reading, U.K., March 1971 (1971).

6. Proceedings of the Int. Conf. on Radiation-Induced Voids in Metals, ed. J.W. Corbett and L.C. Ianniello, Albany, N.Y., June 1971, AEC Symposium Series, CONF-710601 (1972).

7. Consultant Symposium on The Physics of Irradiation Produced Voids, ed. R.S. Nelson, Harwell, U.K., September 1974, AERE-R7934 (1975).

8. Radiation Damage In Reactor Materials, II, IAEA Symposium Proceedings, Vienna, June 1969, STI-PUB-230 (1969).

9. Proceedings of ASTM Conf. on Irradiation Effects on Structural Alloys for Nuclear Reactor Applications, Niagara Falls, N.Y., June 1970, ASTM-STP-484 (1971).

10. Proceedings of ASTM Conf. on Effects of Radiation On Substructural and Mechanical Properties of Metals and Alloys, Los Angeles, Calif., June 1972, ASTM-STP-529 (1973).

11. Proceedings of 1973 Int. Conf. on Defects and Defect Clusters In B.C.C. Metals and Their Alloys, Nuclear Metallurgy, Vol. 18, ed. R.R. Arsenault, Gaithersburg, Maryland (1973).

12. Proceedings of the Int. Conf. on Radiation Effects and Tritium Technology for Fusion Reactors, ed. J.S. Watson and F.W. Wiffen, Gatlinburg, TN, October 1975, CONF-750989 (1976).

13. R.S. Nelson and D.J. Mazey, Radiation Damage in Reactor Materials, Vol. II, STI-PUB-230 (1969), p. 157.

14. R.S. Nelson, Proc. of the Int. Conf. on The Use of Cyclotrons In Chemistry, Metallurgy, and Biology (Iliffe Press, Oxford, (1969), p. 273.

15. R.S. Nelson, D.J. Mazey, and J.A. Hudson, J. Nucl. Mater., 37, 1 (1970).

16. R.S. Nelson, D.J. Mazey, and J.A. Hudson, Voids Formed By Irradiation of Reactor Materials, ed. S.F. Pugh, N.H. Loretto, and D.I.R. Norris (1971), p. 191.

17. R.S. Nelson, J.A. Hudson, D.J. Mazey, G.P. Walters, and T.M. Williams, Radiation-Induced Voids In Metals, ed. J.W. Corbett and L.C. Ianniello, CONF-710601 (1972), p. 430.

18. D.W. Keefer, H.H. Neely, J.C. Robinson, A.G. Park, and D. Kramer, Irradiation Effects On Structural Alloys for Nuclear Reactor Applications, ASTM-STP-484 (1971), p. 332.

19. G.L. Kulcinski, J.J. Laidler, and D.G. Doran, Radiation Effects, 7, 195 (1971).

20. A. Taylor and S.G. McDonald, Radiation-Induced Voids In Metals, CONF-710601 (1972), p. 499.

21. K.D. Challenger, "Irradiation-Induced Void Swelling In Cold Worked Type-316 Stainless Steel Resulting From 5 MeV Nickel Ion Bombardment," Ph.D. Thesis, University of Cincinnati (1973).

22. G.L. Kulcinski, J.L. Brimhall, and H.E. Kissinger, Radiation-Induced Voids In Metals, CONF-710601 (1972), p. 449.

23. G.L. Kulcinski and J.L. Brimhall, Effects of Radiation On Substructural and Mechanical Properties of Metals and Alloys, ASTM-STP-529 (1973), p. 258.

24. D.J. Mazey, S. Francis, and J.A. Hudson, J. Nucl. Mater., 47, 137 (1973).

25. M.L. Sundquist, "Cavity Formation In Aluminum Irradiated With Aluminum Ions," Ph.D. Thesis, University of Wisconsin (1974).

26. A.T. Santhanam, A. Taylor, B.J. Kestel, and C. Steves, J. Vac. Sci. Technol., 12, 538 (1975).

27. S.C. Agarwal and A. Taylor, Radiation Effects and Tritium Technology for Fusion Reactors, Vol. I, CONF-750989 (1976), p. 150.

28. F.A. Smidt, Jr., "Controlled Thermonuclear Reactor Materials Program Annual Progress Report, 1 January 1975 to 31 December 1975," Naval Research Laboratory, Washington, D.C.

29. M.W. Thompson, Defects and Radiation Damage In Metals (Cambridge, 1969).

30. B.T. Kelly, Irradiation Damage To Solids (Oxford, 1966).

31. T.A. Gabriel, J.D. Amburgey, and N.M. Greene, "Radiation Damage Calculations: Primary Recoil Spectra, Displacement Rates, and Gas Production Rates:, ORNL-TM-5160 (1976).

32. N. Bohr, Mater. Fys. Medd. Dan. Vid. Selsk., 18: No. 8 (1948).

33. J. Lindhard, M. Scharff, and H.E. Schiott, Mat. Fys. Medd. Dan. Vid. Selsk., 39: No. 14 (1963).

34. K.B. Winterbon, P. Sigmund, and J.B. Sanders, Mat. Fys. Medd. Dan. Vid. Selsk., 37: No. 14 (1970).

35. J. Lindhard and M. Scharff, Phys. Rev., 124, 128 (1961).

36. K.B. Winterbon, Radiation Effects, 15, 73 (1972).

37. I. Manning and G.P. Mueller, Computer Physics Communication, 6, 1 (1973).

38. I. Manning and G.P. Mueller, Computer Physics Communication, 7, 85 (1974).

39. G.H. Kinchin and R.S. Pease, Reports on Progress in Physics, 18, 1 (1955).

40. W.A. McKinley and H. Feshbach, Phys. Rev., 74, 1759 (1948).

41. N.F. Mott, Proc. Roy. Soc., A124, 426 (1929).

42. N.F. Mott, Proc. Roy. Soc., A135, 429 (1932).

43. O.S. Oen, "Cross Sections For Atomic Displacements In Solids By Fast Electrons," ORNL-4897 (1973).

44. R. Bullough, B.L. Eyre, and R.C. Perrin, Nucl. Appl. Tech., 9, 346 (1970).

45. F.S. Ham, J. Appl. Phys., 30, 915 (1959).

46. S.D. Harkness and C.Y. Li, Met. Trans., 2, 1457 (1971).

47. R. Bullough and R.C. Perrin, Radiation Damage In Reactor Materials, Vol. II, STI-PUB-230 (1969), p. 233.

48. D.R. Olander, Fundamental Aspects of Nuclear Reactor Fuel Elements, NTIS, TID-26711-P1 (1976).

49. K.C. Russell and R.W. Powell, Acta Met., 21, 187 (1973).

50. M.R. Hayns, J. Nucl. Mater., 56, 267 (1975).

51. B.L. Eyre, Fundamental Aspects of Radiation Damage in Metals, Vol. I, ed. M.T. Robinson and F.W. Young, Jr., CONF-751006-P1 (1975), p. 729.

52. V. Levy, The Physics of Irradiation Produced Voids, AERE-R7934 (1975), p. 50.

53. D.I.R. Norris, The Physics of Irradiation Produced Voids, AERE-R7934 (1975), p. 134.

54. K. Urban, Voids Formed By Irradiation of Reactor Materials (1971), p. 275.

55. G.L. Kulcinski, J.L. Brimhall, and H.E. Kissinger, J. Nucl. Mater., 40, 166 (1971).

56. F.A. Smidt, Jr. and J.A. Sprague, Scripta Met., 7, 495 (1973).

57. J.L. Katz and H. Wiedersich, J. Chem. Phys., 55, 1414 (1971).

58. J.L. Katz and H. Wiedersich, Radiation-Induced Voids In Metals, CONF-710601 (1972), p. 825.

59. K.C. Russell, Acta Met., 19, 753 (1971).

60. K.C. Russell, Scripta Met., 6, 209 (1972).

61. K.C. Russell, Scripta Met., 7, 755 (1973).

62. K.C. Russell and D.H. Hall, Defects and Defect Clusters In B.C.C. Metals and Their Alloys (1973), p. 545.

63. K.C. Russell, The Physics of Irradiation Produced Voids, AERE-R7934 (1975), p. 158.

64. K.C. Russell, Acta Met., 20, 899 (1972).

65. J.L. Katz and H. Wiedersich, J. Nucl. Mater., 46, 41 (1973).

66. H. Wiedersich and J.L. Katz, Defects and Defect Clusters In B.C.C. Metals and Their Alloys (1973), p. 530.

67. H. Wiedersich, J.J. Burton, and J.L. Katz, J. Nucl. Mater., 51, 287 (1974).

68. H. Wiedersich, The Physics of Irradiation Produced Voids, AERE-R7934 (1975), p. 147.

69. B.T.M. Loh, Acta Met., 20, 1305 (1972).

70. J.A. Sprague, K.C. Russell, and U.H. Choi, Fundamental Aspects of Radiation Damage in Metals, Vol. I, ed. M.T. Robinson and F.W. Young, Jr., CONF-751006-P1 (1975), p. 1181.

71. K.C. Russell, Private Communication (To Be Published).

72. R.W. Powell and K.C. Russell, Radiation Effects, 12, 127 (1972).

73. W.G. Wolfer and M.H. Yoo, Radiation Effects and Tritium Technology for Fusion Reactors, Vol. II, CONF-750989 (1976), p. 458.

74. R. Bullough and R.C. Perrin, Voids Formed By Irradiation of Reactor Materials (1971), p. 79.

75. R. Bullough and R.C. Perrin, Radiation-Induced Voids In Metals, CONF-710601 (1972), p. 769.

76. R. Bullough and R.C. Perrin, Irradiation Effects On Structural Alloys for Nuclear Reactor Applications, ASTM-STP-484 (1971), p. 317.

77. H. Wiedersich, Second Int. Conf. on The Strength of Metals and Alloys, ASM (1970), p. 784.

78. H. Wiedersich, Radiation Effects, 12, 111 (1972).

79. C.Y. Li, D.G. Franklin, and S.D. Harkness, Irradiation Effects On Structural Alloys for Nuclear Reactor Applications, ASTM-STP-484 (1971), p. 347.

80. S.D. Harkness and C.Y. Li, Radiation-Induced Voids In Metals, CONF-710601 (1972), p. 798.

81. A.D. Brailsford and R. Bullough, J. Nucl. Mater., 44, 121 (1972).

82. A.D. Brailsford and R. Bullough, Defects and Defect Clusters In B.C.C. Metals and Their Alloys (1973), p. 493.

83. A.D. Brailsford and R. Bullough, Physical Metallurgy of Reactor Fuel Elements, ed. J.E. Harris and E.C. Sykes (1973), p. 148.

84. N. Ghoniem and G.L. Kulcinski, Univ. of Wisconsin Fusion Design Memo, UWFDM-180 (1976).

85. N. Ghoniem and G.L. Kulcinski, Univ. of Wisconsin Fusion Design Memo, UWFDM-181 (1976).

86. F.W. Wiffen and J.O. Stiegler, J. Metals, 20, 117A (1968).

87. F.W. Wiffen and J.O. Stiegler, Trans Am. Nucl. Soc., 12, 119 (1969).

88. J.D. Elen, Septieme Congres International de Microscopie Electronique, Vol. II (Paris, 1970), p. 351.

89. J.D. Elen, Voids Formed By Irradiation of Reactor Materials (1971), p. 51.

90. J.D. Elen, G. Hamburg, and A. Mastenbroek, J. Nucl. Mater., 39, 194 (1971).

91. Y. Adda, Radiation-Induced Voids In Metals, CONF-710601 (1972), p. 31.

92. F.W. Wiffen, Radiation-Induced Voids In Metals, CONF-710601 (1972), p. 386.

93. J.L. Brimhall, H.E. Kissinger, and G.L. Kulcinski, Radiation-Induced Voids In Metals, CONF-710601 (1972), p. 338.

94. R. Carlander, S.D. Harkness, and A.T. Santhanam, Effects of Radiation on Substructural and Mechanical Properties of Metals and Alloys, ASTM-STP-529 (1973), p. 399.

95. A.F. Bartlett, J.H. Evans, B.L. Eyre, E.H. Terry, and T.M. Williams, Radiation Effects and Tritium Technology for Fusion Reactors, Vol. I, CONF-750989 (1976), p. 122.

96. M. Cambini, J. Bressers, and M. Heerschap, J. Nucl. Mater., 62, 311 (1976).

97. J.H. Perepezko, R.F. Murphy, and A.A. Johnson, Phil. Mag., 19, 1 (1969).

98. B.M. Pande, M.S. Anand, and R.P. Agarwala, Radiation Effects, 24, 173 (1975).

99. J.T. Stanley, J.M. Williams, W.E. Brundage, and M.S. Wechsler, Acta Met., 20, 191 (1972).

100. M.S. Wechsler, J.M. Williams, and J.T. Stanley, Scripta Met., 7, 7 (1973).

101. J.F. McIlwain, C.W. Chen, C. Bajaj, and M.S. Wechsler, Effects of Radiation On Substructural and Mechanical Properties of Metals and Alloys, ASTM-STP-529 (1973), p. 529.

102. R.C. Rau and R.L. Ladd, J. Nucl. Mater., 30, 297 (1969).

103. K. Shiraishi, Y. Katano, and K. Fukaya, Cryst. Lattice Defects, 6, 51 (1975).

104. G.L. Kulcinski and J.L. Brimhall, BNWL-1604 (1971), p. 80.

105. A.T. Santhanam, A. Taylor, and S.D. Harkness, Defects and Defect Clusters In B.C.C. Metals and Their Alloys (1973), p. 302.

106. P.R. Okamoto, A.T. Santhanam, H. Wiedersich, and A. Taylor, Nucl. Technol., 22, 45 (1974).

107. J.L. Brimhall, "Effect of Helium on Void Nucleation in Vanadium", AIME Fall Meeting, Detroit, Michigan (October 1974).

108. J.L. Brimhall and E.P. Simonen, Nucl. Technol., 29, 378 (1976).

109. S.C. Agarwal, D.I. Potter, and A. Taylor, Irradiation Effects on the Microstructure and Properties of Metals, ASTM-STP-611 (1976), p. 298.

also

S.C. Agarwal, D.I. Potter, and A. Taylor, ANS Transactions, 26, 184 (1977).

110. S.C. Agarwal, Private Communication.

111. M. Heerschap and E. Schuller, J. Nucl. Mater., 38, 221 (1971).

112. K. Ehrlich and D. Kaletta, Radiation Effects and Tritium Technology for Fusion Reactors, Vol. II, CONF-750989 (1976), p. 289.

113. M. Kaminsky, S.K. Das, and G. Fenske, J. Nucl. Mater., 59, 86 (1976).

114. M.G. Miller and R.L. Chaplin, Radiation Effects, 22, 107 (1974).

115. P. Jung and G. Lucki, Radiation Effects, 26, 99 (1975).

116. R.L. Chaplin, K. Sonnenberg, and R.R. Coltman, Jr., Radiation Effects, 27, 119 (1975).

117. T.E. Mitchell, G. Das, and E.A. Kenik, Fundamental Aspects of Radiation Damage in Metals, Vol. I, ed. M.T. Robinson F.W. Young, Jr., CONF-751006-P1 (1975), p. 73.

118. R.I. Saunderson and W.J. Weber, Unpublished Results.

119. R. Bullough and R.S. Nelson, "Voids In Irradiated Metals," AERE-R7353 (1973).

120. R.G. Lott and H.V. Smith, Jr., Proc. of Symp. on Experimental Methods for Charged Particle Irradiations, Gatlinburg, TN, CONF-750947 (1975), p. 82.

121. H.V. Smith, Jr. and R.G. Lott, Nucl. Instr. and Meth., 143, 125, (1977).

122. H.V. Smith, Jr. and H.T. Richards, Nucl. Instr. and Meth., 125, 497 (1975).

123. R.A. Douglas, J. Zabritski, and R.G. Herb, Rev. Sci. Instru., 36, 1 (1965).

124. W.J. Weber, G.L. Kulcinski, R.G. Lott, P. Wilkes, and H.V. Smith, Jr., Radiation Effects and Tritium Technology, Vol. I, CONF-750989 (1976), p. 130.

125. J. Davis, McDonnell-Douglas Corp., Private Communication.

126. M. Stauber, Grumman Aerospace Corp., Private Communication.

127. Annual Book of ASTM Standard, Part 11, E 112-17 (1975), p. 205.

128. J.E. Westmoreland, J.A. Sprague, F.A. Smidt, Jr., and P.R. Malmberg, Radiation Effects, 26, 1 (1975).

129. T.D. Ryan, "Heavy-Ion Induced Void Formation In Nickel." Ph.D. Dissertation, University of Michigan (1975).

130. M.H. Loretto and R.E. Smallman, Defect Analysis in Electron Microscopy (New York: Halsted Press, 1975).

131. B.L. Eyre, D.M. Maher, and R.C. Perrin, Harwell Report AERE R-8223, to be published in Phil. Mag.

132. B.L. Eyre, D.M. Maher, and R.C. Perrin, Harwell Report AERE R-8224, to be published in Phil. Mag.

133. R.C. Perrin and B.L. Eyre, J. Microscopy, 98, 200 (1973).

134. P.B. Hirsch, A. Howie, and M.J. Whelan, Phil. Trans. R. Soc. A., 252, 499 (1960).

135. A. Howie and M.J. Whelan, Proc. R. Soc. A, 263, 217 (1961).

136. A. Howie and M.J. Whelan, Proc. R. Soc. A, 267, 206 (1962).

137. G.W. Groves and A. Kelly, Phil. Mag., 6, 1527 (1961).

138. G.W. Groves and A. Kelly, Phil. Mag., 7, 892 (1962).

139. D.J. Mazey, R.S. Barnes, and A. Howie, Phil. Mag., 7, 1861 (1962).

140. B. Edmondson and G.K. Williamson, Phil. Mag., 9, 277 (1964).

141. D.M. Maher and B.L. Eyre, Phil. Mag., 23, 409 (1971).

142. B.A. Bilby, R. Bullough, and E. Smith, Proc. R. Soc. A, 231, 263 (1955).

143. D.M. Maher and B.L. Eyre, Phil. Mag., 26, 1233 (1972).

144. R.G. Lott, Unpublished data.

145. The Encyclopedia of the Chemical Elements, ed. C.A. Hampel (New York, 1968), p. 439.

146. E.R. Stevens and O.N. Carlson, Metallurgical Transactions, 1, 1267 (1970).

147. W. Rostoker, The Metallurgy of Vanadium (New York, 1958) p. 59.

148. J.O. Stiegler, K. Farrell, C.K.H. DuBose, and R.T. King, Radiation Damage In Reactor Materials, Vol. II, STI-PUB-230 (1969), p. 215.

149. J.O. Stiegler, Radiation-Induced Voids In Metals, CONF-710601 (1972), p. 292.

150. J.T. Buswell, S.B. Fisher, J.E. Harbottle, and D.I.R. Norris, Physical Metallurgy of Reactor Fuel Elements, ed. J.E. Harris and E.C. Sykes (1973), p. 170.

151. G.H. Kinchin and R.S. Pease, Reports on Progress in Physics, 18, 1 (1955).

152. F. Seitz and J. Harrison, Phys. Rev., 98, 1530 (1955).

153. W.S. Snyder and J. Neufeld, Phys. Rev., 97, 1636 (1955).

154. J. Neufeld and W.S. Snyder, Phys. Rev., 99, 1326 (1955).

155. D.G. Doran Et al., "Report of Working Group on Displacement Models and Procedures for Damage Calcuations," February 1973.

156. I.M. Torrens and M.T. Robinson, Interatomic Potentials and Simulation of Lattice Defects, ed. P.C. Gehlen, J.R. Beeler, Jr., and R.I. Jaffe (Plenum Press, 1972), p. 423.

157. J. Lindhard, V. Nielsen, M. Scharff, and P.V. Thomsen, <u>Mat. Fys. Medd. Dan. Vid. Selsk.</u>, <u>33</u>: No. 10 (1963).

158. M.T. Robinson, Proceedings of Conf. on <u>Nuclear Fusion Reactors</u>, British Nuclear Energy Society (1970), p. 364.

159. D.G. Doran, J.R. Beeler, N.D. Dudey, and M.J. Fluss, HEDL-TME-73-76, December 1973.